Boron Nitride Nanostructures on Transition Metals: Flat Layers and Nanomesh

---

Dissertation

zur

Erlangung der naturwissenschaftlichen Doktorwürde
(Dr. sc. nat.)

vorgelegt der

Mathematisch-naturwissenschaftlichen Fakultät

der

Universität Zürich

von

Martina Corso
aus Italien

Promotionskomitee

Prof. Dr. Jürg Osterwalder
Prof. Dr. Thomas Greber
Prof. Dr. Herbert Over

Zürich 2006

Die vorliegende Arbeit wurde von der Mathematisch-naturwissenschaftlichen Fakultät der Universität Zürich auf Antrag von Prof. Dr. Jürg Osterwalder und Prof. Dr. Hugo Keller als Dissertation angenommen.

‘If we knew what we were doing,
it wouldn’t be called research,
would it?’

A. Einstein

Abstract

This thesis deals with the characterization of the structural and electronic properties of different hexagonal boron nitride (*h*-BN) nanostructures grown on the hexagonal ((111)) and rectangular ((110)) surfaces of some transition metals (Ni, Rh, Ru, Pd and Ir). They consist of single *h*-BN layers which are grown in ultra-high-vacuum by vapor chemical deposition of borazine ($(HBNH)_3$) on the metal surfaces kept at 800 °C. The lattice mismatch between the *h*-BN and the substrate and the strength of the bonding between the BN and the metal are among the main responsible for the morphology of the resulting *h*-BN layers. A large part of this work is focussed on the most peculiar of these structures: the 'nanomesh'. This nanostructure is a hexagonal network with a periodicity of 3.2 nm and 2 nm pore size. It grows by self-assembly of *h*-BN units on the Rh(111) and Ru(0001) surfaces. The combined information obtained from complementary surface sensitive techniques and theoretical calculations gave a deep insight on this complex system. Low energy electron diffraction (LEED) and surface x-ray diffraction (SXRD) confirmed that the nanomesh periodicity is due to (13 × 13) BN units growing on (12 × 12) Rh unit cells. Measurements with a low temperature scanning tunneling microscope (LT-STM) allowed to resolve the nanomesh with atomic resolution. X-ray photoelectron diffraction (XPD) patterns gave information on the geometric structure and the distribution of nanomesh domains on the surface. The valence band structure was obtained by angle resolved ultraviolet photoelectron spectroscopy (ARUPS). The nanomesh on Rh and Ru are discussed in view of their similarities and differences. The *fcc* and the *hcp* nature of the crystals is recognized by the nanomesh and the main difference between the two lies in their long- and short-range ordering. One chapter is dedicated to *h*-BN/Pd(111) and Pd(110), where the BN is only weakly physisorbed. Moiré patterns with several periodicities are found on the surface. A direct comparison between the *h*-BN layers on Ni(111), Rh(111), Pd(111) and Ru(0001) is given with respect to their valence band structure and the quantification of B and N coverages on the surfaces. This thesis demonstrates that these systems can be used as templates to assemble molecules, as shown by decoration experiments with C_{60}. Due to their stability in air and at high temperatures, these insulating ultra-thin *h*-BN layers are promising nanostructures for technological applications.

Zusammenfassung

In dieser Doktorarbeit wurden verschiedene Nanostrukturen aus hexagonalem Bornitrid (*h*-BN) untersucht. Diese bilden sich in einer Reaktion mit Borazin $(HBNH)_3$, auf Übergangsmetallen als atomar dünne Filme in drei verschiedenen Morphologien. Entweder wachsen die Filme pseudomorph, wie im Falle von Ni(111), in grossen Koinzidenzgittern (Rh(111), Ru(0001), Pd(111), Ni(110)), oder teilweise inkommensurabel (Pd(110)). Die Strukturen auf Rh und Ru waren unbekannt, sind aber besonders interessant und bilden ein sogenanntes 'Nanomesh'. Sie haben eine Gitterkonstante von etwa 3 Nanometern, wobei sich 2 Nanometer Poren ausbilden. Diese Poren sieht man in der elektronischen Struktur der Filme und sie bestimmen das Verhalten des *h*-BN Nanomesh massgeblich. Diese aussergewöhnlichen Strukturen können als Schablonen oder Lehren für die Anordnung von Molekülen oder kleinsten Metallaglomeraten (Cluster) benutzt werden, wie hier für den Fall von C_{60} gezeigt wird. Die *h*-BN Nanomesh Strukturen sind stabil an Luft und in Wasser und können im Vakuum bis 800° C geheizt werden. Diese Eigenschaften machen das *h*-BN Nanomesh zu einem vielversprechenden Kandidaten für Anwendungen in der Nanotechnologie.

List of Acronyms

2D/ 3D	two-/three-dimensional
AFM	atomic force microscopy/microscope
ARUPS	angle resolved ultraviolet photoelectron spectroscopy
CVD	chemical vapor deposition
DFT	density functional theory
DOS	density of states
ESCA	electron spectroscopy for chemical analysis
fcc	face centered cubic (lattice)
FFT	fast Fourier transform
FWHM	full width at half maximum
h−BN	hexagonal boron nitride
hcp	hexagonal close-packed (lattice)
$(HBNH)_3$	borazine
HOMO	highest occupied molecular orbital
IMFP	inelastic mean free path
I_t	tunneling current
LDOS	local density of states
LEED	low energy electron diffraction
LT	low temperature
LUMO	lowest unoccupied molecular orbital
ML	monolayer
MSC	multiple scattering cluster calculations
SBZ	surface Brillouin zone
SSC	single scattering cluster calculations
STM	scanning tunneling microscopy/microscope
STS	scanning tunneling spectroscopy
SXRD	surface x–ray diffraction
UHV	ultra–high vacuum
UPS	ultraviolet photoelectron spectroscopy
UV	ultraviolet (radiation)
V_s	sample bias voltage
XPD	x–ray photoelectron diffraction
XPS	x–ray photoelectron spectroscopy

Contents

1 Introduction

1.1 Nanomaterials, nanoscience and nanotechnology

There is no doubt that 'nano' is the prefix of the 21st century. Nanoscale materials, or nanomaterials, are objects with at least one dimension that is on the nanometer scale (between 1 nm and 100 nm). They have become one of the most popular research topics in a very short period of time. Due to their dimensions, nanomaterials possess unique physical and chemical properties when compared to their bulk counterparts even if they have the same atomic or molecular composition. Their peculiar properties are due to quantum size effects and due to their morphology and spatial arrangement. Since at this length scale more and more atoms are exposed to the surface, phenomena (such as wetting) that take place there play a crucial role. The great interest in their study is driving nanotechnology and nanoscience (in particular nano-physics, -chemistry and -biology). These are continuously fueled not only by the research for new efficient use of energy sources, effective treatment of hazards, accurate detection and treatment of human diseases, but especially by the emerging industrial needs of miniaturization of functional devices with higher storage capacity and speed. Today composite devices on silicon chips as small as 180 nm can be routinely fabricated with optical lithography: this is already a great improvement from the first integrated circuits of 15 µm. The celebrated Moore's law (1965) states that the number of silicon field-effect transistors per unit area in an integrated circuit chip is doubled every 18 months. Therefore it is anticipated that in the near future a nanodevice size of 50 nm needs to be reached in order to satisfy the demands of consumers, but tools and methodologies for a cheap mass production of such devices are not yet ready [1]. Two different approaches are used to manufacture nanodevices or to create surface patterns: the '*top down*' and the '*bottom up*'. The former can generate features down to the sub-100 nm range and is based on lithographic techniques and electron-beam writing. The key elements of nanolithography are the *writing* and the *replication*. First a 'master' (a structure that provides or encodes a pattern to be duplicated in multiple copies) has to be written and molded, then it has to be transferred to a functional material. Nanomanufacturing requires a combination of high-precision writing and a low-cost replication of masters. The first is usually done with a focused beam of electrons or ions scanned on a material while the second is nowadays achieved with optical photolithography [2]. The existing technologies are rapidly approaching their ultimate capacities and the conventional optical photolithography, the limits of which are due to optical diffraction, is likely to be replaced by advanced lithographic techniques that use extreme ultraviolet light or hard x-ray radiation (Fig. 1(a)) [3, 4]. The enormous costs that will be encountered in their development are pushing scien-

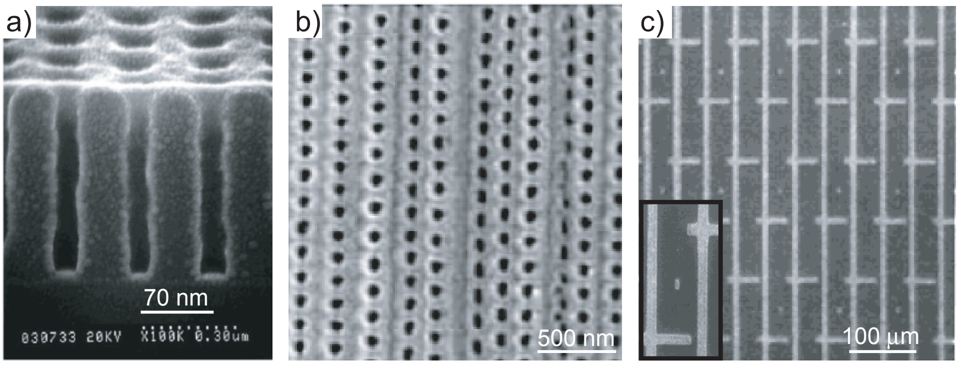

Figure 1: *Nanopatterns obtained with different 'top down' techniques. (a) Hole pattern of 70 nm size replicated in a UV2-HS chemically amplified resist with synchrotron radiation lithography [4]. (b) AFM image of a portion of a pattern of holes spaced by 70 nm created by thermal imprinting with a 'millipede' [5, 6]. (c) Scanning electron microscopy image of a surface with patterned carbon nanotubes [7]. Inset, lower scale image of the same structure.*

tists and engineers to move towards cheaper and simpler non-photolithographic methods for pattern transfer. For example attention is paid to soft-lithography which embraces techniques as replica molding (REM), embossing, and microcontact printing (μCP), for which a periodicity smaller than 100 nm can be obtained [2, 6]. The first transfers topological features from a rigid or elastomeric mold into another material by solidifying a liquid in contact with the original pattern. The second is the process of imprinting a pattern to a flat substrate coated with a deformable material by pressing a mold into its surface. The third brings a topographically patterned stamp, wetted with a solution of alkanethiol or other molecules that can self-assemble, into contact with a metal, metal oxide or semiconducting surface for a few seconds such that at the point of contact an ordered monolayer forms. Besides these methods, scanning probes as atomic force microscopes (AFMs), scanning tunneling microscopes (STMs) or scanning near-field optical microscopes (SNOMs) are unique techniques with a resolution that approaches the atomic level. They are capable to modify or generate ordered structures on surfaces, even by controlling and manipulating single atoms. For example, AFM tips can create a pattern on a surface by removing or depositing material. In dip-pen nanolithography, an AFM tip is 'inked' with a solution of material that is selectively transferred to the substrate when the probe scans across the surface; patterns can be as small as 15 nm. Effort is given in trying to increase the patterning speed of these devices by incorporating arrays of tips that can write in parallel, guided by the same electronics (Fig. 1(b)) [5]. It is likely that these last methods will be used for formation of masters rather than for replication and they will not find industrial use in the next future.

Since the seventies, research in nanoscience has moved also towards the field of molecular electronics and the implementation of nanotubes in nanodevices has spread extremely fast. These nanomaterials are carbon allotropes that can be either semiconductors either metallic conductors with peculiar electronic properties and extraordinary mechanical strength. In particular single-wall nanotubes can be considered as prototypes for a one-dimensional quantum wire. For example they have been recently used in the production of intramolecular field effect transistors (FETs) [8, 9] that can be potentially used as biological or chemical sensors [10]. Multiwalled nanotubes have been used to pattern surfaces with photolithography or μCP (Fig. 1(c)) [7]. Many other applications have been found for these materials or their derivates (from lithium batteries to tennis rackets). Nevertheless, they are still very expensive for mass production and cheaper means of synthesis need to be found.

Nanoscience and nanotechnology are moving towards *'bottom up'* techniques that seem to be very suitable and cheap tools for patterning at the nanoscale. While the *'top down'* approaches carve a surface in order to produce the desired pattern, in the case of *'bottom up'*, atoms, molecules or particles self-assemble spontaneously into organized surface structures. Examples of these structures obtained with different strategies include those derived from aggregated surfactant molecules, self-assembled monolayers, crystallized proteins or colloidal particles. In their current state of development, techniques that use self-assembly (such as buckling [11] or microphase separation of block copolymers [12]) are naturally integrated with other more common fabrication methods. Devices already commercially available make use of patterns with a periodicity of 20 nm obtained by self assembled phase-separated block copolymers [13]. Self-assembly is not much used yet in nano and micro-fabrication, although it offers opportunities to simplify processes, lower costs, develop new processes, use components too small to be manipulated robotically, integrate components that are created using incompatible technologies and generate structures in three dimensions and on curved surfaces. It allows to pattern unconventional materials into structures impossible to shape with any other standard method [2]. The major limitations of self-assembly do not seem to be intrinsic, but rather operational: fabricating the small, complex, functional components that future applications may require, will necessitate the development of new methodologies.

1.2 Self-assembly and self-organization

Self-assembly and *self-organization* are related notions but they are often used in inappropriate contexts. The concept of *self-assembly* started to be used in the sixties, and it takes its origin from biological processes such as the formation of the DNA double helix. It refers to the spontaneous aggregation of sub-units (molecules, or meso-scale objects) into stable, well-defined structures. Self-assembly implies spatial structuring as a result of minimization of the free energy in a closed system. Hence, a self-assembled structure corresponds to a thermodynamic equilibrium and for this reason it tends to reject defects [2]. The most important driving force for self-assembly in general is the interaction energy between the subunits involved. On the fundamental level the interaction between atoms, ions or molecules can be divided into three categories depending on their charge state: Coulomb interaction due to the electrostatic effects from the permanent charges, van der Waals interactions due to instantaneous polarization induced by the neighboring units and short range strong repulsion [1]. The total interaction energy between macroscopic bodies (such as spherical particles) is the summation of the electrostatic repulsion and the van der Waals attraction (that can be assumed to be the addition of all the contributions from the individual atoms or molecules). The prevailing of one component with respect to the other leads either to their separation or to their aggregation. For polar molecules and water, another important intermolecular force is the hydrogen bonding and the related hydrophobic or hydrophilic interactions. *Self-organization*, on the other hand, requires a situation far away from thermodynamic equilibrium and it is possible only in open systems with an external energy source. This term was initially used in the late 19^{th} century to describe the human collective behaviour and then it has been transposed to describe cooperative phenomena in natural sciences, mathematics, informatics (as neural networks), economics, sociology and many more. Heterogeneous catalytic reactions are an aspect of self-organization taking place on surfaces. They are systems far from thermodynamic equilibrium, and therefore one can observe in such systems rate oscillations, spatiotemporal patterns and chaos, a group of phenomena which has been denoted as dissipative structures [14]. However it has become common to use the term *self-organized growth* in metals or semiconductors epitaxy when strain-relaxation or kinetic limitations in the growth process give rise to the formation of complex structures as quantum dots or dislocation patterns.

1.3 Nanostructure formation at the fundamental level

Focusing on processes involved in the growth of nanostructures on surfaces, the primary parameter that needs to be taken into account is the diffusion of an adatom on a surface. Depending on the place where it lands, an adatom or molecule has to overcome barriers in order to hop from one adsorption site to another, on a terrace, over steps, along edges or around kinks. These thermally activated processes are represented by the diffusivity D, a parameter defined as the mean square distance travelled by an adsorbate per unit time. It depends exponentially on the potential energy barrier for hopping and on the substrate temperature, obeying an Arrhenius law. If the flux F of molecules or atoms impinging on a surface is kept constant, then D is the average distance they will travel before meeting another adatom and nucleate an island, or joining an existing one. As F increases, the nucleation and expansion of islands on the surface will increase as well, thus lowering the value of D. It is clear that the ratio of deposition rate and diffusivity is a key parameter in the growth kinetics. If the deposition rate is fast relative to the diffusion then individual processes and metastable structures become important. In this regime where the complex kinetics and hierarchy of the different diffusion steps is fundamental, metallic islands form. Semiconductors are grown at intermediate values of D/F and the morphology of the resulting structures is driven by the interplay between kinetics and thermodynamics. When the deposition is slower than diffusion, then the growth occurs at equilibrium conditions since the system has enough time to reach a minimum energy configuration. In this case supramolecular self-assembly is allowed since molecules are able to recognize each other [15]. When atoms join to form an island the cohesive energy between them prevents the island to collapse, that is the free energy of the island is negative. To this energy should be added the positive contribution given by the 'boundary free energy', a destabilizing factor due to the presence of dangling bonds at the island edges. At the beginning of island formation the boundary free energy dominates and the total free energy becomes more and more positive as atoms are added. Therefore to nucleate an island, enough atoms have to meet to make the total island's free energy negative [16]. In homoepitaxy as islands continue to grow they develop with specific shapes: either compact ones (as squares, triangles or hexagons), or fractal-like with highly anisotropic shapes [17]. The temperature, the bonding geometry and the symmetry of the substrate seem to play an important role in the resulting island morphology. In hetheroepitaxial growth three main processes have been observed experimentally, depending on the interfacial free energies of overlayer and substrate and on the lattice mismatch. The three modes have been classified as: layer-by-layer growth (Frank-van der Merwe), the island growth mode (Volmer-Weber) and the layer-then-island growth mode (Stranski-Krastanow) in lattice mismatched systems. Attention is paid to the last mode as a method to grow quantum dots. Besides this three-dimensional aggregation, also a lateral ordering can be induced by the elastic and electrostatic forces present in lattice mismatched materials. Long-range interactions are responsible for the formation of strain-relief or reconstruction patterns that minimize the stress to which the atoms in the epilayer and substrate are continuously subjected. Regarding molecular behavior, the formation of self-assembled low-dimensional supramolecular structures at surfaces is governed by the subtle balance between intermolecular and molecule-surface interactions, which can be tuned by the appropriate choice of the substrate material. The ultimate ordering is achieved by the balance of three fundamental parameters: the magnitude of the thermal energy involved in the process, the surface translational and rotational mobility of the species adsorbed and the strength and nature of the intermolecular interactions. Therefore the right combination of the symmetry of the substrate and the chemical nature of the components involved can be optimized in order to guide the supramolecular self-assembly towards a desired structure.

1.4 Examples of nanopatterned structures

This thesis is centered on the presentation of a peculiar self-assembled nanostructure: the *nanomesh* [18]. This honeycombed mesh results from the spontaneous arrangement of hexagonal boron nitride (*h*-BN) units on the Rh(111) surface. Its periodicity of 3 nm, its double layer character, its insulating nature, its spatial-order developed not only locally, its stability to high temperatures, in air and in aqueous environments [19] and its possibly easy mass production make the nanomesh a nanomaterial unique in its kind. To better appreciate this structure, a few examples of other patterned surfaces obtained with different approaches are here presented. A carbon hexagonal structure (Fig. 2(a)) can be formed by annealing to 1100 °C the 6H-SiC(0001) surface [23]. At these elevated temperatures Si atoms from the bulk evaporate and carbon nanoclusters segregate on the surface forming a honeycombed array with a periodicity of $(6\sqrt{3} \times 6\sqrt{3})$R30° in low-energy electron-diffraction (LEED) patterns. STM images of this surface show a (6×6) overstructure whose atomic unit cell is still on debate. It could either correspond to a Moiré pattern [24], or to a network with a pore size of 2 nm [23]. This nanotemplate has been used to grow monodispersed Co nanoclusters (Fig. 2(b)) [20]. Co species do not react with the underlying SiC to form cobalt silicide during cluster formation and annealing process. This observation suggests that the centers of the carbon mesh are also covered by carbon islands one monolayer (ML) thick, therefore this is a chemically inert surface. While in the growth of metal clusters on graphite or sapphire, their lateral distribution is very heterogeneous, in this case the Co cluster size distribution is narrow. This is probably due to the limited diffusion of atoms inside the mesh holes.

The same formation process has been seen in the growth of nanoislands on dislocation networks. In some homo- and hetero-epitaxial systems strain can be relieved through dislocations. These dislocations often arrange into ordered periodic patterns, due to their long-range repulsion and mobility. A peculiar case is given by 2 ML of Ag on the Pt(111) substrate. The first monolayer of Ag grows pseudomorphic and strained due to the large compressive lattice mismatch of +4.3% between Ag and Pt. The second monolayer of Ag forms a trigonal network of dislocations through which part of the stress is relieved (Fig. 2(c)). The dislocations are the boundaries between face-centred cubic (*fcc*) and hexagonal close-packed (*hcp*) adsorption sites. The unit cell has trigonal

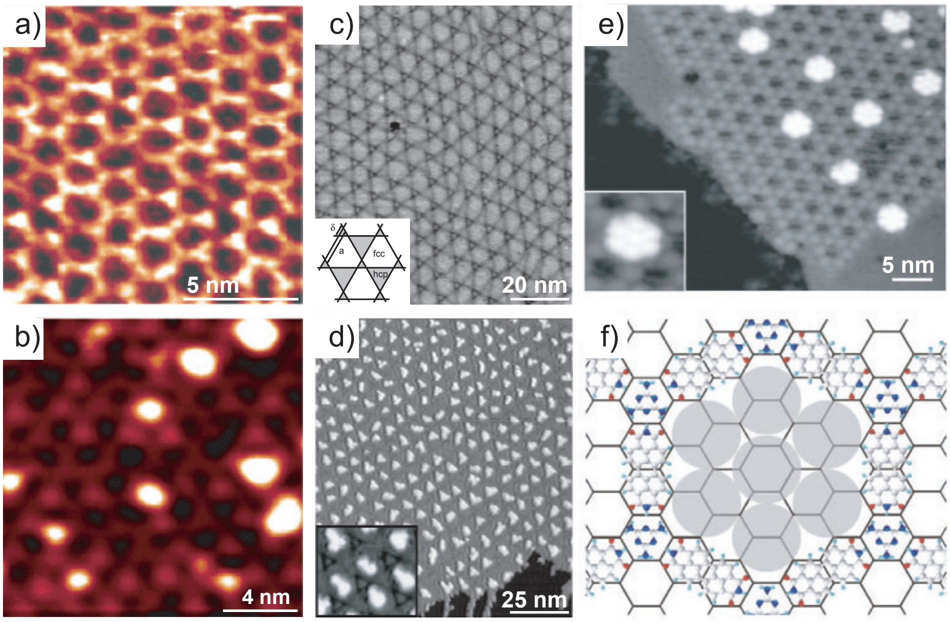

Figure 2: *Examples of nanometer-scale nanostructures as appearing in STM images. (a) Carbon porous hexagonal network obtained by annealing a SiC(0001) substrate [20]. (b) Co nanoclusters adsorbed on the carbon mesh. (c) Dislocation strain-relief pattern formed by the second ML of Ag on Pt(111). Inset, model of the structure. (d) Superlattice of islands formed by deposition of 0.1 ML of Ag on the network in (c) [21]. Inset, zoom on the picture (d). (e) Supramolecular honeycomb arrangement of PTCDI and melamine self-assembled on a Ag terminated Si(111) surface [22]. The white islands are C_{60} clusters in the network pores. Inset, zoom on a C_{60} cluster. (e) Schematic reproduction of a C_{60} heptamer and the molecular structure.*

symmetry and consists of a large quasi-hexagon (*fcc*) and two oppositely oriented triangles (*hcp*). The periodicity is 7 nm, that corresponds to (25×25) Pt lattice constants. This structure can be used to assemble periodic nanoclusters. For example, when it is further exposed to Ag at low temperatures (110 K), a superlattice of monodispersed Ag islands self-organizes (Fig. 2(d)). The surface dislocations are very repulsive to diffusing adatoms thus the islands nucleate only into the *fcc* hexagons [21]. This kind of self-organized growth in homo- and hetero-epitaxial systems and semiconductors aimed to obtain patterned networks, makes use of periodic variations in adatoms binding energy. Repulsive dislocations or Moiré patterns are phenomena appropriate for this purpose.

Two-dimensional open honeycomb networks can be obtained also via assisted supramolecular assembly. In particular, hydrogen bonding has been used to guide the coadsorption of two different molecules, perylene tetra-carboxylic di-imide (PTCDI) and melamine (1,3,5-triazine-2,4,6-triamine), on the reconstructed $(\sqrt{3}\times\sqrt{3})$R30° Ag/Si(111) surface [22]. First 0.1-0.3 ML of PTCDI are deposited at room temperature and then melamine while keeping the substrate at 100 °C. Each melamine molecule sits at the corners of the network and forms hydrogen bonds with three PTCDI molecules that compose the straight edges. This overstructure has a lattice constant of 3.5 nm and is rotated 30° with respect to the substrate. The exposure to C_{60} molecules for a coverage on 0.1-0.3 ML results in the formation of clusters of 2 to 5 molecules trapped inside the mesh pores (Fig. 2(e)). At higher coverages the C_{60} molecules cover also the underlying mesh wires and a compact fullerenes network rises. Further deposition of C_{60} does not lead to the formation of additional layers on the hexagonal network.

The examples illustrated here, and many more, represent the first stage characterization of self-assembled nanopatterned structures with periodicities below 10 nm. They are produced and analyzed in ultra-high vacuum, under extreme conditions far from the macroscopic world. Thus their incorporation in more complex nanodevices or systems is a challenging goal for the research community. The *h*-BN-nanomesh, on the other hand, represents a model candidate for technological applications in the near future.

2 Experimental techniques and setup

Different techniques have been used in this work in order to study different properties of the nanostructures under investigation. In particular, information about the long range ordering were given by the analysis of low-energy electron diffraction (LEED) images, the ordering at the atomic level by x-ray photoelectron diffraction (XPD) patterns, the elemental composition on the surface by x-ray photoelectron spectroscopy (XPS) and the electronic structure by angle-resolved ultraviolet photoelectron spectroscopy (ARUPS). While all these techniques average over a macroscopic area of the sample surface, the local information has been obtained with scanning tunneling microscopy (STM).

2.1 Scanning tunneling microscopy (STM)

The scanning tunneling microscope (STM) is 'a kind of nanofinger for sensing, addressing, and handling individually selected atoms, molecules, and other tiny objects and for modifying condensed matter on an atomic scale' [25]. The original goal of its inventors, G. Binnig and H. Rohrer in 1982 [26], was to study the structural, electronic and growth properties of thin insulating films locally, ie. at a scale in which also the inhomogeneities were accessible. Due to its ultimate resolution at the atomic level, this remarkable instrument became the basis of an enormous development not only within physics, but also in chemistry and biology. It is widely used nowadays either as a standard analysis tool for surface characterization or as a high level research instrument. Its continuous development from the original setup made it possible to extend the range of phenomena studied. The measuring temperature, time and pressure for example are operational parameters that can be routinely controlled. Therefore STMs are not only used to characterize the surface topography but also to measure its electronic and magnetic properties, to manipulate atoms or molecules, to study in real time surface phenomena such as phase transitions or surface reconstructions, or to follow chemical reactions. Nevertheless it has always been clear that scanning tunneling microscopy is characterized by a dual aspect: one thing is to obtain a STM image, and quite another is to understand the structure seen in it.

2.1.1 Taking STM images

The *tunneling effect* is the base principle of a STM. In this quantum mechanical phenomenon, electrons have a non-vanishing probability to overcome a classically forbidden potential barrier, therefore they are able to pass through vacuum or an insulating thin layer between two electrodes placed at a close distance and to 'jump' from one lead to the other. In a STM, a sharp metallic tip is brought into close proximity of a metallic surface.

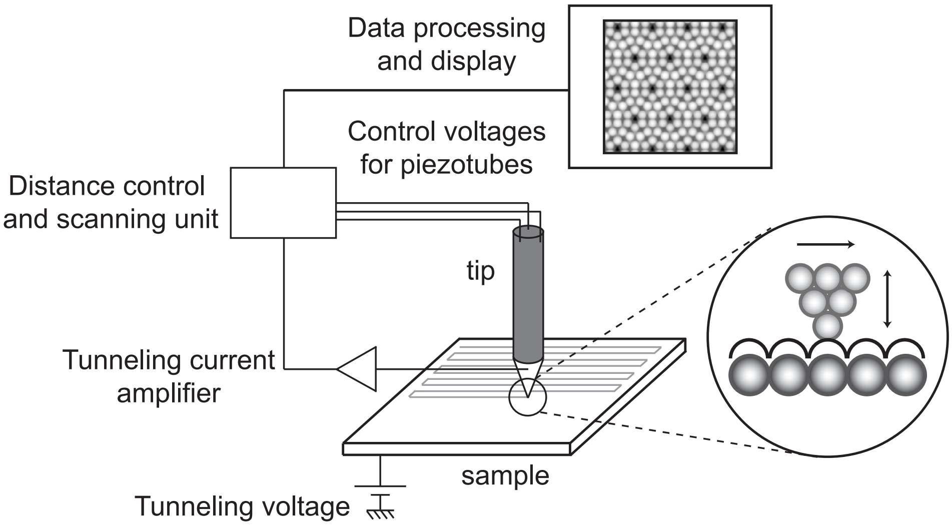

Figure 3: *Schematic illustration of the basic principles and operation of the STM. The tip is moved in 3D by means of piezo-electric elements, a tube geometry is shown. During the scanning from left to right the tunneling current flowing between the tip and the sample is recorded. A feed-back circuit is introduced in order to regulate the tip height. All the tip trajectories on the scanned surface are displayed as an image on a computer screen. On the right the tip apex and the sample surface are shown at the atomic level with a magnification of* 10^8.

Applying a voltage (V) between the two, typically ranging from a few millivolts to a few volts, electrons tunnel from the sample to the tip surface or vice versa, depending on the polarity. The exponential decay of the tip and sample wave functions into the vacuum gap requires a distance between them of only 0.5 to 1 nm (2 to 4 atomic distances) in order to achieve a sufficient overlap for measuring a tunneling current (I_t) in the range of a few picoamperes to a few nanoamperes. In order to control so precisely its position, the tip is attached to a piezo-electric element (usually with a tube geometry). By adjusting the voltages on this element one is able to regulate the distance between the tip and the sample and to raster-scan it in the directions parallel to the sample surface. A scheme of the working principle of a STM is shown in Fig. 3. Operating in the *constant current* mode, one wants to maintain I_t constant. Therefore during the scanning on the sample surface, every time the last atom of a tip is above a surface atom, the tunneling current increases, and the tip needs to be retracted, while it has to be brought closer if it is between surface atoms. This distance regulation is performed automatically by a feedback electronic system that corrects the position of the tip whenever the measured current deviates from the desired I_t value. A STM image consists in a full record of the trajectory of the tip scanned over the surface. The set of all these trajectories plotted together represents the atomic corrugation of the surface. Another possible way to operate the STM is in the *constant height* mode, where the vertical position of the tip is kept constant and the variation of tunneling current is recorded during the scanning over the surface. The whole STM operation is usually computer-controlled and the scanning parameters as V, I_t and the raster speed are set via an interface.

2.1.2 Interpreting STM images

There exists no inversion theorem which allows from a given STM image to deduce the electronic and geometrical structure of the surface. A full interpretation of the information from the STM measurements requires the ability to generate reliable models for the surface and for the tip, solving their electronic structures, modeling the interactions between them and calculating the tunneling currents. Then theoretical STM images can be produced from fully ab initio methods and they can be compared to the experimental ones [27,28]. A theoretical description of the tunneling process in STM has been treated with different approaches and at different levels of approximation, in particular within *perturbation theory* and *scattering theory.*

To introduce the concept of STM imaging one can consider the simple case of the tunneling process in one dimension [29]. The solution of the Schrödinger equation for an electron moving in a rectangular barrier U extended in a region $0 < z < d$ is:

$$\Psi(z) = \Psi(0)e^{-kz} \tag{1}$$

where $k = \sqrt{2m(U-E)}/\hbar$, E is the energy of the electron, m is its mass and $\hbar$ is the Planck constant. The probability (Γ) of observing the electron at the end of the potential barrier is $\Gamma \propto |\Psi(d)|^2 = |\Psi(0)|^2 e^{-2kd}$. It is straightforward to generalize to the case of a metal-vacuum-metal junction where the metals are identical, the sample states are Ψ_n, the work function is Φ and the thermal excitations of electrons are neglected (Fig. 4). Assuming that $eV << \Phi$ is valid for negative bias (V) applied to the sample, then the probability of an electron, in the n^{th} state with energy E_n between the Fermi level E_f and $E_f - eV$, to tunnel to the tip surface ($z = d$) is $\Gamma \propto |\Psi_n(d)|^2 = |\Psi_n(0)|^2 e^{-2\sqrt{2m\Phi}d/\hbar}$. The tunneling current is then proportional to the total number of states on the sample surface with energies within the interval $\Delta E = [E_f - eV, E_f]$:

$$I_t \propto \sum_{E_n=E_f-eV}^{E_f} |\Psi_n(d)|^2. \tag{2}$$

If the density of electronic states (DOS) does not vary significantly within the energy interval ΔE, this result can be expressed through the *local density of states* (LDOS)

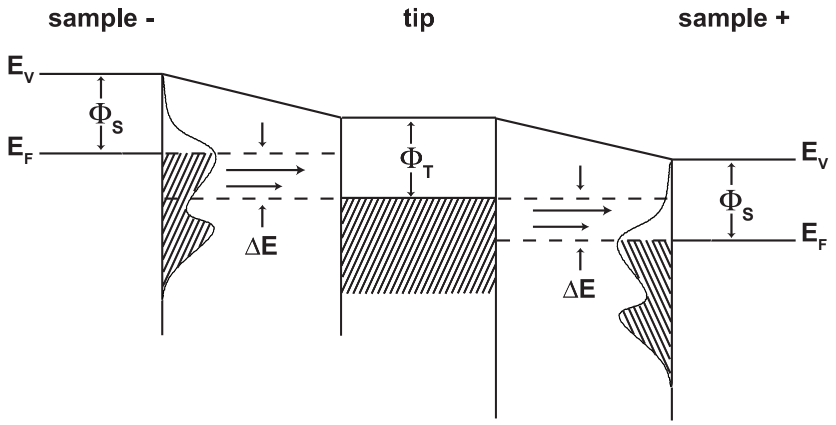

Figure 4: *When a negative voltage is applied to the sample, electrons tunnel from the occupied sample states to the tip, on the contrary if the sample is positively biased, electrons flow in the opposite direction and empty sample states are mapped.* Φ_s *and* Φ_t *are the sample and the tip work functions, respectively.*

$\rho_s(d, E_f)$ of the sample at the Fermi level and at the tip position $z = d$, thus Eq. 2 becomes:

$$I_t \propto V\rho_s(d, E_f) = V\rho_s(0, E_f)e^{-2\sqrt{2m\Phi}d/\hbar}. \tag{3}$$

In this view a constant-current STM image at a small bias voltage is a contour map of the sample surface LDOS at the Fermi energy and at the position of the tip over the surface. Eq. 3 explains why an increase in the tip-sample distance as small as 1 Å leads to a decrease of one order of magnitude in I_t (taking a value for Φ of $4 - 6\,\mathrm{eV}$). For a more precise treatment of the problem, one can use the formalism of **Bardeen** where tip and sample are treated as separated entities [30]. One first calculates the electronic wave functions for the isolated tip (Ψ_t) and the isolated sample (Ψ_s) solving the stationary Schrödinger equation; then the tunneling matrix element (M) is given by the overlap of these wave functions at a surface S running in the vacuum region between them:

$$M = \frac{\hbar^2}{2m}\int\limits_S (\Psi_s^* \nabla \Psi_t - \Psi_t^* \nabla \Psi_s) d\mathbf{S}. \tag{4}$$

This quantity is used in time-dependent perturbation theory to calculate the tunnel probability between two states Ψ_t and Ψ_s via the *Fermi's golden rule*:

$$\Gamma = \frac{2\pi}{\hbar}|M|^2\delta(E_{\Psi_s} - E_{\Psi_t}) \tag{5}$$

where the δ-function ensures the energy conservation and thus only elastic processes are taken into account. The tunneling current results from the sum over all the states with energies between the Fermi level and eV (where V is a negative voltage applied to the sample):

$$I_t = \frac{2\pi e}{\hbar} \int_{-\infty}^{\infty} [f(E - eV) - f(E)]\rho_s(E - eV)\rho_t(E)|M|^2 dE \tag{6}$$

where *f(E)* is the Fermi distribution function and ρ_s and ρ_t are the densities of states (DOS) of the sample and of the tip, respectively. In the approximation of the Fermi function to its zero temperature expression, Eq. 6 can be written as:

$$I_t = \frac{2\pi e}{\hbar} \int_{E_f}^{E_f + eV} \rho_s(E - eV)\rho_t(E)|M|^2 dE. \tag{7}$$

If M does not vary much in the energy interval ΔE, then the tunneling current is determined by the convolution of tip and sample surface DOS.

An easy way to evaluate the matrix element M was given by **Tersoff and Hamann** which assumed that the predominant tip state involved in the tunneling is an *s*-state [31]. They showed that for small bias voltages (V) the tunneling current is proportional to the LDOS of the sample at the Fermi level and at the centre of curvature of the tip (r_0):

$$I_t \propto V \frac{R^2}{k^4} e^{-2kR} \rho_t(E_f)\rho_s(E_f, r_0) \tag{8}$$

where R is the tip radius and $k = \sqrt{2m\Phi}/\hbar$ is the minimum inverse decay length for the wave functions in the vacuum gap with a local barrier height Φ. A STM image now can be seen not just as the topography of a surface, but as a convolution of topographic and electronic information. In the interpretation of the features seen by STM, one has to be aware that while topography is due to the total charge density, STM is more sensitive to the density of states at the Fermi level. While this aspect can be almost neglected in the case of metals, it can be predominant in semiconductors or surfaces covered by adsorbates.

The Tersoff-Hamann approximation is very convenient and gives a simple picture of the STM operation but in some situations one needs to include more details of the electronic structure of the tip (p- and d-states) [29, 32], while still remaining in the perturbation theory. However this theory can not be applied in two particular cases: the first is when the tunneling becomes intrinsically strong (as when a point contact between sample and tip forms) [33]; the second occurs when the tunneling is 'more rapid' than some other part of the electron transport process (as for example if there is a second barrier, such as a thin insulating layer on one surface, in the way of the passage of the electrons [34]). In either case, a single treatment of the transport of electrons through the whole system (tip and sample) is necessary and one can use the scattering theory. The basic idea is to treat the sample and the tip as two semi-infinite periodic systems separated by a two-dimensional defect represented by the tunneling gap. Bulk electrons then scatter from the tunneling junction and have a small probability to pass to the tip and a large probability to be backscattered. In the **Landauer-Bütticker** [27] approach the conductance across a tunneling junction is given by the ratio of the transmission probability (T) to the reflection probability, and the tunneling current is usually written as:

$$I_t = \frac{2e}{\hbar} \int_0^{eV} T(E) dE. \tag{9}$$

The advantages of this approach are its mathematical rigor, its inclusion of the different boundary conditions for tip and sample states and the possibility to take into account interference effects between separate conductance channels. On the other hand usually a model for the structures of the two leads is calculated with the tight-binding theory and these results often disagree with experiments. Today the most accurate method in the tunneling theory is the one of **Keldysh-Green** where a wide range of interactions can be included, as inelastic processes, spin-flips and multiple scattering events [35]. Nevertheless the computational time limits its complete use.

Since the tunneling current depends on the local density of states of the sample the dependence on the voltage in STM can be used to obtain spectroscopic information on the local electronic structure of a surface. While for very small voltages and for an s-type tip the tunneling current is directly proportional to ρ_s (Eq. 7), for modest voltages the results of Tersoff and Hamann [31] can be qualitatively generalized as:

$$I_t(V) \propto \int_0^{eV} \rho_s(E) \exp\left(\frac{-2z\sqrt{2m}}{\hbar} \sqrt{\frac{\Phi_s + \Phi_t}{2} + \frac{eV}{2} - E} \right) dE = \int_0^{eV} \rho_s(E) T(E, dV, d) dE \tag{10}$$

where the effect of the voltage on the surface wave functions is included through a barrier transmission coefficient $T(E, eV)$ [36]. With the assumption that ρ_t is a smooth function (usually valid for blunt tips at E_f) and for a monotonous transmission coefficient (not strongly dependent on the voltage), the differentiation of the convolution integral for the tunneling current, expressed in Eq. 10, with respect to the voltage allows to relate directly the differential conductance dI/dV to ρ_s as:

$$\frac{dI}{dV} \propto \rho_s(eV) T(eV) + A(V) \tag{11}$$

where the term $A(V)$ contains the voltage dependence of T. Experimentally, different kinds of scanning tunneling spectroscopy (STS) measurements can be perfomed. Local tunneling spectra (i) are obtained by positioning the tip over the surface at some tip-sample separation z as a function of start parameters $(z_0(I_0, V_0))$ and then sweeping the bias voltage V (with open feed-back loop) and recording the tunneling current $I(V)$. This allows to record spectra crossing 0 V. Besides point spectroscopy, (ii) one can keep the tunneling current constant and modulate the bias voltage during the sweep with a lock-in amplifier (at modulation frequencies above the cut-off frequency of the feed-back loop). In this way it is possible to measure directly the differential conductance signal and record a conductivity map of the surface ($dI/dV(x,y)$). dI/dV measurements can also be performed at tip-sample separation varied by a linear ramp, obtaining $dI/dz(x,y)$ contours (iii). Another STS measurement (iv) can be done at constant gap resistance were simultaneously the bias voltage and the current set-point are sweeped with the feed-back loop turned on, yielding a spectrum proportional to the normalized differential conductance $(dI/dV)/(I/V)$ were the dependence on the distance in the conductivity signal gets reduced. STS is thus a powerful method for investigating not only the local electronic structure but also the spatial distribution of the LDOS on a surface (for example electron standing waves and electron scattering on atomic scale structures, on steps, impurities or quantum corrals).

2.1.3 Scanning through insulators

In principle it should not be possible to perform STM measurements on insulating materials, but in reality STM can image insulators at elevated temperatures [37] or thin insulating films grown on conductive substrates [38]. The interest has been addressed to layers of organic molecules (up to 100 nm thick [39]), or to thin films of wide band gap insulators such as metal oxides (Al_2O_3, NiO, CoO, Ga_2O_3, CeO_2, MgO) [38] or more ionic materials as CaF_2 [40] and NaCl [41]. Although a complete and general picture of the thin insulator film electronic structure has no yet emerged, three possible ways of tunneling into insulating thin layers has been observed so far: (i) tunneling from the tip to the conduction band minimum (CBM) of the insulator, (ii) resonant tunneling via image states and (iii) electron tunneling from the substrate to the tip through the insulator. The first case (i) is possible when a large, positive sample bias is applied, so that electrons injected into the CBM pass through the insulator and prevent it from charging. In the case of CaF_2 on Si(111) the CBM lies about 3-5 eV above E_f and a stable tunneling current is obtained at a sample bias voltage ≥ 4 eV [40]. For the second case (ii), applying a large sample bias in a region between tunneling and field emission, one is able to obtain an enhanced tunneling into images states [42–44]. The origin of these states is due to the attraction between an electron approaching a metal surface and its image charge. These states are bound to a metal surface by the response of the substrate to the presence of the electron and kept outside the surface by the reflective properties of the substrate. The inverse dependence on distance from the surface of the image potential leads to a Rydberg-like series of states that converge to the vacuum level. The field produced by the STM tip induces a shift and an expansion of the image state spectrum. Since these states accumulate at the vacuum level, their energy position is tightly connected to the work function of the sample. Therefore when a metallic surface is partially covered by an insulator, due to the local work function changes, image states will appear at different energies (those of the insulator are lower than those of the substrate for a finite dielectric constant value). STM set at proper sample bias is thus able to identify the different species from the different contrasts in the images [42]. For example differential conductance spectra measured at a bias voltage of 3 eV for bare Ag(001) and partially covered with MgO, show two series of oscillations due to the first field resonance states which are shifted one with respect to the other [38]. A different contrast in the images is obtained when imaging at 5 eV, which is the second field resonance when tunneling through 1 ML of MgO on Ag(001). The MgO islands appear higher (0.3 nm versus 0.21 nm geometric height) than the Ag-Ag step. This resonant tunneling mode has been the key method to be able to image with STM a pure diamond single crystal (001) surface [45]. Tunneling is absent at voltages between -6 and 4 eV due to the insulating character of the diamond and this results in STM tip crashes, but at 5.9 ± 0.1 eV it is possible to tunnel into the lowest resonance above the vacuum level of the sample and resolve atomically the C(110)-(2×1) surface structure. In the third case (iii), since there are no electron states of an insulator accessible for the tunneling within its band gap, the tunneling is still possible from and into the substrate *through* the thin insulator layer. It has been found that the apparent height of insulator islands on the substrate has a strong dependence on the sample voltage within this range. They can appear as protrusions or depressions (as for NaCl grown on different substrates [41], MgO or CoO on Ag(001) [37]). Atomic resolution is often obtained for these films and usually the lattice of only one species is imaged. Calculations have shown that for ultra-thin films of NaCl evaporated onto Al single crystals, the anions (Cl^-) are imaged as protrusions instead of Na^+ atoms since they have a higher density of occupied states around the Fermi level [41]. The same has been demonstrated experimentally via electron-stimulated STM desorption experiments for NaCl on Cu(311) [46], where the STM tip has been retracted at 10 Å from the surface and a positive voltage (> 7 V) has been applied. In this way single Cl ions desorb from the surface and vacancies are imaged by STM. In a MgO layer on the Ag(001) surface, Mg ions are seen as protrusions when scanning at the insulator CBM, but at a bias voltage close to the Fermi level the Ag-substrate atoms are imaged [38].

2.2 Photoelectron Spectroscopy

Photoelectron spectroscopy is a technique that provides direct insight into the electronic properties of matter [47]. It is based on the phenomenon of photoemission detected at first by Hertz (1887) and explained by Einstein later on (1905) as a manifestation of the quantum nature of light. When a sample is illuminated, a photon with energy $h\nu$ can be adsorbed to lift an electron from a bound state into an unoccupied state with maximum final energy $h\nu - \phi$ (where ϕ is the work function of the material).

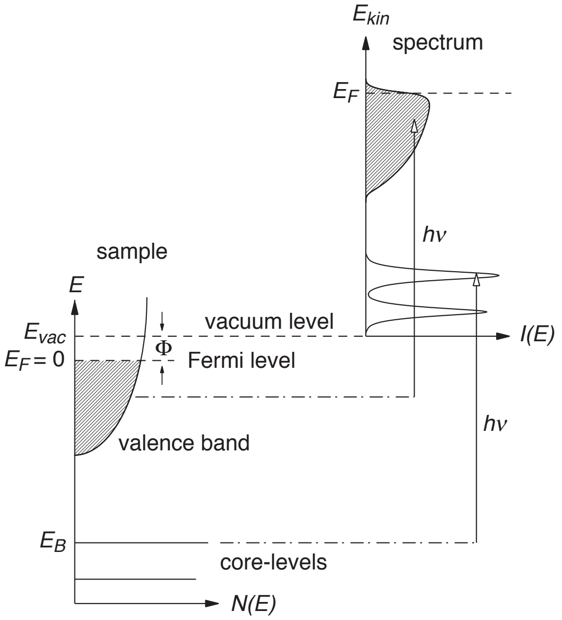

Figure 5: *Energetics of the photoemission process in the single-particle picture. Electrons with binding energy E_B can be excited above the vacuum level E_{vac} by photons with energy $h\nu > E_B + \phi$. The photoelectron distribution I(E_{kin}) measured by an analyzer gives in a first approximation a picture of the electronic density of states N(E_B) in the sample [47].*

In a modern photoemission experiment a gas discharge lamp, a x-ray tube, a laser or synchrotron radiation are used as monochromatized light sources. The light impinges on a sample, which is a gas or a solid, and electrons excited by the photoelectric effect escape into the vacuum in all the directions. They are then detected by an energy analyzer and characterized by their kinetic energy E_{kin} and their momentum $\hbar\mathbf{k}$. In an angle-resolved experimental-setup one measures E_{kin} of the photoelectrons as a function of the emission angle. Knowing the photon energy and the work function of the sample, one can determine the binding energy E_B and the momentum of the outgoing photoelectron as:

$$E_{kin} = h\nu - \phi - E_B, \tag{12}$$

$$k = \hbar^{-1}\sqrt{2m_e\, E_{kin}}. \tag{13}$$

The direction of the wave vector $\mathbf{k}$ is obtained from the polar (θ) and azimuthal (ϕ) angles under which the electron leaves the surface.

In Fig. 5 it is schematically sketched the relation between the energy levels in a solid and the electron distribution of the photoemitted electrons. The core levels of the sample are measured with photon energies in the soft x-ray range ($h\nu > 500\,\mathrm{eV}$), while the valence band is investigated with lower photon energies (ultraviolet range, $h\nu < 100\,\mathrm{eV}$) because of the superior energy and momentum resolution obtainable.

A theoretical interpretation of the spectra measured by PES is based on the expression of the photocurrent (J) produced [48]. The sample represents always a many-body system that is involved as a whole in the photoemission process, nevertheless as long as one is measuring a spectrum which is not strongly influenced by electronic correlation effects, or one is not interested in features as line shapes or satellites, then the simple single-electron picture is suitable (Fig. 5). On the basis of Fermi's Golden Rule (Eq. 5) as a result of perturbation theory in first order, J is the outcome of a photo-induced excitation of a system in the ground state Ψ_i to a final state $\Psi_f = \Psi_{k,s}$ which results in a photoelectron with energy and momentum given by Eqs. 12 and 13, and the remaining (*N-1*) electron system:

$$J_k(h\nu) = \frac{2\pi}{\hbar} \sum_s |\langle \Psi_{k,s} | H_{PE} | \Psi_i \rangle|^2 \; \delta(E_{kin} - E_s - h\nu). \tag{14}$$

The index s refers to a set of quantum numbers that contain all the possible excitations of the final state as phonons, plasmons, electron-hole pairs and multiple excitations. The operator H_{PE}, that describes the interaction of a spin-less electron of momentum $\mathbf{p}$ in the system with the electromagnetic vector potential $\mathbf{A}$, can be expressed as:

$$H_{PE} = \frac{e}{2m_e c}(\mathbf{A} \cdot \mathbf{p} + \mathbf{p} \cdot \mathbf{A}) + \frac{e^2}{2m_e c^2} A^2 \sim \frac{e}{m_e c} \mathbf{A} \cdot \mathbf{p}. \tag{15}$$

The right hand simplified expression for H_{PE} takes into account that the quadratic term in $\mathbf{A}$ is relevant only for extremely high photon intensities, usually not produced in standard laboratories and that $\mathbf{A}$ is constant over atomic dimensions in the UV regime. For the calculation of the spectrum an important simplification is usually made: the *sudden approximation*. In this limit the photoelectron is instantaneously removed from the sample and the effective potential of the system has a discontinuous change at that moment. Therefore in the final state (Ψ_f) the photoelectron is decoupled from the remaining solid, so that all the extrinsic interactions are neglected. The final state in Eq. 12 has to be replaced by $|\Psi_{k,s}\rangle = |k; N-1, s\rangle \rightarrow c^+_{k,s}|N-1, s\rangle$ using the creation operator (c^+_k) for the photoelectron with momentum k and energy E_{kin}. J becomes then:

$$J_k(h\nu) = \frac{2\pi}{\hbar} \sum_\kappa |\Delta_{k\kappa}|^2 A^<_\kappa(E_{kin} - h\nu) \tag{16}$$

where $\Delta_{k\kappa} = |\langle \Psi_k | H_{PE} | \Psi_\kappa \rangle|$ is the photoemission matrix element that describes the transition probability of a single electron from a state Ψ_κ into the final state Ψ_k, and $A^<_\kappa(E_{kin} - h\nu) = \sum_s |\langle N-1, s | c^-_\kappa | N \rangle|^2 \; \delta(E_{kin} - E_s - h\nu)$ is the one-electron spectral function which describes the probability of removing (in this expression) an electron with momentum κ and energy $E_{kin} - h\nu$.

2.2.1 Angle Resolved Photoelectron Spectroscopy

Angle-resolved photoemission data are usually discussed within the *three step model*, which although purely phenomenological, has been proven to be very successful [49]. In this approximation the photoemission process is described as a sequence of (i) the optical photoexcitation of a band electron into an empty band, (ii) the propagation of this excited electron to the surface and (iii) its refraction at the surface potential barrier and escape into the vacuum (Fig. 6).

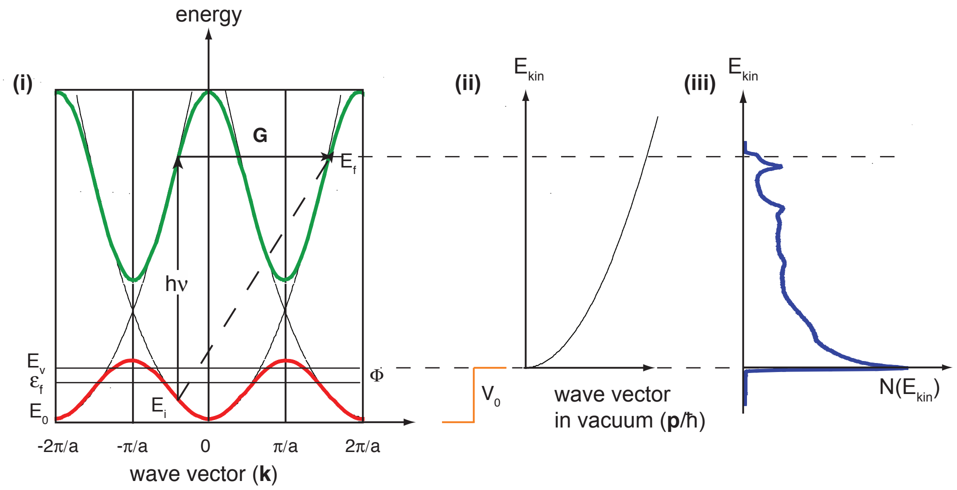

Figure 6: *Diagram of the free electron final-state model for ARUPS. (i) An optical transition between two bands in a nearly free-electron band structure is indicated. In the reduced scheme it appears as a vertical transition. It corresponds in the extended zone scheme to a non-vertical transition between two points which differ by a reciprocal lattice vector* **G**. *(ii) The final-state wave vectors in this model are obtained by the intersection of a free-electron parabola with its zero energy (E_0) at the bottom of the valence band and the final energy E_f. The wave vector of the photoelectron in vacuum is then given by the intersection of a free-electron parabola laying on the vacuum level E_v and the final state energy E_f. (iii) Typical photoelectron spectrum were the photoelectrons distribution is recorded as a function of their kinetic energy ($E_{kin} = \varepsilon_f - \Phi$). The inelastically scattered and secondary electrons are responsible of the broad peak appearing at low energies.*

In the photoexcitation process (i) from an initial state with energy E_i and momentum $\hbar\mathbf{k}_i$ to a final state (E_f, $\hbar\mathbf{k}_f$), the energy, momentum and spin of the photoelectron are conserved. If the photon energy at a given value of the wave vector $\mathbf{k}_i$ is equal to the difference between an occupied initial state and an unoccupied final state, then the photoemission is at resonance and a *direct* transition can be observed if the final state propagates into the vacuum. Since the photon wave vector is only a percent of typical

Brillouin zone dimensions, then its momentum is neglected and a reciprocal lattice vector **G** is needed in order to provide the momentum for the electron to escape from the crystal:

$$\mathbf{k}_f = \mathbf{k}_i + \mathbf{k}_G. \tag{17}$$

In the propagation to the surface, step (ii), the photoelectron is involved in processes as elastic and inelastic scattering or diffraction, but these mainly modify the transition intensity and width but do not change the position in **k**-space. Step (iii) is described by the transmission through the surface potential step, expressed by the inner potential V_0. The component of the wave vector parallel to the surface ($\mathbf{k}_{\parallel}$) is conserved, while the perpendicular component ($\mathbf{k}_{\perp}$) is reduced. If one can make the assumption that the photoelectron is excited in a free-electron-like final state in the solid, and one measures free electrons in vacuum, then the respective energies are:

$$E_f = \frac{\hbar^2 \mathbf{k}_f^2}{2m_e}, \quad E_{kin}^{vac} = \frac{\hbar^2 \mathbf{k}_{vac}^2}{2m_e} \tag{18}$$

and the momentum of the electron in its initial state can be found by measuring E_{kin}^{vac} Eq. 12 and the polar angle θ relative to the sample surface normal:

$$k_{\parallel}(\text{Å}^{-1}) = \hbar^{-1}\sqrt{2m_e E_{kin}^{vac}}\ sin(\theta) = 0.5123\sqrt{E_{kin}^{vac}(eV)}\ sin(\theta) \tag{19}$$

$$k_{\perp} = \hbar^{-1}\sqrt{2m_e(E_{kin}^{vac} + V_0)}\ cos(\theta_{solid}) \tag{20}$$

where θ_{solid} is the polar emission angle inside the solid. Considering the conservation of $\mathbf{k}_{\parallel}$ parallel (Eq. 19), one arrives at the equivalent of Snell's law of refraction to quantify θ_{solid} as:

$$sin(\theta_{solid}) = sin(\theta)\sqrt{\frac{E_{kin}^{vac}}{E_{kin}^{vac} + V_0}}. \tag{21}$$

Eq. 20 states that a wave vector can be measured only if its perpendicular component $k_{f_{\perp}} > \hbar^{-1}\sqrt{2m_e V_0}$, this limit is known as photoemission horizon. In 2D systems, $\mathbf{k}_{\parallel}$ is conserved rigorously while the final state can pick up any value of $\mathbf{k}_{\perp}$ since this component is not quantized. Examples of these systems are ultrathin films or surface states, while atomic or molecular arrangements on surfaces are quasi-2D systems because their interaction with the substrate is never completely negligible. A peculiar situation arises when overlayer and substrate have different periodicities. In this case the electronic states of the overlayer have the periodicity of the overlayer reciprocal lattice the size of which is different from that of the clean substrate and *umklapp* effects can be detected. Two particular types of photoemission data will be presented in this work and an example is illustrated in Fig. 7. In the first case full photoemission spectra are taken in a given range of polar or azimuthal angles and are then plotted as binding energy vs. wave

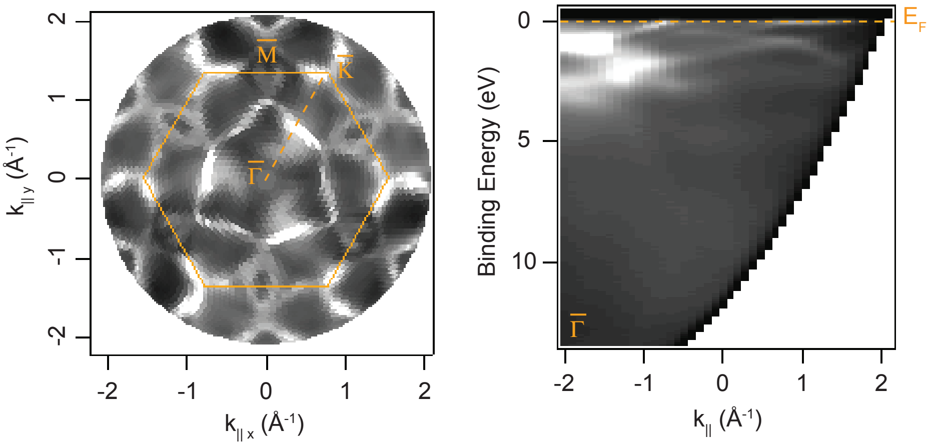

Figure 7: *On the left, He Iα Fermi surface map of the Rh(111) surface. On the right, He Iα excited dispersion plots in the $\overline{\Gamma K}$ plane for the same surface. The zero energy value corresponds to the Fermi energy. White corresponds to high intensity.*

vector (or angle). In this way it is possible to measure the band dispersion in a particular direction in the reciprocal space. For each binding energy the sampled k-vectors move in the reciprocal space along a circular line of radius:

$$k_f = \hbar^{-1}\sqrt{2m_e(E_{kin}^{vac} + V_0)}. \tag{22}$$

Every intersection point between the initial state band with periodicity of the reciprocal lattice and the final state with wave vector $\mathbf{k}_f$, indicates a direct transition for a particular binding energy, and high photoemission intensity is measured. In the second case measurements of constant energy maps are taken detecting the photoelectrons of a chosen binding energy at all the possible emission angles (θ and ϕ) on the hemisphere above the sample surface. Here the sampled $\mathbf{k}$-vectors move along a sphere with radius given by Eq. 22 and centered at the origin of the reciprocal space. Since constant energy surfaces are continuous in the three-dimensional space, the intersections between initial and final states will be measured as high intensity continuous lines in a parallel projected plot [50].

2.2.2 X-ray Photoelectron Spectroscopy and Diffraction

X-ray photoelectron spectroscopy (XPS) is an ideal tool for the chemical investigation of surfaces and thin films, known also as ESCA (electron spectroscopy for chemical analysis) since 1967 (from Siegbahn [52]). The continuous development and interest for this technique produced a deep knowledge on photoemission cross sections of most elements,

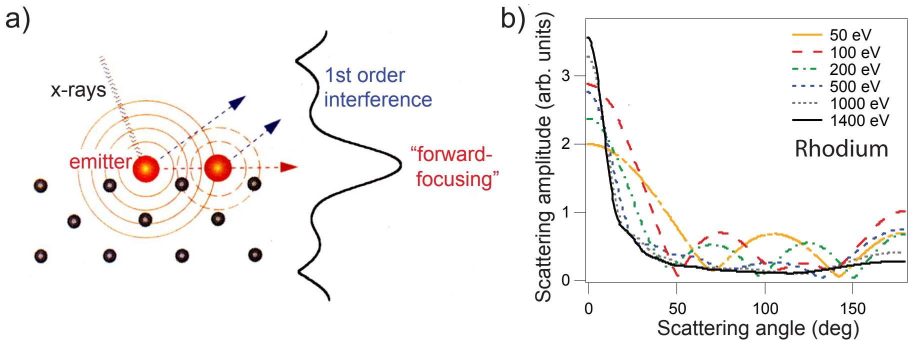

Figure 8: *(a) Schematic illustration of the process involved in photoelectron diffraction [51]. (b) Scattering amplitude calculated for an electron plane wave incident on a Rh atom at different kinetic energies.*

core-level binding energies and chemical shifts, so that nowadays it is relatively easy to analyze an XPS spectrum quantitatively and determine the elemental composition of a sample with a precision of a few percent. Besides the detailed atomic composition that can be achieved with the analysis of core levels by XPS, it is possible to study the atomic structure (i.e. the atomic positions) using x-ray photoelectron diffraction (XPD) [53]. The physical principle of this technique, schematically reproduced in Fig. 8(a), is based on the strong forward scattering, or focusing, that occurs when x-ray photoelectrons emitted by near-surface atoms are coherently scattered by the surrounding atoms in the lattice. This scattering process (Fig. 8(a)) produces enhanced intensities at polar and azimuthal angles corresponding to the directions connecting the emitting atom with the nearest- and next-nearest neighbor atoms. Since the core-level peaks are element dependent, the observation of the directions in which their intensities are enhanced gives information on the short-range ordering around a particular atomic species. Individual electron-atom scattering processes are strongly dependent on the kinetic energy of the photoelectron (Fig. 8(b)). Most XPD experiments are performed in the higher kinetic energy range or forward focusing regime. As can be seen in Fig. 8(b), at energies higher than 500 eV forward scattering dominates and one finds that the photoelectron angular distribution is, to a first approximation, a forward-projected image of the atomic structure around the photoemitter. Besides this, one has to take into account that in some cases interference effects, that occur between amplitudes from different scatterers, can be very strong and can be directly used to calculate bond distances [51]. Below 200 eV the scattering process becomes more isotropic and interferences of orders higher than zero become predominant. Sometimes the backscattering (at 180°) turns out to be more useful to identify bond directions and surface structures [54].

A theoretical description of the photoelectron diffraction process can be schematically summarized in several steps [51]. In the first one (i) a photon impinging on an atom (emitter) excites a photoelectron which is emitted as a spherical wave $exp(ikr)/r$ with a given angular momentum symmetry (of quantum numbers l, m), (ii) this wave is then involved in single- and multiple-elastic scattering processes with the surrounding atoms (process described by a complex scattering factor $f_j(\theta_j)$). During its propagation to the surface (iii) the wave amplitude is attenuated by inelastic processes (the inelastic mean free path Λ_e quantifies this step) and (iv) thermal vibrations are responsible of the reduced degree of coherent elastic scattering processes (expressed by temperature-dependent mean-square atomic displacement $< u_j^2 >$ of the emitter and the scatters and modeled by a Debye-Waller factor). The primary emitted wave and the scattered ones are then (v) refracted at the surface-potential step (V_0) and (vi) their coherent superposition is detected by an analyzer. In order to simulate experimental XPD patterns, one of the most popular theories is the *single-scattering-cluster theory* (SSC) derived by Lee [55] and developed by others [56], which is relatively simple and usually gives good agreement between experimental and theoretical results. In SSC the intensity from one chosen photoemitter in an atomic cluster is written as the square of a coherent sum of a primary, unscattered photoelectron wave and all the singly-scattered amplitudes from all the neighboring atoms. In its simplest form, the plane-wave (PW) approximation, the scattering of the electron wave is described by the factor $f_j(\theta_j)$ that can be obtained from the values of partial-wave shifts. These can be calculated by means of the MUFPOT program by Pendry [57] which uses a muffin-tin potential in order to represent the scatterer in the solid surface investigated. A further step in the development of theoretical simulations of complex XPD data, is given by the consideration of multiple scattering events treated in MSC theory. These effects are important especially for the emission along a chain of atoms. In a single-scattering theoretical model it is predicted that, even if a number of scatterers is present in front the emitter, a strong enhanced intensity can be detected along the chain-axis. On the other hand, a multiple scattering model predicts that only if a certain number of atoms is present in front of the emitter there will be enhancement, otherwise if they are too many only the first atoms in a row tend to be forward focusing while the others will be responsible for ‘defocusing’ effects [58].

2.3 Experimental setup

The experiments presented in this thesis have been performed in an ultra-high vacuum (UHV) system with three separable chambers equipped with their own pumping and pressure reading systems, but joined together via VAT vacuum-valves (Fig. 9). In this way the same sample can be transferred in vacuum from one to the other chamber without

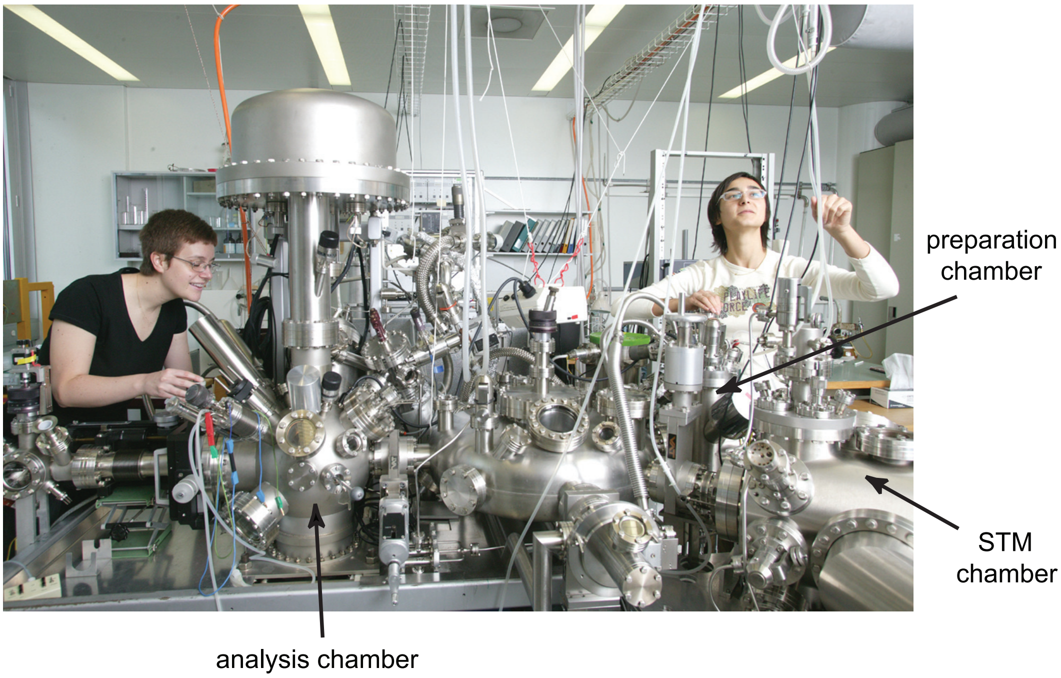

Figure 9: *Experimental system.*

being exposed to air. The *preparation chamber* is furnished with standard sample preparation facilities: a sputter gun (with Ar^+ ions), a sample heating and cooling stage with a movable thermocouple to read the sample temperature, a quadrupole mass spectrometer, several evaporation sources (for metals or molecules) and leak-valves to introduce into the vacuum gases and vapors from molecules in the liquid state. The possibility to isolate this chamber from the rest of the system has been implemented recently, in order to perform experiments with high pressure gas exposures. A rear-view LEED is mounted for surface characterization. The photoemission experiments are performed in a μ-metal *analysis chamber* which houses a commercial VG-ESCALAB 220 electron spectrometer (Vacuum Generators). Three x-ray sources (Mg Kα: $h\nu$=1253.6 eV, Si Kα: $h\nu$=1740 eV and monochromatized Al Kα: $h\nu$=1486.6 eV) and a monochromatized high-flux He discharge lamp (Gammadata VUV5000) are used in this chamber to excite photoelectrons. The UV-radiation lines are selected by a toroidal grating monochromator that focuses the light on a 2 mm aperture towards the sample surface. Two differential pumping stages provide a final He partial pressure of $\sim 5 \times 10^{-9}$ mbar during the measurements. The electrostatic analyzer, of 150 mm mean radius, is equipped with six channel electron multipliers, allowing count rates up to 5 Mcts/s with a constant detector efficiency [59, 60]. A lower limit of 23 meV (FHWM) for the energy resolution achievable has been estimated from the linewidth of He Iα excited Ar 3p gas phase spectra at a partial pressure of 10^{-5} mbar at an analyzer pass energy of 30 meV. The angular resolution ($\Delta\theta$) can be varied by means of two iris apertures from 12° to 1° FWHM, and a lower limit value of $\Delta\theta < 0.8^\circ$ (FWHM) has been determined from the width of angular distribution curves of the Shockley surface state on Cu(111) [61]. Samples can be cooled by means of a liquid He flow cryostat to 100 K and heated resistively up to 900 K during data acquisition.

In this experimental setup, in order to measure XPD patterns and ARUPS dispersion maps, the analyzer is maintained at a fixed position while the sample is rotated. Each sample is mounted on the manipulator in a home-built, two axis goniometer that allows to reach all the electron emission angles in the hemisphere above its surface with a reproducibility better than 0.2°. In spherical coordinates the polar emission angle (θ) is the angle between the spectrometer direction and the sample surface normal, while the azimuthal angle (ϕ) is the one between the projection of the detection direction on the surface and an arbitrary defined direction in the sample surface. The angle scanning is done by computer controlled stepping motors that drive the two axis goniometer, in such a way that the measurements in an XPD experiment start at grazing emission angles ($\theta = 88^\circ$) and the polar angle is reduced after each full 360° rotation of the crystal. The azimuthal step size at any θ is chosen so that the sampling density in solid angle is uniform; typically 5000 angles are mapped. The detected intensities $I(\theta, \phi)$ are visualized as a gray-scale image where brighter spots correspond to high intensity and are plotted in stereographic projection. In this way the radius at which a diffracted feature appears is proportional to $tan(\theta/2)$, therefore circular features in a diffraction pattern are seen as true circles on the projection plane. In the same way constant energy maps as Fermi surface maps, are measured. The position of the Fermi level E_F for each experiment is determined by fitting with a Fermi-Dirac ($f(E)$) function a measured UPS spectrum of a Ag polycrystal at normal emission. $f(E)$ is defined as: $f(E) = I_0 + I[exp((E - E_F)/kT_{eff})]^{-1}$, where I_0 and I are the intensities far above and below E_F, respectively, and T_{eff} describes the width of the Fermi edge which depends on the real sample temperature and the experimental resolution [62]. In order to record dispersion plots, full energy spectra are taken keeping the azimuthal angle ϕ fixed while varying the polar angle θ or vice versa. From the resulting two-dimesional binding energy vs angle (or momentum) plots it is possible either to extract single spectra at a specific angle (known as energy distribution curves, EDC), or to monitor the intensity variation at a fixed binding energy as a function of the angle (known as angular distribution curves, ADC), or momentum distribution curves (MDC).

The STM experiments are carried out with a room temperature VPII scanning probe from Park Scientific Instruments (now incorporated in ThermoMicroscopes). The microscope is mounted on a home-built, vibration-isolated table with three legs in an independent UHV chamber (*STM chamber*). A system of two *DN63CF* bellows with different

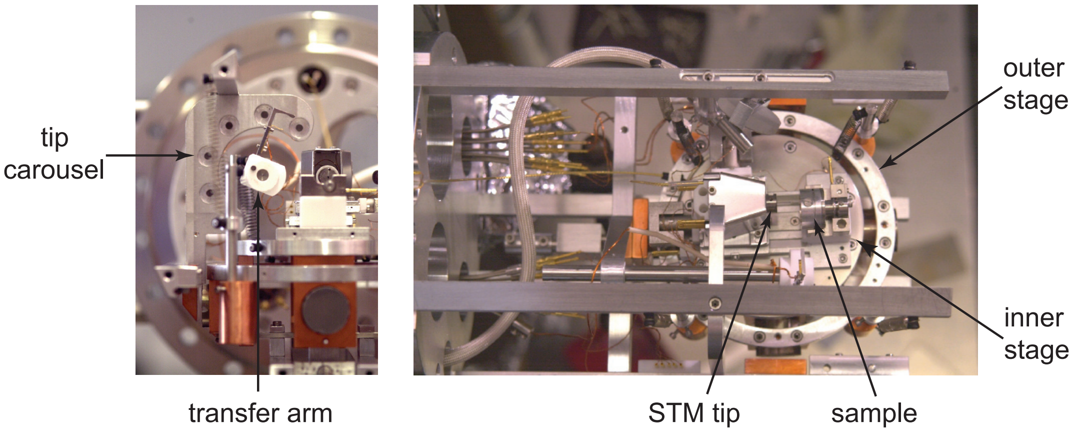

Figure 10: *On the left, front view of the STM stage. In this picture the arm used for tip exchange and the tip carousel were are placed the magnets supporting the tip holders, are visible. On the right, top view of the VPII-STM.*

properties (diameter, number of membrane pairs and spring constant) to avoid common eigenfrequencies has been designed to join the STM chamber to the VAT-valve towards the preparation chamber [63]. In this way the instrument has been well decoupled from the vibrations produced by the instruments running in the other chambers and atomic resolution is obtainable. In this type of STM, the tip scans horizontally on the sample surface. The tip is magnetically held on a 10 μm-tube scanner for x-y-z movement which is placed on a x-z inertial drive translation stage which allows movements of a few mm relative to the sample, so that different spots on the surface can be imaged (Fig. 10). The tips can be exchanged without breaking the vacuum via a transfer arm, and at most six tips can be stored in a tip carousel in the STM stage. The sample holder is set horizontally on the measuring position by a wobble-stick and is held in place by friction and gravity on three metallic pins in a cradle. Both the sample and the scanner are mounted on a two-stage, double-spring suspended platform with magnetic eddy current damping so that an efficient vibration isolation is provided during measurements. A preamplifier outside the vacuum converts the tunneling current into a voltage signal which is amplified by a gain of 10^8 (0.1 V per nA). The bias voltage is applied to the sample (V_s).
All STM images taken at room temperature have been recorded at the University of Zurich, in constant current mode and with tungsten (W) tips that were electrochemically (NaOH) etched. An useful means of tip preparation consists in applying soft and hard crashes to the tip while scanning on clean metal surfaces. STM images recorded at 77 K have been measured with a Low Temperature (LT) Omicron STM at the Laboratories of EMPA Thun in Switzerland. Etched and cut Pt-Ir tips were used for LT

measurements. Surface x-ray diffraction experiments (SXRD), briefly discussed in this work, were performed at the Materials Science (MS) beamline at the Swiss Light Source (SLS).

Besides single crystals of some transition metals, also thin films have been used in this work. The Rh(111), Ir(111) and Ru(0001) thin films, 40 to 150 nm thick, grown on $Al_2O_3(0001)$ were produced at the University of Augsburg (DE) by Dr. Matthias Schreck and Stefan Gsell. The borazine ($(HBNH)_3$) was synthesized by PD. Dr. Hermann Sachdev and Dr. Dirk Bentz at the University of Saarland (DE).

3 Hexagonal boron nitride: the white graphite

Boron nitride (BN) can be found in different crystalline phases: cubic zincblende, wurtzite or hexagonal. The hexagonal layered structure (h-BN or α-BN) is the most common form of BN. It is an insulating material; published values for its band gap range from 3 to 7 eV and it is not yet established if it is direct [64] or indirect [65]. It possesses outstanding properties such as high chemical inertness, high thermal conductivity, high resistance to thermal shock and to corrosion and low thermal expansion coefficient [66]. Therefore h-BN can be used in a large variety of applications: in metal machining [66], as a protective coating material of metals, to produce parts used in high temperatures situations (it has a melting point $> 3000\,\mathrm{K}$), as well as in electronic insulation components and can be added to other materials to improve vibrational damping [67]. Due to the ease of sliding between its basal planes, h-BN is a good solid lubricant for reducing wear and friction in machining processes [68] and further applications include h-BN in optical waveguides [69]. h-BN can be synthesized in different ways: by the traditional sintering and hot pressing sintering [70], by the combustion synthesis technique [71], by the reaction of boron-based and nitrogen-based compounds [66], or by chemical vapor deposition (CVD) as a thin film onto a substrate [72].

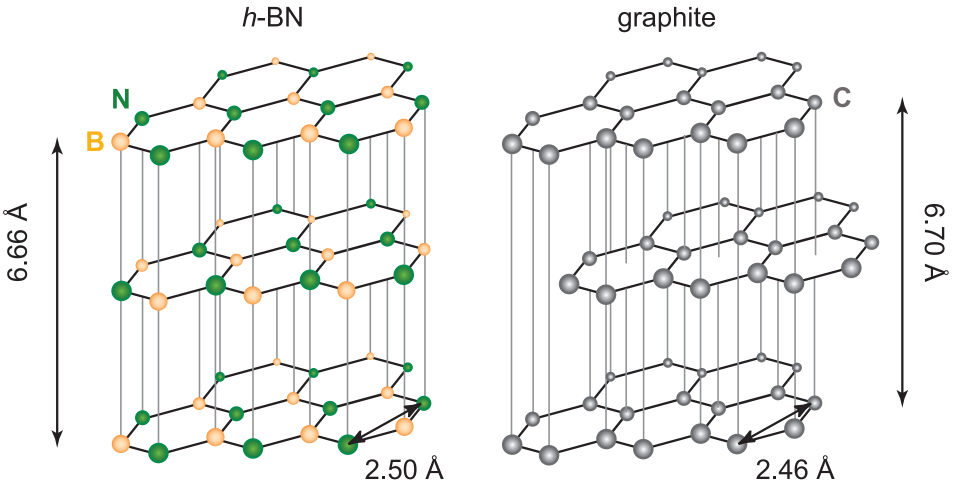

Figure 11: *Schematic crystal structures of hexagonal boron nitride h-BN and graphite. Solid h-BN has a white color in contrast to the black graphite.*

Hexagonal BN has a similar structure to graphite, in which alternating boron (B) and nitrogen (N) atoms, instead of carbon (C), construct a bidimensional honeycomb network forming the basal plane. In-plane bonds between adjacent N and B atoms are a mixture of ionic and strong sp^2-covalent character with electron localization closer to N than to B. The basal planes interact weakly with each other via van der Waals bonds and ionic interaction between oppositely charged ions. In fact, in the most probable structural model for bulk *h*-BN [73], for neighbouring basal planes there is not a Bernal stacking (as for graphite) but the planes lie in registry with each other and each B (or N) atom in one layer is located directly on top of a N (or B) atom in the neighboring ones. The in-plane lattice constants of *h*-BN are very similar to those of graphite, with $a_0 = b_0 = 2.50 - 2.51\,\text{Å}$ and $c_0 = 6.66 - 6.67\,\text{Å}$ [73, 74]. As for graphite, nanotubes are also allotropes of *h*-BN. The strong anisotropic character of their in-plane and out-of-plane bonds is exhibited also in many physical properties such as electrical and thermal conductivity, in the energy band structure and in the surface energy. The (0001) surface parallel to the basal plane has the lowest energy with respect to the others, therefore *h*-BN and graphite preferentially grow on a solid surface with their basal plane.

The research of a possible implementation in technological applications of thin films (up to a few monolayers) of these layered materials has widely spread in the last years. For example, recent studies have addressed the transport properties of ultrathin epitaxial graphite (i.e graphene) grown on the SiC(0001) surface [75]. Experiments demonstrate that these properties are dominated by the single epitaxial graphene layer at the silicon carbide interface. Moreover this structure can be patterned with standard nanolithography methods and shows quantum confinement of electrons and phase coherence lengths beyond 1 µm at 4 K and 500 nm at 58 K, with mobilities bigger than $2.5\,\text{m}^2/\,\text{V}\,\text{s}$. These promising results indicate the possibility to construct coherent epitaxial graphene electronic devices at the nanometer scale and at high temperatures, based on the wave-like properties of electron and holes (as interference-based electronic switches). Low dimensional graphitic structures as this one exhibit most of the electronic properties of carbon nanotubes but their advantages are that, due their 2D character, one could integrate them in large-scale ballistic-devices with optimal methods and one could use them in molecular electronics. In fact, differently from nanotubes, in planar graphene it is possible to dope the dangling-bonds at the edges with donor or acceptor molecules thus tuning the electronic properties without affecting the graphitic backbone of the device.

3.1 *h*-BN thin films on different surfaces

Boron nitride films have been deposited onto a variety of substrates either via precipitation methods (i) [76] or most commonly via chemical vapor deposition (CVD) (ii). In the second case (ii), either two different boron and nitrogen containing source gases (as NH_3+B_2H_6, NH_3+BF_3 or BCl_3, NH_3+H_3BO_3, B+NH_3), or compounds which present both elements (as borazine $(HBNH)_3$ or substituted borazines as $(ClBNH)_3$ or $(ClBNCl)_3$), have been used. From these source gases boron nitride films form either via thermal decomposition or by using highly reactive conditions (such as plasma or ion processing). Precipitation (i) has been used for example on single-crystals and polycrystalline samples of **Fe-37Ni alloy** doped with nitrogen and boron (through separate elevated-temperature chemical treatments) [76]. The system has been investigated using Auger electron spectroscopy (AES) and LEED. The in-plane room-temperature lattice constant on the (111) surface of this alloy is 2.54 Å and the misfit with *h*-BN is only 1.5% therefore an epitaxial growth is expected. Precipitation was induced by annealing for 25 min the *h*-BN oversaturated samples at $1273 - 1333\,\mathrm{K}$, then rapid cooling down to RT and subsequently it was heated to a holding temperature between 923 and 1123 K. A few cycles were needed to obtain surface precipitation and a substantial decrease in the nitrogen concentration in the alloy occurred after 20-50 heating cycles. Some samples were sputtered in the cooling down step. For all the cases it was found that *h*-BN grows epitaxially on the (111) surface and the atomic model proposed suggests that boron and nitrogen occupy hollow sites on the substrate. Long annealing induces sulfur atoms to segregate on the interface between the *h*-BN overlayer and the substrate (demonstrating that the bonding within the *h*-BN layer is strong while the *h*-BN/substrate bonding is weak). For polycrystalline material and for samples that were not cooled to RT but kept at a holding temperature of 1048 K after heating, several *h*-BN rotational domains were found on the surface and seen as rings on LEED patterns. Studies on the stability of *h*-BN on Fe-37Ni alloy show that once the structure is formed, further annealing between 1028 and 1108 K for periods ranging from 1127 to 6043 min, do not enhance the precipitation and the film is saturated. Moreover the structure survives heating to temperatures between 1088 and 1238 K.

If two different B and N compounds are used in CVD (ii) to grow BN films, a detailed study of their behavior in the adsorption on the clean metal surface is often needed in order to understand their coadsorption. For the synthesis of BN films on **Ru(0001)** for example, the use of ammonia (NH_3) as group-V reactant and diborane (B_2H_6) as group-III reactant is not recommendable [77]. In fact the extremely high chemical stability of ammonia, induces a low reactivity with diborane in UHV. A suitable substitute turned out to be hydrazine (N_2H_4), so that BN adlayers with a stoichiometry 1:1 could be formed by its simultaneous coadsoprtion with B_2H_6 at 450 K or at 90 K and post-annealing at 450 K [78].

In CVD borazine and substituted borazines have the advantage of 1:1 B:N stoichiometry already built into the adsorbate for the growth of BN thin films. Therefore several experiments have been carried out using these precursors. Infrared reflection absorption spectroscopy (IRAS) and high resolution electron energy loss spectroscopy (HREELS) studies were involved in understanding the behavior of borazine molecules on different surfaces. For example if 10 L of borazine are dosed at 170 K on a clean Pt(111) surface, the molecules are adsorbed perpendicular to the surface, thus the bonding is mainly due to the N atoms from the BN-ring in the molecules which share their electrons in a σ-type bonding with the empty states in the Pt *d*-band [79]. The opposite appears for $(HBNH)_3$ on **Au(111)** [80]. If $<$ 1 L of borazine is exposed on the Pt(111) surface previously covered by one layer of *h*-BN, then the molecules are adsorbed parallel to the surface and the bonding is of π-type.

A conjugate study of adsorption and decomposition of $(HBNH)_3$ at the **Ru(0001)** and **Pt(111)** surfaces has been done with AES, thermal desorption mass spectroscopy (TDMS), XPS, electron energy loss spectroscopy (EELS), LEED and low energy ion scattering spectroscopy (LEISS), over a wide temperature range of $140 - 1200$ K [81]. The RT adsorption of borazine is shown to be irreversible on both surfaces and TDMS data and AES experiment suggest that there is an higher degree of borazine dissociation at RT on the Pt(111) surface as compared to the Ru(0001). With a RT borazine exposure no ordered LEED patterns are observed on the surfaces. On the contrary if the exposure to $50 - 100$ L of borazine is done at 1000 K, then ordered structures appear. The adsorbed BN layer is inferred to lie flat on the surface with a layer distance from the substrate equal to the *h*-BN bulk interlayer spacing (3.3 Å). For *h*-BN on Pt(111) the LEED patterns show a coincidence lattice with periodicity of (10×10) Pt lattice constants (2.77 Å), and the estimated coverage is 1.22 ML. In the case of *h*-BN on Ru(0001) the coincidence appears at (12×12) Ru lattice spacings (2.71 Å) and the estimated coverage is 1.16 ML. These structures are found to be stable at least up to 1250 K.

The ordering of *h*-BN on **Pt(111)** has been characterized also by other experimental studies were $(ClBNCl)_3$ has been used as precursor [82]. In this case not only BN domains in which the orientation of the B and N atomic lattices coincide with that of the substrate are found, but also domains rotated by 30°. In this way the adlayer is found to be less strained on the surface.

The interaction of $(HBNH)_3$ with the exposed surface does not always result in the formation of *h*-BN layers, as it happens in the case of **Re(0001)** [83]. A detailed study with LEED, TDS, AES, and EELS shows that borazine forms physisorbed multilayers on Re(0001) at 115 K. These multilayers desorb at $\sim$ 200 K and leave on the surface less than 1 ML of chemisorbed borazine. An annealing to 570 K induces the dissociation into atomic nitrogen and boron and the desorption of hydrogen appears in TDS spectra. The nitrogen atoms form a (2×2) structure as seen in LEED patterns which leaves the surface at temperatures $>$ 1200 K; the borons form a $(\sqrt{3} \times \sqrt{21})$ structure stable up to temperatures $>$ 2100 K. The nitrogen structure is seen only for low borazine exposures $<$ 1 L and subsequent annealing to 801 K, while the boron structure forms at any coverage up to 40 L after an annealing at temperatures $> 1194\,\mathrm{K}$. However a boron-nitrogen compound can be produced on this surface by the decomposition at 115 K of borazine-multilayers, due to the irradiation of the 2 keV e^-–beam in the AES measurements. The resulting boron-nitrogen compound is stable up to 1500 K.

3.2 The Nickel case

The adsorption of BN on Ni is one of the most studied systems. The Ni bulk lattice constant of 3.5 Å favors the growth of *c*-BN (3.6 Å), but *h*-BN has been found instead. The adsorption on the Ni(111) surface is lattice matched with *h*-BN. The Ni in-plane lattice constant is 2.49 Å, therefore the lattice mismatch between a *h*-BN adlayer on this surface is only +0.6% which favors its unstrained pseudomorphic epitaxial growth.
Several experiments and various techniques have been used to characterize the structural and electronic properties of *h*-BN layers on Ni(111). The formation of a single *h*-BN layer on the surface is easily obtained with the deposition of 100 L of borazine at a substrate temperature around 1050 K, but the growth of further layers is very slow. A second *h*-BN layer could be grown with 6×10^3 L of borazine while for a multilayer 1×10^5 L are necessary [84]. It is suggested that the growth of the BN is not proceeding in a layer-by-layer fashion after the formation of the first layer, but in a Stransky-Krastanow mode [85]. The atomic structure proposed first as a result of LEED intensity analysis [86] and confirmed then by XPD, STM [87] and DFT [88,89], consists of N atoms adsorbed on top of Ni atoms, while the B atoms preferentially occupy *fcc* adsorption sites. The *h*-BN layer is slightly buckled by about 0.1 Å with the B atoms closer to the Ni surface than the N atoms [88], and the distance adlayer/substrate is ~ 2 Å. While there is a general agreement on the structural properties of the *h*-BN on Ni(111) interface, the strength of the chemical bonding remains still controversial. In fact, in the electronic valence band structure measured by ARUPS, the bands due to the single *h*-BN layer (ie. one σ band and one π band at $\overline{\Gamma}$) do not cross neither the Fermi level (E_f), nor the *d*-bands of the substrate. This suggests that the layer is insulating and physisorbed. A similar behavior has been found also for *h*-BN on **Pt(111)** and on **Pd(111)**, but the π band in the Ni case has higher binding energy by 1 eV [90,91], indicating a stronger bond in the system. These conclusions were also derived from the comparison with similar measurements for MG on Ni(111) where it is found that the π states (especially those with energies near E_f) are hybridized with the Ni *d*-states, which leads to the formation of a covalent bond between overlayer and substrate [85]. Nevertheless a change in the work function due to the adsorption of *h*-BN is a fingerprint of the interaction between *h*-BN and nickel, suggesting that the *h*-BN layer gets polarized. Charge is transferred to the substrate and electrons can tunnel across the vacuum/*h*-BN/Ni(111) interface in

STM measurements [88]. On the other side, HREEL studies explain the strong difference in the spectra measured for *h*-BN on Pt(111) and on Pd(111) with respect to those of *h*-BN on Ni(111) as involving a hybridization of the π electrons with the *d* electrons of Ni. The same result is also coming from measurements done with several core-level spectroscopic techniques based on sychrotron radiation: soft x-ray absorption (XAS), core-level photoemission (PE) and resonant Auger spectroscopy (RAS) [84]. In all the spectra measured a strong orbital hybridization between the Ni $3d$-states and *h*-BN states has been observed. This system is even defined as 'strongly chemisorbed' with respect to *h*-BN on **Cu(111)** were a weak metallicity explains the near edge x-ray absorption fine structure (NEXAFS), photoemission/Auger and work function data [92].

BN layers have been grown on **Ni(100)** using ammonia and diborane. They have been characterized with different techniques [93]. TDS and XPS data indicate that the interaction to form BN occurs through an intact B_2H_6 monolayer and NH_3 multilayers when the sample is exposed to 5 L of NH_3 followed by 15 L of B_2H_6 at 100 K and then annealed to 250 K. This interaction is responsible for the two binding energy states of B-containing species as found in XP spectra (at 187.7 eV and 189.6 eV binding energy). An annealing to 1000 K results in the formation of a BN compound appearing in the strong enhancement of the B peak bound to N and in a shift in the peaks towards the values measured for *c*-BN and *h*-BN films (ie. for the N $1s$ from 397.5 to 398.5 eV and for the B $1s$ from 189.6 to 190.1 eV). This BN phase is not ordered on the surface (as seen with LEED) and desorbs at 1200 K. If the two gases are dosed at higher temperatures (950 K) an ordered structure with (1×7) periodicity forms, and a further annealing to 1100 K sharpens the LEED pattern. A simple model with a slightly stretched *h*-BN layer on the Ni(100) surface is suggested to match this overstructure periodicity. XPS measurements show that the BN coverage saturates at 1 ML and longer exposures in UHV do not allow to reach more than 1.5 ML. This structure has been found to survive upon air exposure. The stability of samples left in atmosphere for several days has been demonstrated by the presence of a weak (1×7) structure on the LEED patterns that could be sharpened by annealing to 1100 K. Using metal-organic-chemical-vapor-depostition (MOCVD) at 76 Torr it has also been possible to grow roughly 10 ML of *h*-BN on a previously BN-covered Ni(100) surface.

On the **Ni(755)** surface the exposure to 100 L of borazine at 750 K induces a faceting of the substrate [94]. The surface covered by 1 ML of *h*-BN consists of the (111) face and a higher-Miller-index face oriented 45° from the (111). HREEL spectra show two peaks at 90 and 97 meV that are assigned to optical phonons with out-of-plane displacement of the film adsorbed on the two faces. If the sample is heated to 1020 K, the peak at 97 meV disappears and the other gets sharper suggesting that only the *h*-BN on the (111) face remains on the surface because of its interfacial bonding. A similar behavior has been found for the formation of a *h*-BN layer on **Ni(223)**, were adsorption on (111) faces and (114) or (115) has been observed by LEED and ARUPS [95].

3.2.1 *h*-BN on Ni(110)

STM images of 1 ML *h*-BN on Ni(110) show a variety of *h*-BN superstructures, recognizable as Moiré patterns on the surface [96]. This polymorphism is also reflected in LEED patterns where among the most evident structures are a (1 × 6), a (7 × 5) and a (6 × 3). In the first one, the *h*-BN/Ni(110) lattice mismatch along the $[1\bar{1}0]$ direction is compressive by +2.6%, for the second one it is tensile by -0.6%. For the last one no consistent overlayer model is found, therefore the focus is on the first two.

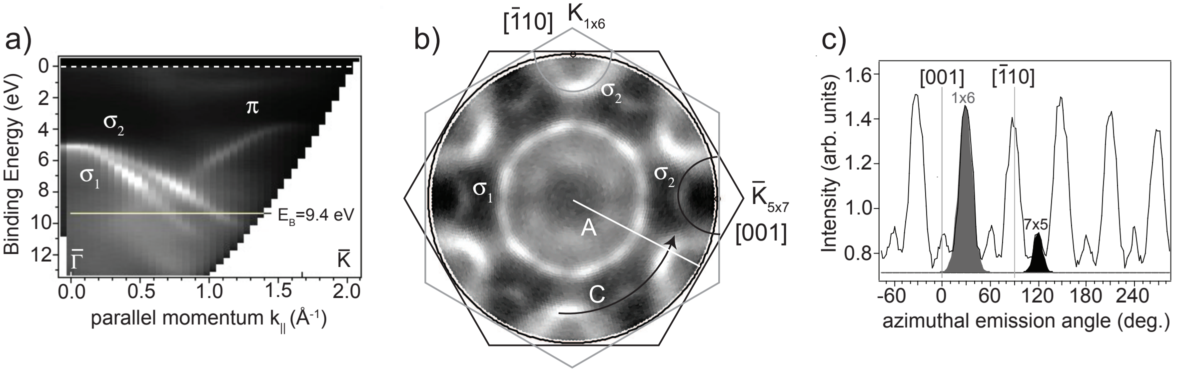

Figure 12: *Angular resolved He Iα photoelectron spectroscopy data for h-BN/Ni(110). White is high intensity. (a) Dispersion plot along the azimuth labeled A in (b) which corresponds to a* $\overline{\Gamma K}$ *direction. The cut in (a) corresponds to the energy (*E_B*=9.4 eV) at which the map in (b) has been measured. (b) k-space map in* $k_{||}$ *projection. Two h-BN matching Brillouin zone labeled (1×6) and (5×7) are marked. The polar cut A shown in (a) and the azimuthal cut C shown in (c) are shown as well. (c) Azimuthal cut across the* σ_2 *resonances at polar angle* θ*=47°. The shaded Gaussians are a weight for the two different h-BN orientations.*

The (1 × 6) unit cell extends for one substrate lattice unit along the close packed $[1\bar{1}0]$ rows and six units in the [001]. The (7 × 5) covers seven units in the $[1\bar{1}0]$ and five in the [001]. ARUPS experiments allow to identify which is the most favorable of the two for *h*-BN growth. The *h*-BN overlayers in the two supercells have two different azimuthal orientations. Accordingly, the *h*-BN $\overline{\Gamma \mathrm{K}}$ direction in the first surface Brillouin zone for the (1 × 6) is 90° rotated with respect to the $\overline{\Gamma \mathrm{K}}$ direction of the (7 × 5). The first is parallel to the $[1\bar{1}0]$, the second to the [001] direction. Fig. 12(a) shows a dispersion plot along a $\overline{\Gamma\mathrm{K}}_{1\times6}$ azimuth. Two σ bands (σ_1 and σ_2) and one π band are visible as in the case of *h*-BN/Ni(111) [88]. In Fig. 12(b) an energy map measured at 9.4 eV shows a cut through the dispersion for the two domains. Clearly the σ_2 resonances are stronger for the (1×6) domain. From the azimuthal cut at 47° polar angle in Fig. 12(c) an area ratio is derived between the $\overline{\Gamma\mathrm{K}}_{1\times6}$ and the $\overline{\Gamma\mathrm{K}}_{7\times5}$ of 6.3:1, which can be explained by the coincidence density ratio Ni/N of $\mathrm{n}_{1\times6}$:$\mathrm{n}_{7\times5}$=1/10:1/56.

4 The Nanomesh

This thesis represents the first study of *h*-BN layers on Rh(111). This system is characterized by a large tensile lattice mismatch (−6.8% Table (1)), which together with the particular bonding properties of the B and N atoms to the substrate are the major responsible factors for the peculiar behavior of the BN film covering this metal surface. The lattice mismatch (M) here considered follows the definition of Zangwill [97] (pag. 268), where M measures how much an adsorbate in-plane lattice parameter deviates with respect to the layer on top of which it grows:

$$M = \frac{a_f - a_s}{a_s} \tag{23}$$

where a_f is the in-plane lattice constant of the overlayer and a_s is the in-plane lattice constant of the substrate.

	Ni	Cu	Rh	Ru	Ir	Pd	Pt	Au	Ag
a_b	3.52	3.61	3.80		3.84	3.89	3.92	4.08	4.09
a_s	2.489	2.553	2.687	2.700	2.715	2.751	2.772	2.885	2.892
M	+0.6%	-1.92%	-6.81%	-7.26%	-7.77%	-8.98%	-9.67%	-13.21%	-13.42%

Table 1: *The values (in Å) of the bulk-lattice constants (a_b) of some fcc and hcp (Ru) metals are taken from [98]. From these values the in-plane lattice constants (a_s) for the hexagonal (111) surface for fcc metals and (0001) for the Ru hcp are calculated, and possible relaxations of the surface atomic lattice are not considered. The lattice mismatches for the different systems are estimated taking the value of 2.504 Å for h-BN [99].*

4.1 *h*-BN film preparation on Rh(111)

For the experiments presented here, two Rh(111) single crystals have been used, and for the LT-STM experiments also a 80 nm thick Rh(111) film grown on Al_2O_3(0001). The crystals were cleaned by repeated cycles of Ar^+ ion sputtering (15 to 20 min) with acceleration voltage of 800 eV and a sputtering current $\sim$ 1.7 to 2 μA/ cm^2, followed by $\sim$ 40 L (1 L=1 Langmuir = 10^{-6} torr·s) of oxygen (O_2) exposure at $700-750$ K and subsequent annealing to 1000 K. The sample cleanliness was checked by LEED and XPS. A clean Rh(111) LEED pattern showed a clear threefold-hexagonal (1×1) pattern with sharp spots, while from the analysis of C 1s and O 1s XPS spectra measured with Al Kα radiation we find that a cleaned sample contained less than 1% of a monolayer of the two species. The value of the workfunction of $\Phi = 5.50 \pm 0.10$ eV measured on the clean

Rh(111) surface agrees with the literature value of 5.4 eV [100]. The workfunction has been determined from the position of the secondary electron cutoff detected by applying a bias voltage (∼-10 V) to the sample and is calculated as $\Phi = h\nu - (E_F - E_{cutoff})$ (with $h\nu = 21.22$ eV for He Iα radiation and $h\nu = 40.8$ eV for He IIα). Pristine Rh(111) films on $Al_2O_3(0001)$ were annealed in UHV for several hours until the temperature of 1050 K was reached. Then they were treated with two (or three) cycles of short Ar^+ sputtering (3 to 10 min at an ion energy of 500 eV and Ar^+ current density of $\sim 1.8\,\mu A/cm^2$), exposure to 2 L of O_2 at 750 K with subsequent annealing to 1050 K. The *h*-BN layers prepared in our laboratory, are grown with CVD of $(HBNH)_3$. Before each sample preparation the borazine was cleaned by one cycle of 'liquid nitrogen freezing and pumping' and it was exposed only when it reached RT (i.e. only in the liquid state). In a typical *h*-BN/Rh(111) preparation the Rh(111) sample was sputtered, oxidized and annealed three times and in the last cycle only 1 L of O_2 was used. Then at the annealing temperature of 1050 K the sample was exposed to about 40 L of $(HBNH)_3$ (i.e. $3 \cdot 10^{-7}$ mbar for 3 min) followed by 1 min of post-annealing at the same temperature.

4.2 BN-superlattice on Rh(111) in LEED patterns

Low energy electron diffraction (LEED) patterns of *h*-BN on Rh(111), as in Fig. 13, show an ordered hexagonal superlattice with spots that surround the Rh principal ones. These superlattice spots can be observed and clearly distinguished in a LEED-beam energy range from 2 to 240 eV. The spots neighboring those of the rhodium, that appear at a larger reciprocal space distance than the substrate positions (indicated as *h*-BN in Fig. 13), belong to an ordered hexagonal atomic overlayer with a real space distance

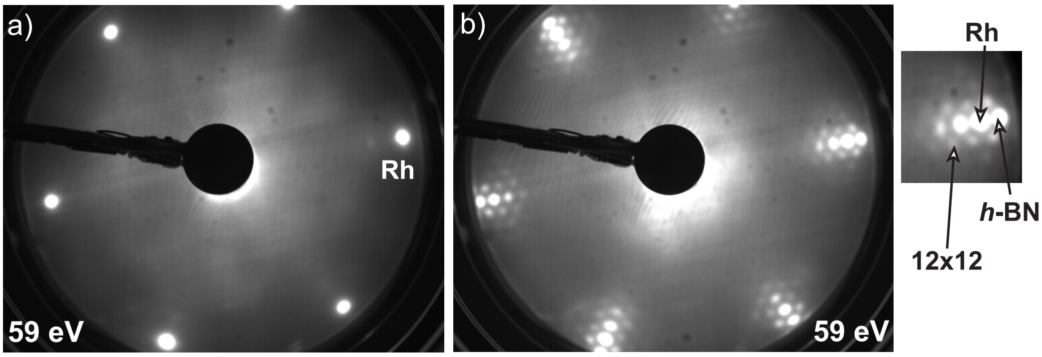

Figure 13: *LEED images of the clean Rh(111) surface (a) and the h-BN on Rh(111) pattern recorded at 59 eV. The detail on the right illustrates the assignment of adjacent group of spots: the Rh(111) substrate spots, the h-BN principal spots and the BN-superlattice spots as indicated.*

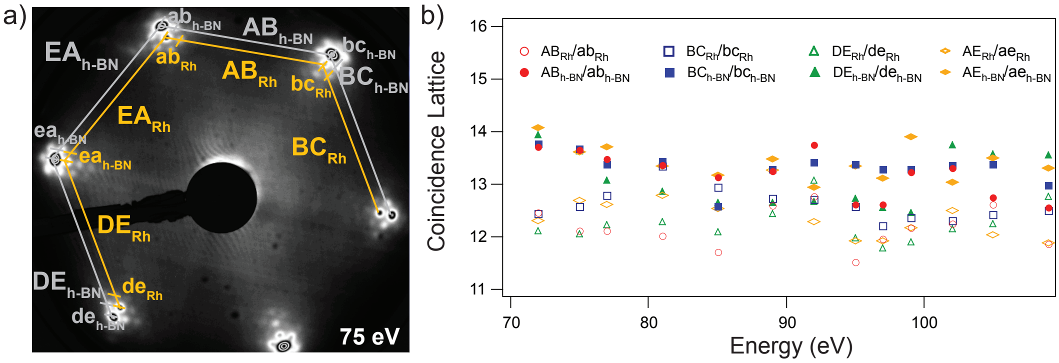

Figure 14: *(a) LEED image of h-BN on Rh(111) recorded at 75 eV. The Rh principal lattice spots (1,1), (0,1), (-1,-1), (0,-1) and (-1,-1) are indicated with the letters A, B, C, D and E respectively. The BN-superlattice given in Rh unit cells results from the ratio of the distances between the Rh principal lattice spots (AB_{Rh}, BC_{Rh}, DE_{Rh}, EA_{Rh}) and the superlattice splitting (ab_{Rh}, bc_{Rh}, de_{Rh}, ea_{Rh}) in the same line profile. The BN-superlattice given in h-BN unit cells is found in the same way and the distances are labeled with h-BN instead of Rh. The distances between the LEED spots are estimated from the peak positions that appear in the line profiles passing between them. These are obtained by fitting the peaks with multiple gaussians, typically 6, with the same width. The coincidence lattice periodicity for each LEED spot distance at different energies for one series of images recorded in the same day on the same structure is plotted in (b). The resulting value is estimated from all the points appearing in this graph.*

smaller than the Rh nearest neighbor distance in the (111) surface. They are assigned to *h*-BN units and their lattice constant, deduced from the Rh value of 2.687 Å (Table (1)), is 2.48 ± 0.05 Å. The periodicity of the BN-superlattice (given in numbers of Rh or *h*-BN unit cells) results from the analysis of series of LEED images recorded at different beam energies (between 70 and 110 eV, where only first order Rh spots appear and all the spots are inside the LEED screen). For each image the ratio between the Rh-principal lattice spot distances ((1,1) and (0,1), (-1,-1) and (0,-1), (0,-1) and (1,-1), (1,-1) and (1,1)) and the superlattice spot splitting and also the ratio for the *h*-BN-spots in the corresponding direction Fig. 14, have been evaluated. The position of LEED spots appearing in a line profile that crosses two principal spots has been estimated by fitting their intensities with multiple Gaussians with the same peak width. The distance between the LEED spots is thus the center of these Gaussians. The resulting average value for the hexagonal BN-superlattice is $(12.4 \times 12.4) \pm 0.4$ Rh units and $(13.3 \times 13.3) \pm 0.4$ *h*-BN units, which corresponds in the real space to $(3.3 \times 3.3) \pm 0.1$ nm. This LEED pattern is consistent with the formation of a coincidence lattice or a Moiré pattern. In order to better visualize the BN-superlattice in the LEED images, a simple model of a

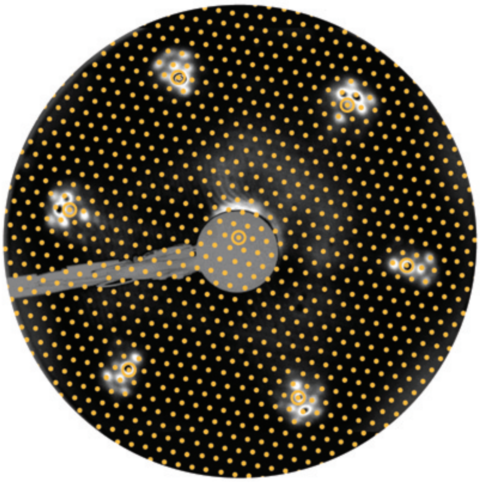

Figure 15: *Simulation of the LEED pattern recorded at 89 eV. Not all the BN-superlattice spots can be seen in the experimental pattern due to the scattering events in the LEED process. In order to estimate the incoming electron beam wave number, the beam energy has been corrected with the sample work function (4.15 eV) and the sample surface has been tilted with respect to the direction of the LEED gun. In particular a clockwise rotation of 0.27° along the x-axis on the sample surface (looking from right side along the x-axis) and a counter-clockwise rotation of 0.54° along the y-axis are needed. The sample is correctly in the focus of the beam. The simulated LEED pattern is projected on our spherical LEED screen of radius of 52 mm and sample-screen distance of 54 mm.*

(12 × 12) Rh reciprocal lattice in Fig. 15 is overlayed on a picture recorded at 89 eV. In this case for reproducing the experimental pattern the sample work function (4.15 eV) is considered and the best agreement is obtained with a tilt of the sample surface with respect to the incoming electron beam. Surface X-ray diffraction (SXRD) experiments performed at the Swiss Light Source (SLS) on the *h*-BN/Rh(111) structure confirmed unambiguosly that the BN-superlattice is a commensurate structure with a (12 × 12) Rh unit cell [101]. This information results from in-plane scans along high symmetry directions of the Rh substrate, where the (13/12, 0) peak of the superlattice can be clearly distinguished Fig. 16.

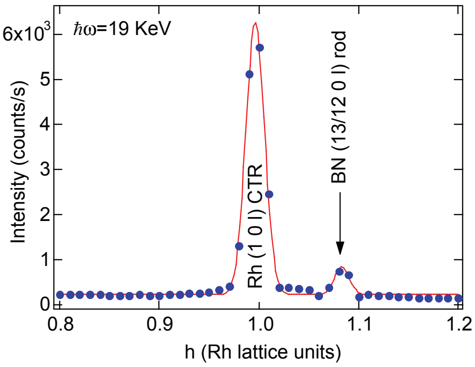

Figure 16: *A SXRD profile recorded along a (h k l) direction where h is scanned between 0.8 and 1.2 Rh lattice units, k=0 and l=0.07 Rh lattice units, where the crystal truncation rod of the rhodium substrate is weak [101]. The (1 0 0.07) peak of the Rh and the (13/12 0 0.07) peak of the BN-superlattice are clearly visible, confirming a periodicity of (12 × 12) Rh unit cells on the surface. The SXRD data were measured with X-ray photon energy of 19 keV and at a glancing angle of incidence of 0.2°.*

4.3 The nanomesh imaged by STM

The real space nature of the BN-superlattice on Rh(111) appearing in LEED patterns is revealed by STM. A highly regular hexagonal structure with a periodicity of $3.2 \pm 0.1\,\mathrm{nm}$ that covers homogeneously the entire Rh(111) surface is imaged by STM (Fig. 17). The structure appears as a '**nanomesh**' formed by two distinct areas: the brighter regions, higher in topography, form the wires of this network, while the round darker regions resemble holes. Cross-sectional line profiles along several unit cells of this structure show a corrugation of $0.7 \pm 0.2\,\mathrm{nm}$, depending on the tunneling parameters used during scanning. The wire size has a typical value of $1.2 \pm 0.2\,\mathrm{nm}$, while the holes are $2.0 \pm 0.2\,\mathrm{nm}$ wide.

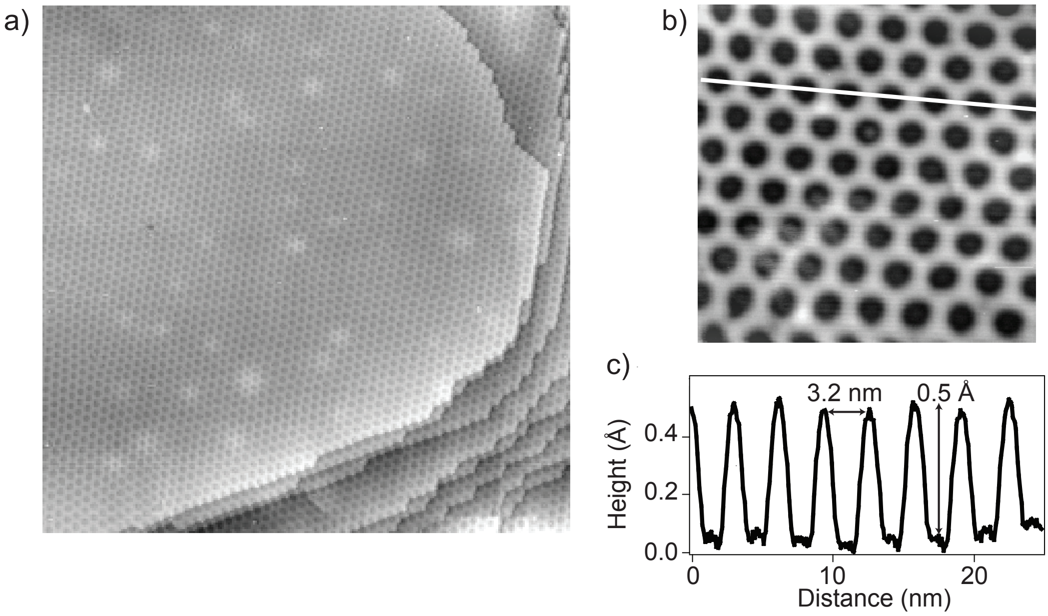

Figure 17: *Constant current STM images of h-BN on Rh(111): (a) large area topography scan recorder at RT of the hexagonal BN superstructure covering a large terrace and the surrounding narrower ones (150×150 nm^2, I_t=0.5 nA, V_s=-2 V); (b) smaller area of the same structure measured at 77 K (25×25 nm^2, I_t=0.01 nA, V_s=-1 V). This honeycombed nanostructure with 3.2±0.1 nm periodicity is called 'nanomesh' since it consists of two distinct areas clearly seen in (c), the cross-sectional profile along the white line in (b). The brighter (higher) areas correspond to the mesh wires 1.2±0.2 nm broad, while the darker depressions are the mesh holes with size of 2.0±0.2 nm. The mesh corrugation measured at this low current is 0.5 Å. In these profiles a protruding part within the hole is always present with a corrugation of 0.1 Å. The brighter spots appearing in (a) are 'argon bubbles', subsurface Ar$^+$ ions introduced by the sputtering procedure in the sample preparation [102].*

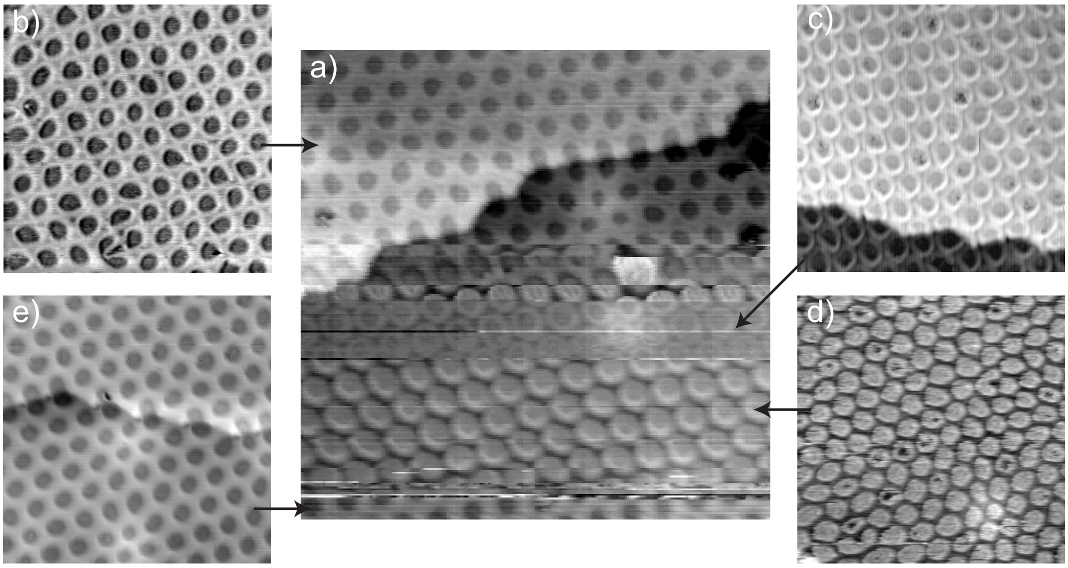

Figure 18: *Constant current STM images of h-BN on Rh(111) measured at RT at negative voltages showing the different contrast achievable for the nanomesh. (a) In a single image (40×40 nm^2, I_t=1.8 nA, V_s=-2 V) four (at least) different contrasts show up. Some of them are reproduced for other nanomesh preparations respectively in the images (b-e) as indicated by the arrows. (b) The nanomesh can appear as a hexagonal network due to the darker contrast seen in the mesh wires, the corrugation within the wires is 0.15 Å and wire-hole is 0.75±0.10 Å (25×25 nm^2, I_t=1 nA, V_s=-2 V); in (c) the wires around the holes have the appearance of 'doughnuts', the corrugation within the wires is 0.25±0.10 Å and from wire to hole is 0.6±0.1 Å (30×30 nm^2, I_t=1 nA, V_s=-2 V); (d) the mesh holes instead of appearing as holes, are imaged as protrusions of corrugation 0.8±0.1 Å (30×30 nm^2, I_t=1 nA, V_s=-1 V); (e) typical contrast of the nanomesh. The wire to hole height difference for this image (30×30 nm^2), measured at I_t=2.5 nA and V_s=-1 V, is 0.9±0.1 Å.*

The bright spots in Fig. 17(a), randomly distributed on the surface and with different sizes (from 3 to 10 nm), are 'argon bubbles', induced by the sputtering procedure [102]. Ar$^+$ ions fill large and stable subsurface cavities creating enough pressure to bend upwards the top Rh layer. The nanomesh gets locally strained in these areas and the holes are small on top of the bubbles and larger on the sides. From previous studies on the Ru(0001) surface, only an annealing at temperatures above 1300 K leads to the Ar$^+$ dissolution into the bulk and disappearance of the bubbles [102]. With an annealing up to 1050 K they are still visible on the Rh(111), therefore also on this surface higher temperatures are needed. Typical values used for imaging the mesh are tunneling currents of 1 nA and a sample bias of -1 V (i.e. electron tunneling from the tip states to the unoccupied sample states); the corrugation is then ~ 0.7 nm. It is observed that the

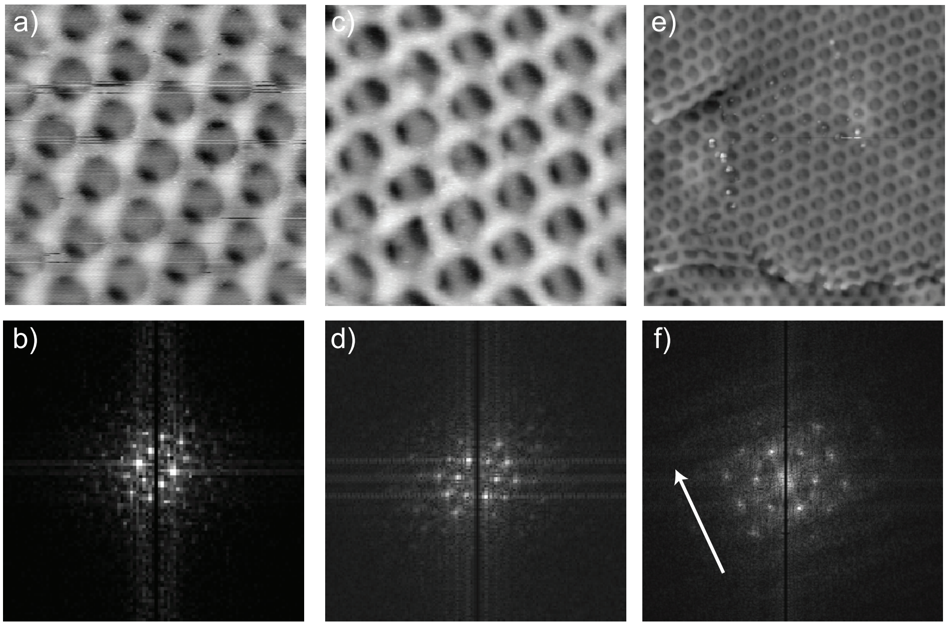

Figure 19: *Constant current STM images of the nanomesh on Rh(111) measured at RT (a)(15×15 nm^2, I_t=1 nA, V_s=-2 V) and at 77 K (c, e) (c: 17×17 nm^2, I_t=0.1 nA, V_s=-1 V; e: 50×50 nm^2, I_t=0.1 nA, V_s=-1 V). (c) has been recorded just after (e). (b, d, f) Fourier-transform images of (a-e) respectively (b: 6.47×6.47 nm^{-2}; d: 5.4×5.4 nm^{-2}; f: 3.5×3.5 nm^{-2}). The topographic images (a) and (c) give the impression that the nanomesh is formed by two hexagonal mesh layers shifted one with respect to the other but this is due to a double tip effect not clearly visible in the Fourier-transform images (b) and (d). The repetition of the 'higher' features as step edges and adsorbates on the surface appearing in (e) gives evidence for the presence of a tip with a double termination scanning over the surface. This effect is visible in (f) as a stripe across the (0,0) elongated in the same direction of the double tip, indicated by the arrow.*

contrast is often inverted at positive voltages and the nanomesh holes (or depressions) appear as protrusions. However, even at negative bias voltages the same effect can be observed (Fig. 18(d)). Depending on the state of the tip different resolution and contrast on the nanomesh can be obtained: the holes can appear as depressions (Fig. 18(e)) or as protrusions (the round islands in Fig. 18(d)), the nanomesh can be imaged as a hexagonal network (Fig. 18(b)) or only the rims surrounding the holes are sometimes imaged (the 'doughnut-like' appearance in Fig. 18(c)). All these effects can be obtained at the same bias voltage (Fig. 18(a)). The reason for these changes in contrast is still unclear but they could be due to the presence of contaminants on the surface interacting with the tip, or due to the state of the tip apex, i.e. a pure W-tip or a B or N-terminated tip. The first model for the structure of the nanomesh consisted of two *h*-BN layers with real holes (due to missing BN untis) of 2 nm size growing one on top of each other and shifted in such a way as to cover most of the Rh substrate [18]. This model was partially based on STM images, as Fig. 19(a), were the two layers are clearly visible, but mainly on ARUPS and XPS data and decoration experiments with C_{60} molecules that will be discussed in the next paragraphs. Typical STM images of the nanomesh (as Fig. 17 or Fig. 18(e)) do not show this double layer network. Images as Fig. 19(a) have been rarely reproduced (examples are Fig. 19(c) and (e)) and the difficulty in obtaining such contrast is explained by the fact that it is due to a tip artifact known as 'double tip' as realized later on. A 'double-tip' with two atomic terminations at different heights scanning over the surface creates an image which is a superposition of the profiles due to the two tip atomic-apexes. Therefore in Fig. 19(a) a nanomesh layer was imaged twice with a height difference corresponding to the vertical distance of $\sim 0.7\,\text{Å}$ between the two tips. Such an effect can be easily identified when the double-tip images features on the surface which are at least as high as the tip apex distance (as steps, dislocations, defects or contaminants), as can be seen in Fig. 19(e). These effects were not visible and recognizable in the images of the steps measured before or after Fig. 19(a), and the double tip is not visible in the Fourier-Transform (FFT) image Fig. 19(b) of Fig. 19(a) where a blurred intense area in the direction of the double tip would be a feature of tip artifacts as visible in Fig. 19(f).

The current model of the nanomesh has been partially revealed by low temperature (77 K) STM measurements which give the possibility to image the nanomesh in atomic detail.

4.3.1 The nanomesh: a corrugated monolayer

Atomic resolution of the nanomesh in STM images is achievable at bias voltages close to the Fermi level. While at RT high tunneling currents (I_t at least 3 nA) are usually needed to induce the appearance of atomic rows in the images, at LT the atoms can be imaged at low current values (I_t around 0.1 nA) making the data more reliable since the possibility of modifying the surface by the tip is highly reduced. In Fig. 20 the same nanomesh area has been imaged at $\mathrm{I_t} = 0.1\,\mathrm{nA}$ varying the sample bias voltage. The atoms in the holes and in the wires can be distinguished and no double-layer *h*-BN nanostructure is visible. The nanomesh appears as single compact corrugated sheet covering the entire Rh surface. Only one atomic species is imaged within the BN-layer and it is likely that it is the N. In fact for *h*-BN on Ni(111) it is found that the N atoms have the highest LDOS at the Fermi level, thus they are imaged as brighter protrusions in atomically resolved STM images [88]. At small bias voltages, imaging states near the Fermi level with $\pm 2\,\mathrm{mV} < V_s < \pm 10\,\mathrm{mV}$ (Fig. 20(c) and (f)), the atoms in the holes are highly resolved,

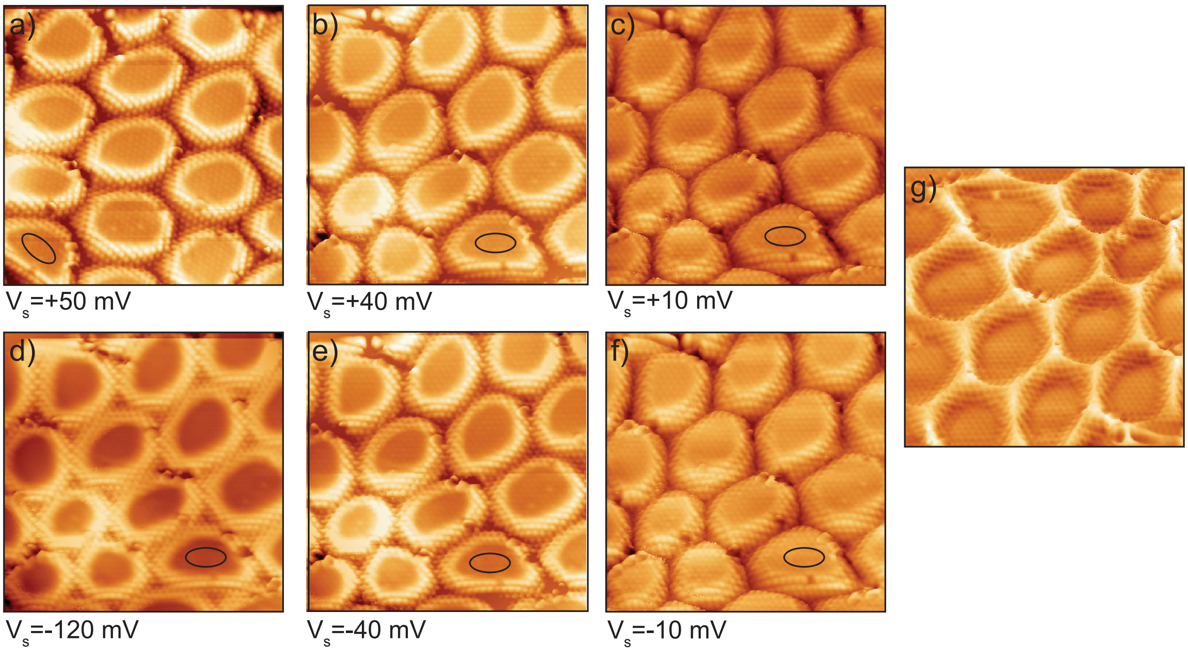

Figure 20: *High resolution series of constant current STM images of the same area of the nanomesh measured at 77 K. The scanned area is 10×10 nm^2, the tunneling current I_t=0.1 nA and the sample voltage is varied between +50 mV and -120 mV. The atomic structure of the nanomesh is well resolved: in the holes at sample bias voltage close to the Fermi level and on the wires at negative values around 120 mV. The rims of the holes are the brighter parts of the nanomesh imaged by STM. No real holes are present but a compact layer. Only one atomic species is imaged and it is likely that it is the N. In (a) the scanner is rotated 40° counterclockwise with respect to the other images as indicated by the black ellipse which identifies the same unit cell in all the pictures. (g) is the same image as (e) but with reversed contrast and rotated of 180°. The nanomesh units are not so regular due to the presence of an Ar^+ bubble as seen in the brighter-smaller nanomesh hole.*

while the wires appear as dark regions. For positive or negative values of V_s, with $10\,\text{mV} < V_s < 50\,\text{mV}$, the atoms on the rims surrounding the nanomesh holes are those that give the highest contrast in the images (Figs. 20(a-b) and (e)). At negative voltages $50\,\text{mV} < V_s < 150\,\text{mV}$ not only those on the rims but also the atoms in the wires become visible (Fig. 20(d)). The atoms in the rims do not line up in straight fashion but follow curved lines. If the scanner is rotated with respect to the surface, this wavy like atomic arrangement is also imaged rotated. This suggests that it is a feature belonging to the mesh structure and not an artifact due to the scanning (otherwise it is expected to appear always on the same position in the image). The fact that the curvature of these lines is convex (not following a circle concentric with the mesh pore) is still not understood. This imaging of the atomic rows might be due to an elastic response of the *h*-BN film to the

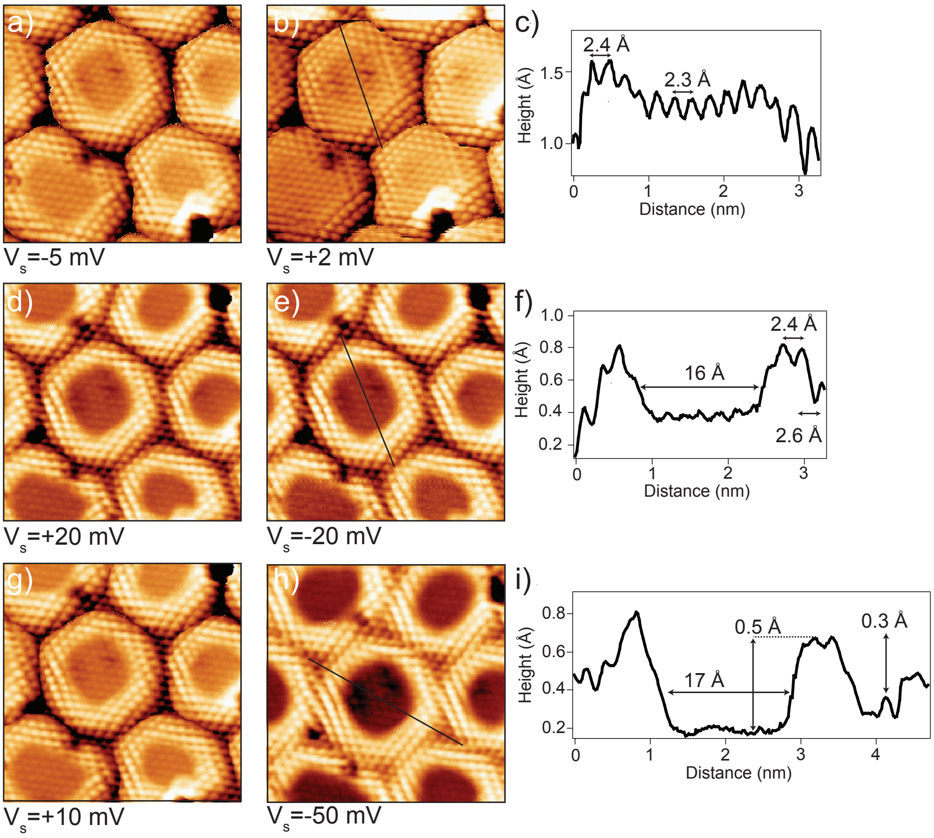

Figure 21: *High resolution series of constant current STM images of a nanomesh unit cell (6×6 nm^2, I_t=0.1 nA). The sample voltage is varied between +20 mV and -50 mV as indicated below each figure. In (c) the cross-sectional profile corresponding to the black line in (b) is plotted, in (f) the one from (g) and in (i) the one of (h). The distances delimited by the arrows are given in the captions.*

STM tip. The interaction between the two may result in the pulling out of the surface the atoms that sit in the transition areas from holes to wires, stretching their distances. These kinds of interactions between a scanning probe tip and an insulating material have been observed in scanning force microscopy studies [103]. In Fig. 21 another series of STM images taken at voltages around E_f on a single nanomesh unit cell can be seen and useful information can be gained by cross-sectional profiles along atomic lines. The distances between nearest neighbor atoms appear slightly different within the unit cell: they vary from 2.3 Å in the holes, to 2.4 Å in the rims, to 2.6 Å in the wires. These values need to be corrected for the tip shape, and for the inhomogeneity of the tip imaging of the holes and the wire during scanning (this can create the asymmetry seen in the profiles) and for electronic effects due to the imaging of the LDOS and not the true topography of the surface. Nevertheless these values are close to the in-plane N-N (B-B) distance in the *h*-BN of 2.5 Å. Depending on the bias voltage, the rims appear more or less

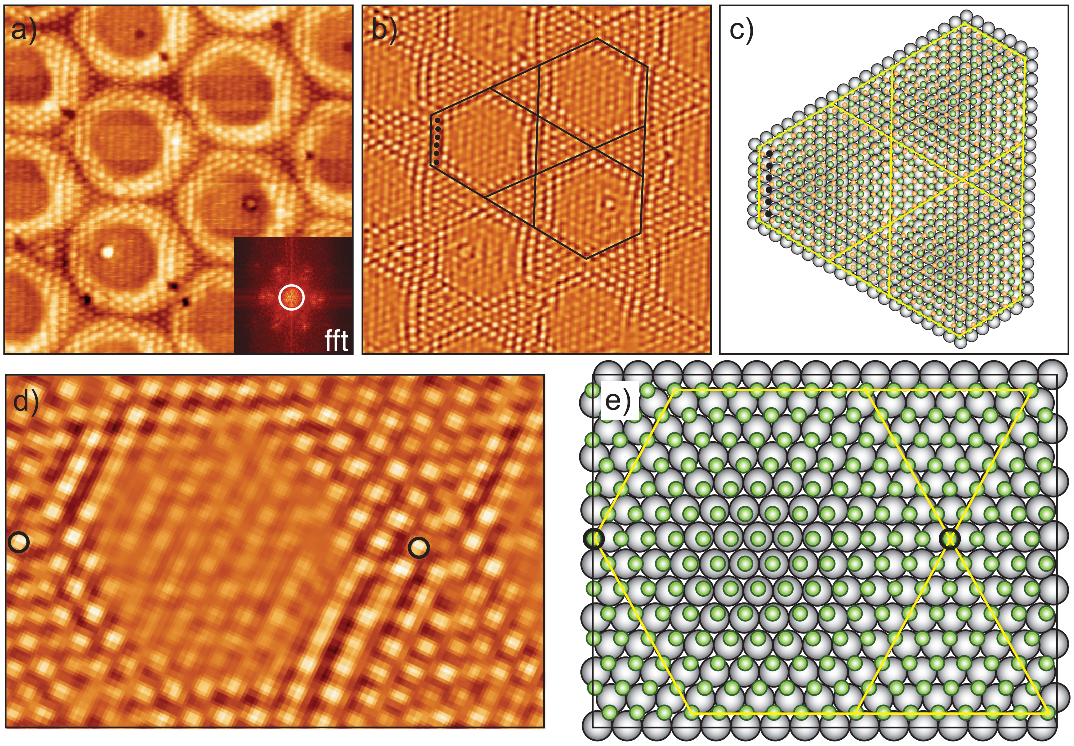

Figure 22: *The atomic structure of the nanomesh can be reconstructed from the constant current STM image (a) (9.4×9.4 nm^2, I_t=1 nA, V_s=-2 mV). In (b), image (a) has been filtered in order to remove the 3.2 nm periodicity of the nanomesh and obtain a picture of the atoms present in the wires and holes (i.e. the spots inside the white circle drawn around the (0,0) in the FFT image of (a) shown in the inset have been removed). (c) Atomistic reconstruction of the area delimited by the black lines in (b). The six black spots are in corresponding positions in the two images. The atomistic model schematically reproduces the (b) in the surface plane but the corrugation out of plane is not considered. Green atoms are N, the orange B and the gray Rh but in the STM images only the N atoms appear; this assignment is based on the atomistic model form [104]. Figures (d) and (e) zoom into (b) and (c) in order to better visualize and count the atoms in the nanomesh unit cell.*

broad and the nanomesh holes have a diameter around 1.7 nm, smaller than the 2.0 nm usually seen at integer values of the voltage. In the topography image Fig. 22(a), the nanomesh unit cells are more regular than in Fig. 20, therefore the atomic structure can be reconstructed more easily. Applying a filtering to Fig. 22(a) in such a way as to remove the 3.2 nm nanomesh periodicity, then only the atomic structure is left on the picture in Fig. 22(b). Instead of round nanomesh holes, now asymmetric hexagons appear and they are surrounded by triangular areas that form the mesh wires and the rims. With a close look to the structure the final nanomesh model is schematically plotted in Fig. 22(c) and in detail in Fig. 22(e). The nanomesh in Figs. 22(c-e) can be viewed as formed by hexagons whose sides are constituted by 7 or 8 N atoms which alternate from side to side. Each hexagon is surrounded by six equilateral triangular areas with sizes defined by the side of the hexagon at the boundary. Each pair of neighboring triangles joins at an atom which identifies the centre of the nanomesh wire in the direction orthogonal to the one connecting the centers of two hexagons. In this way the (13×13) N-N (or B-B) periodicity is retained, since it corresponds to the sum of 6 and 7 N-N (B-B) interatomic distances which constitute the sum of the sides of the triangles. The centers of the hexagons are determined by three N atoms. Since 169 atoms are found in the unit cell (as shown schematically in Fig. 22(e) and Fig. 23) finally it can be concluded that the atomic species seen are N (or B) and not Rh.

DFT calculations on *h*-BN on Ni(111) [88] and on Rh(111) [104] have shown that the N strongly favors bonding directly on top of the transition metal atoms (and B on *fcc* or *hcp* sites), while the other positions are less or not stable. In view of this information the model can step beyond a mere characterization with respect to the N atoms arrangement, but the entire unit cell can be reconstructed (Fig. 22(c) and Fig. 23). The holes seen in the STM images are mainly due to the area where N atoms occupy nearly on top positions, and the diameter of the hole of $\sim 2\,\text{nm}$ is due to the distance between 9 N atoms. Three N atoms in the hole center sit on top of Rh atoms (colored in blue in Fig. 23). The atom in the middle of the wire, where two triangles touch each other, corresponds to a N sitting on a bridge site. This atom plus four more form the mesh wire of $\sim 1.2\,\text{nm}$ size. The wires are made up of two kinds of triangular regions with 7 or 8 atoms in their sides and with different stacking of the BN units: the smaller areas are characterized by B atoms adsorbed on top sites and N in hollow sites, while in the bigger triangles no N nor B occupy on top sites and they sit in *fcc* or *hcp* ones. *Laskowski et al.* simulated the nanomesh unit cell with an ab initio force-field approach, and the experimental data agree well with their theoretical model [104]. In the model the holes are the areas where the BN layer sits closer to the Rh since the highest bonding for the BN to the substrate is due to the N atoms occupying on top sites and B *fcc* sites. Therefore in the holes the BN units ‘lock-in’ to the substrate. The further the BN units are from the centers of the holes, the higher is the strain to which they are subjected since they are forced to occupy unfavorable adsorption positions. Due to the weaker bonding to the substrate at these places, these atoms are pushed upwards forming the nanomesh wires (as visible in Fig. 20(g)). The nanomesh is thus a single layer whose corrugation is driven by the Rh-lattice site occupation of the BN, by the bonding between the BN and the substrate and by the in-plane BN-cohesive forces.

Examples of other nano-patterned surfaces are misfit dislocation networks and strain-relief patterns, which have been observed in the epitaxial growth of metals on metals with

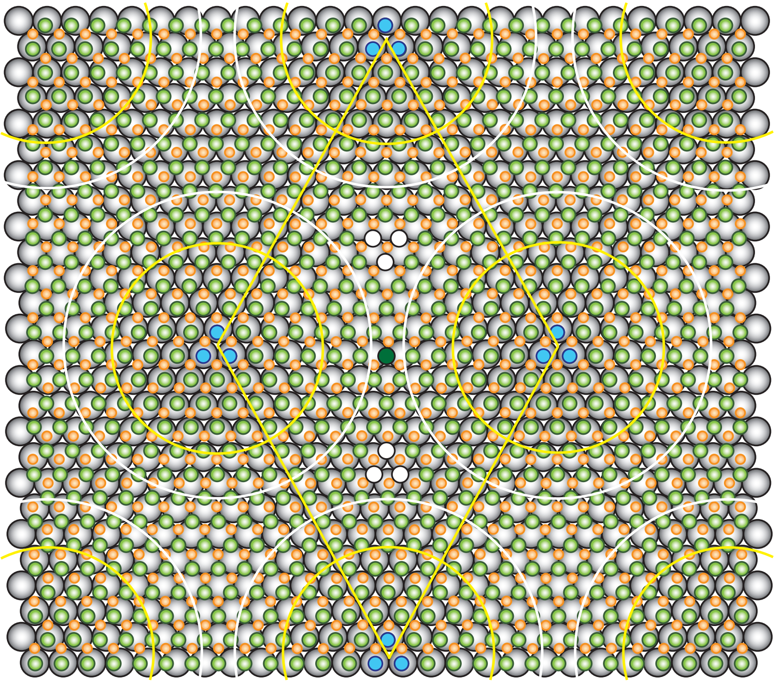

Figure 23: *Model of the atomic structure of the nanomesh. According to the assignment of the species from [104], the grey atoms are Rh, orange B and green N. The nanomesh unit cell side is long 13 N-N atoms distances. The unit cell is drawn from the centers of the nanomesh holes (yellow circles) each of them defined by 3 blue N atoms. In the holes the N atoms reside in nearly-on top sites. The hole diameter is 2 nm, due to 8 N-N atom distances (∼2.5Å). The darker green N atom sits on a bridge site, in the center of the wire. The wires have a width of 1.2 nm, which corresponds to 5 N-N distances. White circles represent the 'rims' of the holes but they are seen as wires in STM images measured at higher bias voltages. The rims have a thickness defined by ∼3 N atoms and the holes appear with a diameter of 1.6-1.7 nm. In the wires either the B occupy on top sites or neither N nor B sit on top the Rh atoms. The six white atoms in the wire are often imaged as depressions even if they should be among the brightest since topographycally the highest. Strong electronic effects need to be taken in account.*

small lattice mismatch [105–107] and in reconstructed close-packed metal surfaces (as the Au(111) or Pt(111) [108]). In these systems the major responsible for the outcoming film structure are the relative strength of the substrate potential acting on the adsorbed atoms and the adatoms lateral interaction potential [109]. When both the potentials have comparable strengths the resulting system is a strain relief pattern, consisting of areas where the strain due to the lattice mismatch is locally relieved and areas where it increases. The notion of misfit dislocation network is used if the overlayer has the possibility to grow locally pseudomorphic. For insulating materials the formation of hexagonal superstructures besides those generated by Moiré effects has been shown for the Al_2O_3 film grown on $Ni_3Al(111)$ [110].

Strong electronic effects are present in these STM images and the most evident one is the imaging of the inner part of the wires as trenches, while geometrically these should be the highest areas on the surface. Especially the groups of three atoms in the wires (depicted in white in the model Fig. 23) have an apparent height 0.3 Å lower than the rims (Fig. 21(i)). The same corrugation is observed for the domain walls in the second-monolayer Ag film adsorbed on Pt(111) at 340 K [105]. In that case the domain walls are regions with lower atomic density than the surrounding areas where the Ag atoms are compressed. This causes a lower electron density in the walls which is responsible for an imaging height close to their geometric value, and they appear as depressions. In contrast, the other regions are imaged higher due to their increased electronic density since they are compressed. For the nanomesh this is not the case, this effect might rather be connected to the fact that the tunneling happens between the Rh electron wave functions, modified by the BN layer, and the tip states. The dark areas are the parts less in contact with the Rh, thus farther from the decaying substrate electron wave function in the tunneling barrier. Simulations of these images are needed in order to understand this effect, the sharp contrast given by the rims and the contrast inversion from hole to protrusions when switching from positive to negative voltages during scanning.

In view of this single layer model, many features appearing in the STM images can be explained. For example the reason why the nanomesh holes are smaller on top of the Ar^+ bubbles and larger around them is due to the substrate lattice distortion. For the case of bare Ru(0001), published data [102] show that the atomic lattice is stretched on top of the Ar^+ bubbles while it is laterally compressed around them. Such a strain imposed on the Rh substrate influences the nanomesh because above the island the lattice mismatch is enhanced and therefore less on top Rh atomic sites are found for the N atoms, while on the sides the Rh layer is compressed and therefore the lattice mismatch is reduced and more favorable on top sites are occupied. Dark features sometimes occur on the nanomesh film. Inside these depressions the nanomesh can still be imaged but with different registry and at a different height than the surrounding layer. An example is shown in Fig. 24 for a *h*-BN structure grown on a Rh(111) thin film on $Al_2O_3(0001)$. A triangular island with dark contrast of 7.3 ± 0.1 nm side, appears on a nanomesh film. The portion of the nanomesh inside it, is imaged 0.73 ± 0.05 Å lower than the neighboring units and the holes between upper and lower layer are not in registry. This structure results from a defect in the Rh substrate generated during the film growth which induces different BN sites occupation between the two nanomesh areas. The stacking fault in this case is due to Shockley partial dislocations [111]. Such intrinsic stacking faults are created by shearing one half of the *fcc* crystal across a (111) plane by

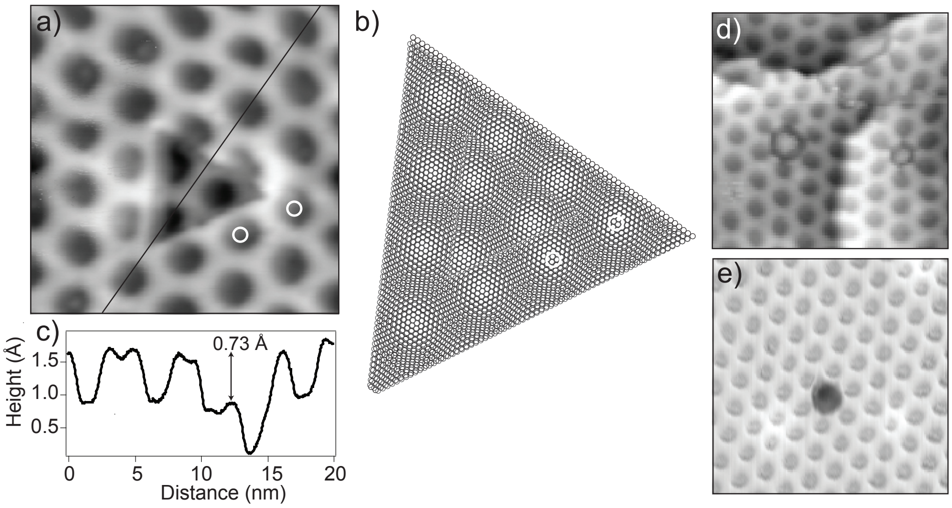

Figure 24: *(a) Constant current STM image measured at 77 K of h-BN grown on a Rh(111) 80 nm thick film on $Al_2O_3(0001)$ (16.6×16.6 nm^2, I_t=0.1 nA, V_s=-0.01 V). The triangular area is represented with an atomic model in (b) where a layer of N atoms is overlayed on a Rh one. The white circles indicate the corresponding mesh holes of (a) and (b). In the model a faulted triangular area is drawn in the Rh layer where the Rh atoms are placed on hcp sites and not on fcc ones. This is responsible for the different registry of the Moiré-like hexagonal pattern created by the N layer. The areas with bright contrast are due to N atoms on top Rh sites and therefore correspond to the mesh holes as in the STM image. (c) Cross sectional profile along the line in (a). In the STM images (d) and (e) another kind of defect on the mesh is visible as missing mesh unit cell (d: 26.5×26.5 nm^2, I_t=0.005 nA, V_s=-1 V; e: 26.5×26.5 nm^2, I_t=2.5 nA, V_s=-1 V). At RT it often appears as a dark hole (d), while at 77 K it is filled by bright features as can be seen in the two defects imaged on two different terraces.*

a Burger vector $b = a_{Rh}/6$ along the direction $[\bar{2}11]$ (or equivalent), generating therefore a stacking sequence of the planes ABCACABC instead of ABCABC. If the shearing is repeated then an extrinsic fault arises. In the Rh bulk film these 3D faults are seen on the surface as triangular islands. The Rh atoms occupy *hcp* sites and the expected height is $3.8/6 = 0.63\,\text{Å}$ lower than the unfaulted-surface layer. Possible relaxations of the atoms on the surface could still lead to differences in this value. This stacking fault in the substrate explains the lower height of the mesh and its shifted registry inside this area. A third kind of defect can be detected on the mesh layer. It appears as dark circles of the size of a nanomesh unit cell which are surrounded by the nanomesh holes, as in Fig. 24(d). At low temperature (77 K) such defects are almost always filled by bright contaminants (probably C atoms) as shown in Fig. 24(e). These are not always seen at RT but they might be mobile on the surface or already desorbed from the surface. Therefore it is possible that they are responsible for the missing nanomesh unit cell.

4.4 The electronic structure of the nanomesh

Normal emission UPS spectra of the clean Rh(111) surface change upon formation of the nanomesh, as shown in Fig. 25. The Rh bands (visible at energies $> 5\,\text{eV}$) get attenuated and the Rh work function shifts to lower values, from $\Phi_{\text{Rh}} = 5.10 \pm 0.10\,\text{eV}$ to $\Phi_{\text{h-BN}} = 4.15 \pm 0.10\,\text{eV}$. The same behavior has been observed for the case of *h*-BN on Ni(111), but there the work function shift ($\Delta\Phi$) is twice as large as for the Rh case ($\Delta\Phi_{\text{Ni}} = 1.8\,\text{eV}$ vs. $\Delta\Phi_{\text{Rh}} = 0.95\,\text{eV}$). This work function change due to the adsorption of a *h*-BN layer on a metal surface, can be explained by the polarization of the *h*-BN layer and by the charge transfer to the substrate, or by charge displacement within the *h*-BN/metal interface that can occur [88]. Besides the work function change, the most prominent features in the UPS spectra due to the presence of the *h*-BN layer on the Rh substrate are the two pairs of the BN-related peaks, each of them split by $\sim 1.1\,\text{eV}$. While in the case of *h*-BN on Ni(111) a single σ and π band are present, on Rh(111) two σ (σ_α, σ_β) and two π (π_α, π_β) bands appear. They are found at the following binding energies: $E_B(\sigma_\alpha) = 4.57 \pm 0.10\,\text{eV}$, $E_B(\sigma_\beta) = 5.70 \pm 0.10\,\text{eV}$, $E_B(\pi_\alpha) = 8.76 \pm 0.08\,\text{eV}$ and $E_B(\pi_\beta) = 9.83 \pm 0.10\,\text{eV}$. This doubling of the bands had never been observed in other single-layer *h*-BN/metal structures and is a peculiar fingerprint of the presence of the nanomesh on a metal surface. ARUPS studies of monolayer graphite (MG) on *h*-BN on Ni(111) show as well the presence of these four peaks and a work function shift of 1 eV with respect to the clean Ni surface [112]. The lower binding energy σ and π bands are assigned to the MG, the hexagonal layer on top of the BN, and its structure resembled the one of an isolated graphite film. The higher binding energy σ and π bands belong to the *h*-BN layer, which is more strongly bonded since it is in close contact with the Ni substrate. The difference of $\sim 1\,\text{eV}$ between the binding energies of the two σ bands agrees well with the splitting on *h*-BN/Rh(111), while the difference for the π is higher $\sim 1.6\,\text{eV}$. Nevertheless, the assignment of the four bands to a double *h*-BN-layer

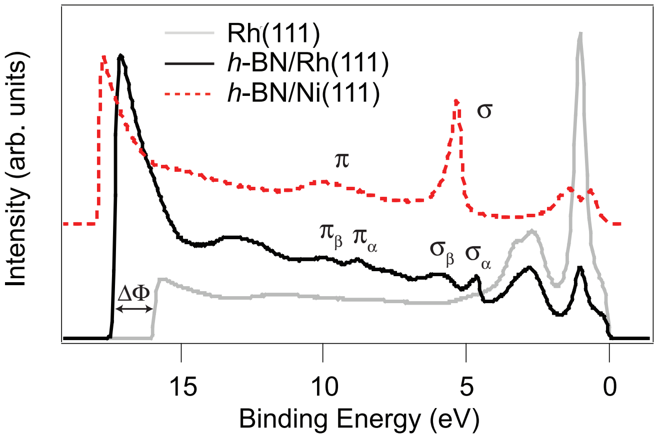

Figure 25: *He Iα normal emission UP spectra for Rh(111), h-BN/Ni(111) and h-BN/Rh(111). Upon h-BN adsorption the Rh(111) work function shifts (by* $\Delta\Phi$*) and two* σ *(*σ_α*,* σ_β*) and two* π *(*π_α*,* π_β*) bands appear, while in the case of h-BN/Ni(111) only one* σ *and one* π *band are present.*

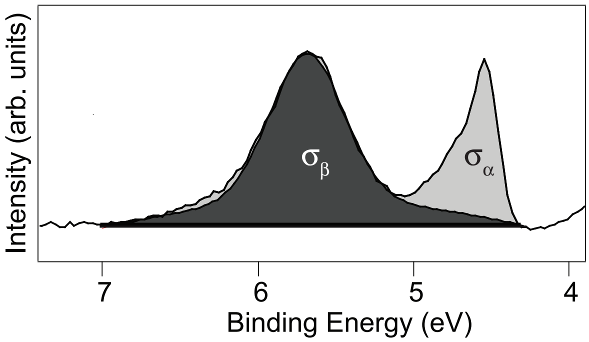

Figure 26: *He Iα normal emission UP spectrum for h-BN/Rh(111) measured at region of the σ bands. The total area is devided in the contributions from the two σ components. The area of σ_β in the spectrum is obtained by integration of the Gaussian fit of the experimental peak, while the area of σ_α is given by the total area minus the one of σ_β since the peak has an asymmetric shape. The area ratio $\sigma_\beta/\sigma_\alpha$= 2.63 ± 0.20 is calculated from the analysis of 17 UPS spectra belonging to different nanomesh preparations.*

structure in the case of *h*-BN/Rh(111), is not the unique way to explain the nanomesh electronic structure [18]. The two pairs of peaks (σ_α and π_α, σ_β and π_β) can be related to the different regions of BN present in the single corrugated nanomesh layer, which exhibit two different chemical bonding to the Rh substrate. The $72 \pm 2\%$ of the total area of the sigma bands in normal emission UPS spectra is due to σ_β, the higher binding energy component, while the remaining $28 \pm 2\%$ is due to σ_α (Fig. 26). Chemical imaging of the nanomesh structure with STM gives the possibility to identify the nature of the two pairs of bands. The conductivity or dI/dV signal is directly proportional to the local density of states of the surface, and spatially resolved spectroscopic information at a particular bias voltage can be obtained by acquiring simultaneously dI/dV maps (i.e. the conductivity at each point on the surface, $dI/dV(x,y)$) and constant current topographic images. The dI/dV signal is produced with a lock-in amplifier which detects the alternating current due to the modulation of the sample bias V ($V = V_0 + \Delta V \sin(2\pi\nu t)$). dI/dV maps have been recorded at a temperature of 77 K simultaneously with constant current topographic images, with an amplitude modulation of $\Delta V = 15\,\text{mV}$ and frequency $\nu = 630\,\text{Hz}$. The LDOS mapped in conductivity maps measured at the bias voltage corresponding to the binding energy of σ_β ($V(\sigma_\beta) = -5.7\,\text{eV}$) is high in the nanomesh holes, while in the maps measured at the bias voltage of σ_α ($V(\sigma_\alpha) = -4.6\,\text{eV}$) the highest LDOS is on the nanomesh wires. Therefore the holes are the regions of the nanomesh in close contact with the rhodium and which give the highest contribute to the bonding to the substrate. The wires which are pushed away from the surface appear at lower binding energies. This clear spectroscopic imaging is facilitated by the insulating nature of the *h*-BN layer, where the σ bands are the first BN-electronic states below the Fermi level that contribute to the tunneling. The weight of the holes or the wires in the total area

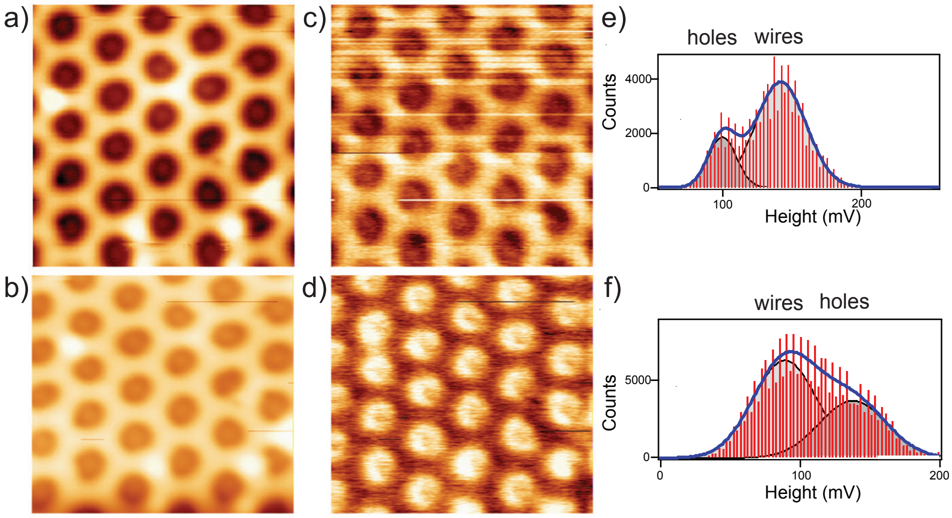

Figure 27: *(a) and (b) Constant current STM images (15×15 nm^2, 15×13 nm^2) of the same area of h-BN on a Rh(111) film (80 nm thick) grown on Al_2O_3(0001) taken at I_t=0.1 nA and bias voltages V_s=-4.6 V and V_s=-5.7 V respectively. Conductivity maps recorded simultaneously with the topographic images (a) and (b) are shown in (c) and (d). In the map (c) measured at $E_B(\sigma_\alpha)$=4.6 eV the area occupied by the nanomesh holes is the 22% of the total area, while in the map (d) measured at $E_B(\sigma_\beta)$=5.7 eV the holes occupy the 37%. These values are estimated from the area of two Gaussian components resulting from the fit of the total area of the image histogram (i.e. the distribution of the voltage modulation) in (e) and (f).*

in the dI/dV maps changes depending on the bias voltage. At $\mathrm{V} = -5.7\,\mathrm{eV}$ the area defined by the holes is 37%, and it is reduced to 22% at $\mathrm{V} = -4.6\,\mathrm{eV}$. These values differ from the one found in normal emission UP spectra. It is not clear yet how the photoemission cross section of the σ peaks depends on the registry and height of the boron nitride with respect to the substrate. Nevertheless, it might be possible that in the photemission process the σ_β component, which is so broad in normal emission UP spectra, is due to the nanomesh holes (with $\sim 1.6\,\mathrm{nm}$ diameter) and the rims, while σ_α is given only by the inner part of the wires, the highest parts in the nanomesh. In fact, the area of the *h*-BN in the holes and in the rims can be calculated as a circle with a diameter of 3 nm due to the distance between 13 N(B) atoms in the holes plus the rims. Its value is $\sim 7.07\,\mathrm{nm}^2$ and since the area of the nanomesh unit cell is $8.87\,\mathrm{nm}^2$, then the holes/rims occupy the 80%.

4.4.1 The valence band dispersion from ARUPS

The valence band structures of the clean Rh(111) and of the *h*-BN covered surface measured with a photon energy of 21.22 eV are shown in Fig. 28. The ARUP spectra were collected along the $\overline{\Gamma \mathrm{K}}$ and $\overline{\Gamma \mathrm{M}}$ symmetry directions in the first surface Brillouin zone (SBZ) on the Rh(111) and on the *h*-BN/Rh(111) surfaces. The size of the hexagonal first SBZ of Rh(111) along these two directions is defined by the vectors $\overline{\Gamma \mathrm{K}} = 1.55\,\mathring{\mathrm{A}}^{-1}$ and $\overline{\Gamma \mathrm{M}} = 1.35\,\mathring{\mathrm{A}}^{-1}$ and for the first SBZ of *h*-BN(0001), by $\overline{\Gamma \mathrm{K}} = 1.67\,\mathring{\mathrm{A}}^{-1}$ and $\overline{\Gamma \mathrm{M}} = 1.45\,\mathring{\mathrm{A}}^{-1}$. The two SBZ are in registry with each other (i.e. the *h*-BN(0001) SBZ is not rotated to the Rh(111) one). Previous ARUPS experimental studies performed with synchrotron radiation at several photon energies ($h\nu = 24, 32, 42, 60\,\mathrm{eV}$) are reported for the clean and hydrogen-covered Rh(111) surface [113]. In the band dispersion two

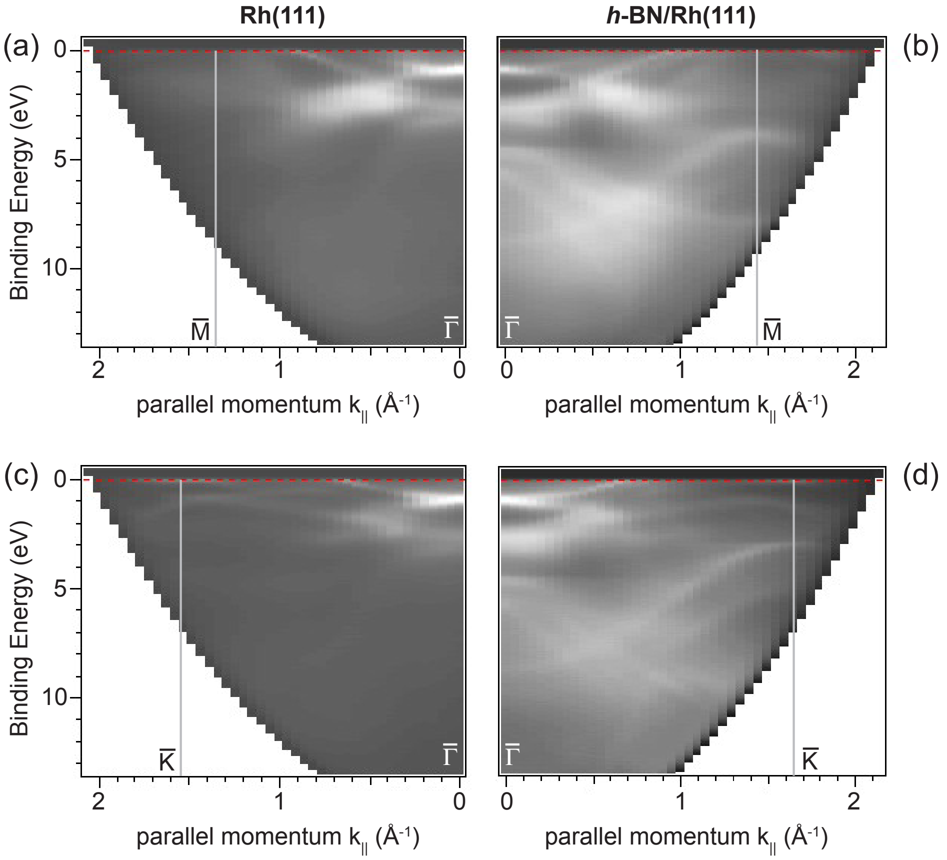

Figure 28: *Angle resolved He Iα dispersion plot for clean Rh(111) ((a) and (c)) and h-BN/Rh(111) ((b) and (d)) along the azimuths* $\overline{\Gamma M}$ *and* $\overline{\Gamma K}$ *respectively. The data are plotted with respect to the Fermi level. The* $\overline{\Gamma}$, $\overline{M}$, $\overline{K}$ *points in the first SBZ are indicated. In the gray scale the highest intensity is white.*

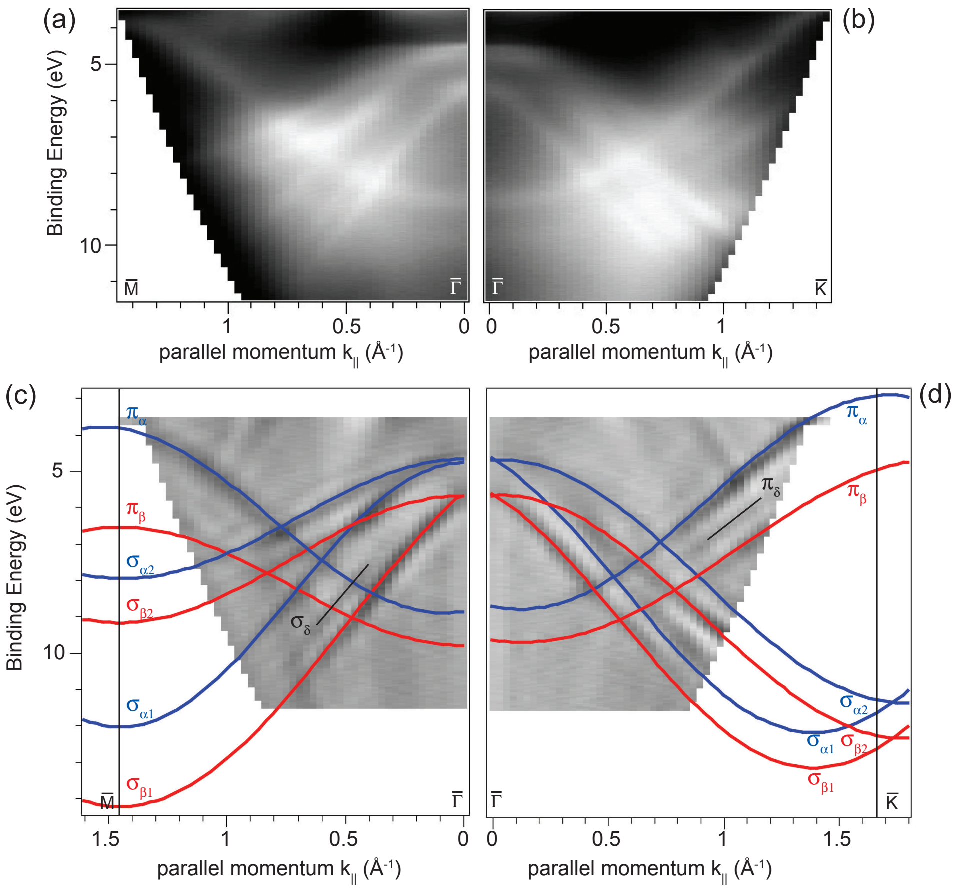

Figure 29: *(a-b) Angle resolved He Iα dispersion plot for the h-BN on Rh(111) measured with a smaller energy and momentum range than in Fig. 28(b) and (d) and with a higher energy and angle resolution. (c-d) Second derivative of the dispersion plots in (a-b) showing the variation in the curvature of the bands. The most probable assignment of the bands appearing is plotted in the graphs. These curves result from a fitting of the experimental dispersion with a sinusoidal function* ($E(k_{||}) = E_0(k_{||}) + \Delta E \sin(\tau k_{||} + \phi)$)*, in a simple tight binding model for band structure calculations.*

bands located at binding energies 0.6 and 2.5 eV at the zone center ($\overline{\Gamma}$) were identified as surface resonances, and with 55 eV photon energy a third more tightly bound surface band appeared at 5.5 eV below E_f at $\overline{\Gamma}$. Surface resonances at 2.5 and 5.4 eV were also predicted theoretically [114]. Two surface states were found (at $h\nu > 24$ eV) inside the projected bulk band gap at 2 eV below E_f near $\overline{\text{K}}$. These two clearly distinguishable bands were degenerate at $\overline{\text{K}}$. The positions of these surface states as determined from theory lie 0.5 eV below the experimental values. The ARUP spectra shown here resemble the experimental data reported in [113]. At $\overline{\Gamma}$ a sharp peak appears at 0.9 ± 0.05 eV binding energy (0.3 eV lower than in [113], but this could be due to the different photon

± 0.1eV	$E_B(\overline{\Gamma})$	$E_B(\overline{\mathrm{K}})$	$E_B(\overline{\mathrm{M}})$	$E_B(\overline{\Gamma}) - E_B(\overline{\mathrm{K}})$	$E_B(\overline{\Gamma}) - E_B(\overline{\mathrm{M}})$
$\sigma_{\alpha 1}$	4.57	11	7.8	6.43	3.23
$\sigma_{\alpha 2}$	4.57				
$\sigma_{\beta 1}$	5.7	12.5		6.8	
$\sigma_{\beta 2}$	5.7				
σ_0	24.1	19.2		4.9	
π_α	8.76	3.1	3.9	5.66	4.86
π_β	9.83	4.9		4.93	

Table 2: *Binding energies values given with respect to the Fermi level for the h-BN-related bands on h-BN/Rh(111). The values are given in eV and the error bar is 0.1 eV.*

energies used), and a broader one with two components at 2.6 and 3.2 ± 0.05 eV. The surface states in the band gap around $\overline{\mathrm{K}}$ and the surface resonance at 5.5 eV are not detected with He Iα radiation.

When the Rh(111) surface is covered with *h*-BN the Rh bands survive and the pairs of σ and π bands and their dispersion can be well resolved by ARUPS. The *h*-BN states lie far from the Rh bands thus they do not take a major role in the conductivity of the *h*-BN/Rh(111) structure. Since no new states belonging to the *h*-BN cross the Fermi level, the *h*-BN film is considered as an 'insulator'. In this study no experiments were performed in order to detect subtle changes in the substrate band dispersion and band positions induced by the presence of the *h*-BN. In the case of *h*-BN on Ni(111) and on other metal surfaces (as previously reported) the σ band is due to two components which are degenerate at $\overline{\Gamma}$ and split in two branches (σ_2 and σ_1) as the parallel component of the momentum increases towards $\overline{\mathrm{K}}$ and $\overline{\mathrm{M}}$. For the nanomesh, in order to assign the several bands that appear in the ARUP spectra in Fig. 28(b) and (d) to σ_α, σ_β, π_α and π_β, the same measurements were taken with a higher energy and angular resolution (pass energy= 2 eV and $\Delta\theta = 0.1°$) in a smaller energy range in the $\overline{\Gamma\mathrm{K}}$ and $\overline{\Gamma\mathrm{M}}$ directions. All the nanomesh related bands can be clearly distinguished (Fig. 29). Each σ band splits in two components which are degenerate at $\overline{\Gamma}$, they are indicated as $\sigma_{\alpha 2}$ and $\sigma_{\alpha 1}$, $\sigma_{\beta 2}$ and $\sigma_{\beta 1}$ in Fig. 29(c) and (d). The dispersion of the bands belonging to the same *h*-BN species, the 'α' ones (i.e. $\sigma_{\alpha 1}$, $\sigma_{\alpha 2}$ and π) and the 'β' ones (i.e. $\sigma_{\beta 1}$, $\sigma_{\beta 2}$ and π), is similar to the one found for the single *h*-BN layer on Ni(111). Two other bands labeled σ_δ and π_δ appear and an investigation of their origin will be discussed in the next paragraph. Angle resolved UP spectra measured with He IIα radiation allow to reach a wider energy and momentum range. In Fig. 30 the dispersion along $\overline{\Gamma\mathrm{K}}$ of the *h*-BN/Rh(111) is shown. At energies around 24 eV below E_f, a third sigma band (σ_0) appears. A third sigma

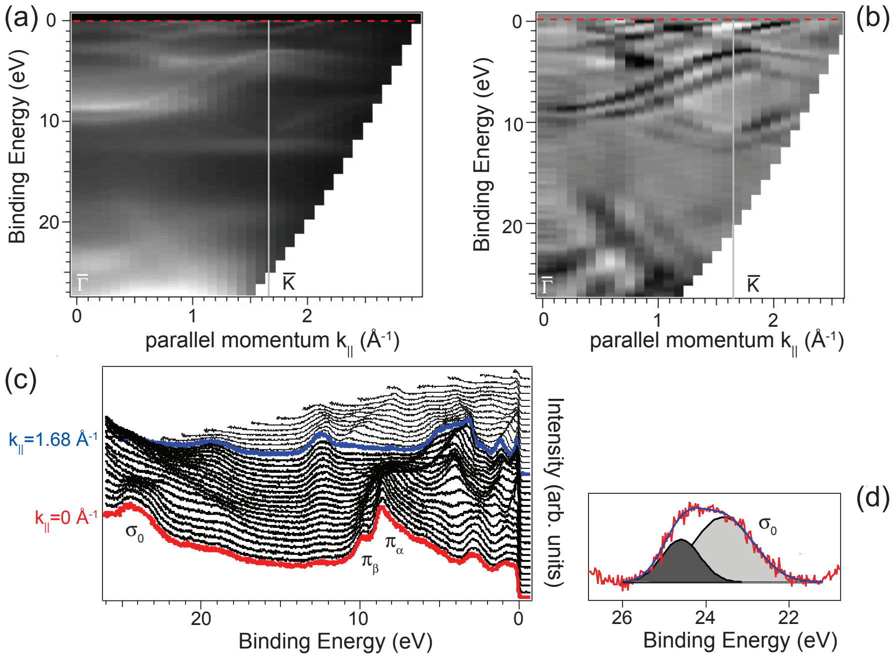

Figure 30: *(a) Angle resolved He IIα dispersion plot for h-BN on Rh(111). At this photon energy it is possible to follow the dispersion of h-BN related bands up to $\overline{K}$ and a third sigma band (σ_0) appears at 24.4 eV at $\overline{\Gamma}$. In (b) the second derivative of the measurement is shown. The two π bands, $\sigma_{\alpha 1}$ and $\sigma_{\beta 1}$ are well visible. π_α and π_β are better resolved due to their higher scattering cross sections as can be seen in (c) for example in normal the emission spectra. The flat band at 12.3 eV is probably due to contamination during the data acquisition. The enlarged spectral region of σ_0 that can be measured with this photon energy is shown in (d). The component at lower binding energy covers the 70% of the total area of the band, while the higher energy component occupies only the 30%, opposite behavior than the other σ bands.*

band is always expected for *h*-BN due to the three sp^2 orbitals shared by the boron and nitrogen atoms in each BN-unit. Theoretical calculations found such a band at $\sim 19\,\text{eV}$ below E_f for bulk *h*-BN [115] with a band width of $\sim 3\,\text{eV}$. σ_0 at $\overline{\Gamma}$ appears as a broad peak that can be due to two components centered at 23.6 eV and 24.6 eV. Their splitting in binding energy of 1 eV is similar to the one of σ_α and σ_β, so they could eventually be assigned to the 'α' and 'β' groups of bands respectively (Fig. 30(d)). The values for the positions of the σ and π bands measured with the two different photon energies are tabulated in Table (2). The band widths ($\Delta E_{\overline{\Gamma\mathrm{K}}} = E_B(\overline{\Gamma}) - E_B(\overline{\mathrm{K}})$) have similar values to those found with theoretical methods for *h*-BN/Ni(111) (for a buckled BN layer): $\Delta E_{\overline{\Gamma\mathrm{K}}}(\sigma_1) = 6.7\,\text{eV}$ vs $\Delta E_{\overline{\Gamma\mathrm{K}}}(\sigma_{\alpha 1}) = 6.4\,\text{eV}$ and $\Delta E_{\overline{\Gamma\mathrm{K}}}(\sigma_{\beta 1}) = 6.8\,\text{eV}$; $\Delta E_{\overline{\Gamma\mathrm{K}}}(\pi) = 5.3\,\text{eV}$ vs $\Delta E_{\overline{\Gamma\mathrm{K}}}(\pi_\alpha) = 5.7\,\text{eV}$ and $\Delta E_{\overline{\Gamma\mathrm{K}}}(\pi_\beta) = 4.9\,\text{eV}$.

4.4.2 The nanomesh superstructure in the first *h*-BN-SBZ

In the ARUPS dispersion plots of *h*-BN on Rh(111) presented so far, the identification of all the bands is still not clear. In fact σ_δ and π_δ shown in Fig. 29 cannot be assigned directly to branches of the 'α' and 'β' bands. These bands could be due to *h*-BN rotated domains on the surface [116], or they could belong to a third BN species in the nanomesh, or they can be *umklapp* bands [117, 118], seen as replica of the σ and π bands in the first SBZ shifted by a nanomesh reciprocal lattice vector. In order to investigate this issue an energy map has been measured at a binding energy where σ_δ is clearly visible, i.e. at 9.78 eV. At this energy from Fig. 29 and Fig. 28 along $\overline{\Gamma \mathrm{M}}$ the sigma bands are found at $\mathrm{k}_{||}(\sigma_{\beta1})$=0.55 Å^{-1}, $\mathrm{k}_{||}(\sigma_{\alpha1})$=0.92 Å^{-1}, $\mathrm{k}_{||}(\sigma_\delta)$=0.69 Å^{-1}, and along $\overline{\Gamma \mathrm{K}}$ at $\mathrm{k}_{||}(\sigma_{\beta1})$=0.69 Å^{-1}, $\mathrm{k}_{||}(\sigma_{\alpha1})$=0.87 Å^{-1}, $\mathrm{k}_{||}(\sigma_{\beta2})$=1 Å^{-1}, $\mathrm{k}_{||}(\sigma_{\alpha1})$=1.25 Å^{-1}. σ_δ along $\overline{\Gamma \mathrm{M}}$ appears at the same $\mathrm{k}_{||}$ as $\sigma_{\beta1}$ along $\overline{\Gamma \mathrm{K}}$, thus one could think that it belongs to a dispersion in $\overline{\Gamma \mathrm{K}}$ due to some *h*-BN units on the surface rotated by 30°. Also in LEED images sometimes *h*-BN principal lattice spots appear rotated by 30° with respect to the others. In the energy map one would expect to see another rotated *h*-BN Brillouin zone resembling the not-rotated one but this is not the case: the *h*-BN units maintain a single orientation with respect to the substrate. For this reason this interpretation is not correct. An assignment of σ_δ to an *umklapp* band is also not straightforward: if σ_δ would be a replica of $\sigma_{\beta1}$ then one would expect to see it shifted in $\mathrm{k}_{||}$ of a nanomesh reciprocal lattice vector. The length of such a vector is 0.223 Å but the difference in $\mathrm{k}_{||}$ here observed is only 0.15 Å. This energy map can be compared to the one measured for *h*-BN on Ni(110) shown in Fig. 12, even if they have been measured at different binding energies. If each set of bands, the 'α' and 'β', would behave as the σ and π observed in the Ni case, then it is expected to see the dispersion of the $\sigma_{\beta1}$ and $\sigma_{\alpha1}$ as circles centered at $\overline{\Gamma}$ and with different diameter than for the Ni due to their offset in binding energy ($\sim$ 1.1 eV at $\overline{\Gamma}$). For the $\sigma_{\beta2}$ and $\sigma_{\alpha2}$ two small arcs centered along $\overline{\Gamma \mathrm{K}}$ and close the $\overline{\mathrm{K}}$ point in the first SBZ are expected. These last two bands well match the expectations. An azimuthal carpet measured in angular range of ±88° around the $\overline{\Gamma \mathrm{K}}$ at $\theta = 72°$ shows that $\sigma_{\beta2}$ and $\sigma_{\alpha2}$ are not rotated one with respect to the other but are centered and disperse symmetrically with respect to $\overline{\mathrm{K}}$. Even a third replica of these bands appears in the direction orthogonal to $\overline{\mathrm{K}}$ and they are shifted one to each other by 0.7 ± 0.1 eV in biding energy. The explanation of the bands present in the centre of the map, especially the intense hexagon is not trivial and not yet understood. It can be reproduced with the superposition of 'circular' $\sigma_{\beta1}$ and $\sigma_{\alpha1}$ centered at $\overline{\Gamma}$ (as for the *h*-BN on Ni(110)) shifted along the six $\overline{\Gamma \mathrm{K}}$ directions in the first *h*-BN SBZ by a nanomesh reciprocal lattice vector 0.223 Å long (Fig. 31(c)). This procedure generates a Moiré-like hexagon at the expected position but besides this, high intensity should also be seen

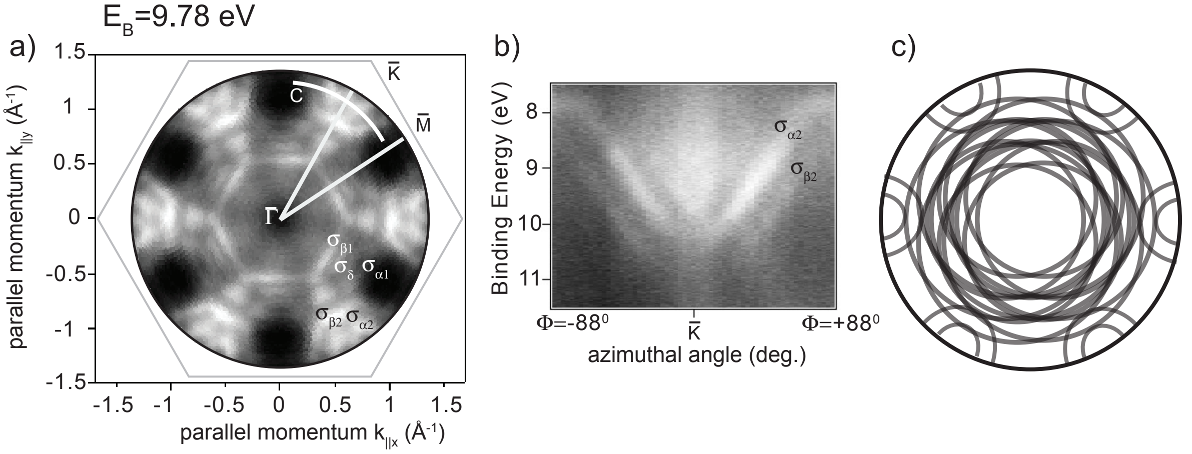

Figure 31: *(a) Energy map measured at 9.78 eV for h-BN on Rh(111). White is high intensity. The white lines indicate the polar cuts measured in Fig. 29(a) and (b). The position at which the different bands are found in the polar cuts is indicated. The azimuthal cut C in (a) measured around $\overline{\mathrm{K}}$ is shown in (b). (c) Possible model to explain the band seen in (a) based on the data from h-BN on Ni(110), Fig. 12. Two circles centered at $\overline{\Gamma}$ with radius $k_{||}=0.69$ Å^{-1} and $k_{||}=0.87$ Å^{-1} are shifted of 0.223 Å^{-1} in the six $\overline{\Gamma K}$ directions. The hexagons are due to a Moiré pattern created by the superposition of the circles.*

inside the hexagon and between the σ bands around the $\overline{\mathrm{K}}$ points, which is not found experimentally. Moreover it would imply that the strong $\sigma_{\beta1}$ dispersing in $\overline{\Gamma\mathrm{M}}$ (Fig. 29), since laying on the hexagon would be an *umklapp* band. Another critical issue not raised so far is that in the nanomesh unit cell all the 169 N and 169 B atoms occupy different adsorption sites, therefore they all have a different chemical environment. This would lead in the nanomesh band structure to 169 different σ and π bands, but here only two kinds (the 'α' and the 'β') are clearly identified, and even a third eventual 'δ' species might be present. In view of this also the understanding of the energy maps requires theoretical calculations with the entire nanomesh unit cell.

4.5 XPD study of the nanomesh

XPD patterns have been measured for the N 1*s* and the B 1*s* core levels on the *h*-BN on Rh(111) at kinetic energies of 856 eV and 1063 eV respectively. They are shown in Fig. 32. The patterns have been azimuthally averaged exploiting the threefold symmetry of the system and normalized with the mean intensity for each polar angle. The center of the plot corresponds to the surface normal (the [111] direction) while the outer circle represents grazing emission along the surface. The crystallographic directions are given with respect to the orientation of the substrate found from the Rh 3*s* and Rh 3*d* XPD

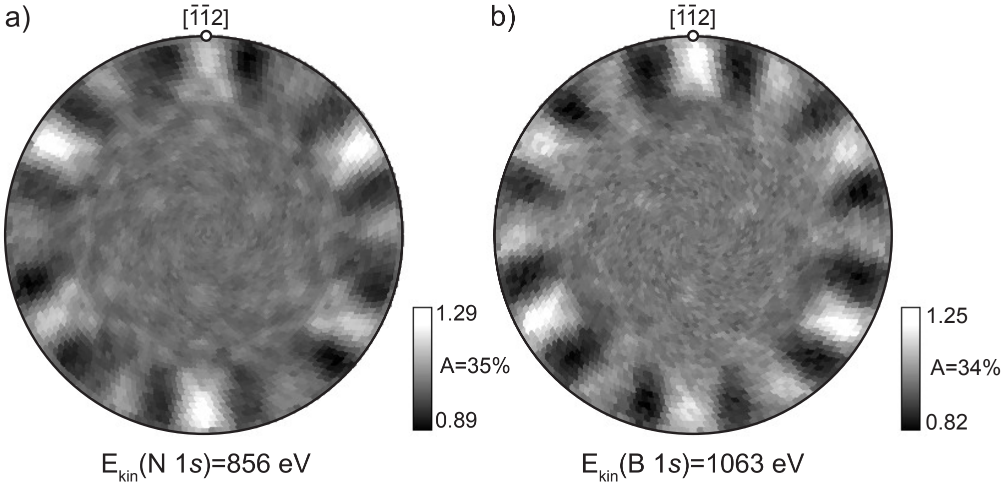

Figure 32: *XPD patterns for h-BN on Rh(111). (a) N 1s pattern measured at 856 eV, (b) B 1s pattern measured at 1063 eV kinetic energy with Mg Kα as photoelectrons excitation source. White is high intensity. The patterns are shown in stereographic projection.*

patterns which have been measured with and without *h*-BN. In the patterns sharp interference fringes appear, indicating a high degree of coherence in the scattering processes and in the order of the atomic structure around the emitters. The two patterns have the same anistropy A=$\sim$ 35% (where A is defined as: $A = (I_{max} - I_{min})/I_{max}$). The three-fold symmetry of the system indicates that the *h*-BN layer discriminates between *fcc* and *hcp* adsorption sites, therefore the role of the second Rh layer below the surface and that of the B preferential site occupation [104] are important for the nanomesh growth. In order to better interpret these data, it is useful to compare them with the XPD patterns measured in the same experimental conditions for the *h*-BN on Ni(111). This is a much simpler system than the nanomesh since the local environment is the same for each atom.

4.5.1 XPD and MSC for *h*-BN on Ni(111)

XPD patterns for *h*-BN on Ni(111) have been measured with different lens settings for the electron analyzer with respect to published data and at a different kinetic energy for the B 1s emission [87]. In this way the features that were not easily showing up before are enhanced. In the experimental patterns highly resolved interference fringes appear as bright half circles surrounding the intense maxima at grazing emission as in Fig. 33(a) and (b). In the interpretation of these patterns in [87], the bright maxima are found along the emitter-B or -N nearest neighbor bond directions while the circles

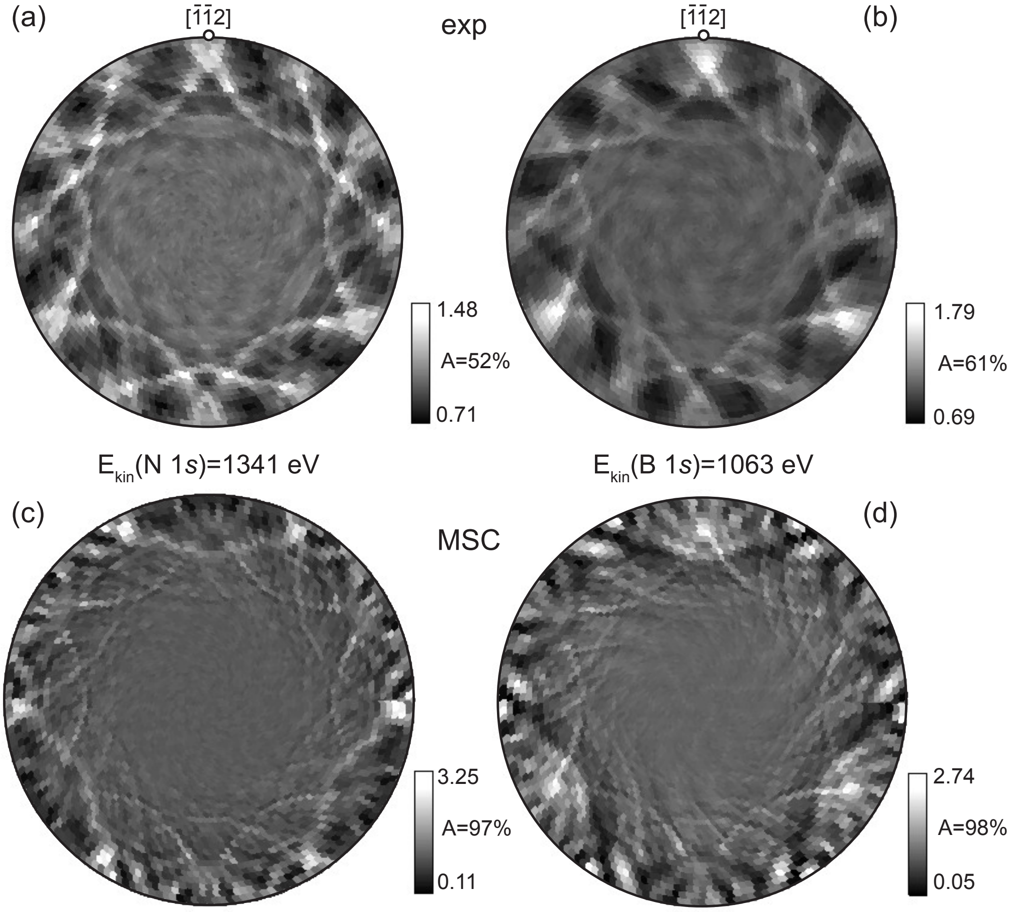

Figure 33: *XPD patterns for h-BN on Ni(111). (a) N 1s pattern measured at E_{kin}=1341 eV (with Si Kα radiation), (b) B 1s pattern measured at E_{kin}=1063 eV kinetic energy (with Mg Kα radiation). The patterns are shown in stereographic projection. (c) and (d) corresponding simulated pattern with multiple scattering calculations (MSC).*

are interference cones mapped in stereographic projection. Whenever such cones cross each other, sharp maxima are found in the circles. These speckles are due to a non linear addition of the diffraction intensity caused by the coherent emission from a single atom and by the scattering processes with the neighboring ones. The two patterns are similar one to the other, but while the B 1s is threefold the N 1s has an almost six-fold symmetry. These patterns have been simulated within the multiple scattering theory (MSC) and the agreement between calculations and experiments is surprisingly good. In the simulations a simple atomic cluster of (6 × 6) *h*-BN units on a single layer of Ni atoms with in-plane N-N and Ni-Ni distance of 2.49 Å has been used. The N atoms are *on top* Ni sites, the B on *fcc* sites. The best agreement is found when the B atoms are 0.1 Å lower than the N and the N are 1.95 Å higher than the Ni atoms. The other

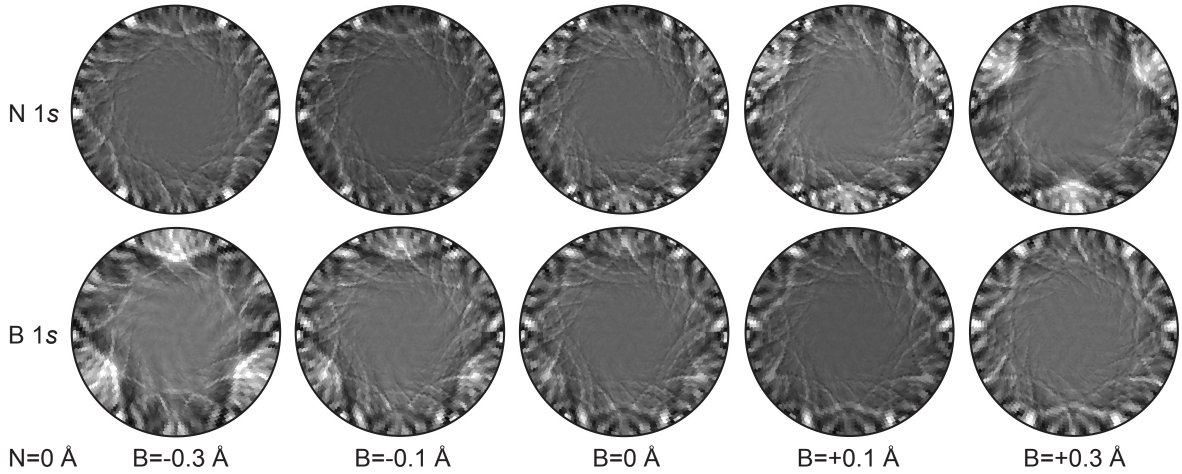

Figure 34: *MSC calculations for the N 1s (E=1341 eV) and the B 1s (E=1063 eV) XPD patterns. The atomic cluster used contains only one h-BN-layer with size (6×6) h-BN units. The out of plane coordinate of the N atoms is kept fixed at 0 Å, while the one of the B is changed between -0.3 Å to +0.3 Å.*

parameters have been optimized to the values of 13 eV for the inner potential, $0.002\,\text{Å}^2$ for the mean square displacement and $11\,\text{Å}^{-1}$ for the inelastic attenuation length. The multiple scatting level used is 5 (i.e. a photoelectron scatters at most 5 times before being emitted on the surface) which produces rather different results as compared to those obtained with single scattering calculations (SSC) where only one single scattering event is taken into account. These simulations give a further confirmation that the geometrical model proposed for the *h*-BN on Ni(111) is correct [86–88]. The three-fold symmetry in the B 1*s* pattern is due to the fact that the B atoms in the *h*-BN layer sit closer to the surface than the N atoms. A series of MSC simulations have been done for a single *h*-BN layer changing the height of the B atoms and maintaining the N at fixed positions. The outcome can be seen is Fig. 34. The bigger the height difference between the two atomic species is taken, the more threefold the pattern becomes. The bright fringes found at grazing emission angles were previously interpreted as forward scattering peaks from SSC calculations. With MSC these broad maxima are well resolved and they are not due to a single peak but to many interference fringes one near the other and their diameter gets smaller the closer the two atoms are.

Experimentally the B 1*s* XPD patterns can change due to different site occupation of the B atoms. If the B atoms adsorb on *fcc* sites, the pattern coincides with the one in Fig. 33. The same pattern has also been measured rotated by 60° (with the same anisotropy $A\sim$ 60%) when all the B atoms prefer to take the *hcp* position. A mixture of the two is also observed depending on the preparation conditions [63]. The possible formation of these domains is clarified by DFT calculations. In fact it is found that the energy difference between the two structures with B atoms adsorbed on *fcc* or on *hcp* sites and N atoms on top positions is only 18 ± 4 meV. Therefore both structures can be found on the surface with similar probability.

4.5.2 Nanomesh domains in XPD

Already the data of *h*-BN/Ni(111) present a relevant degree of complexity. For the nanomesh it is even more difficult to assign the intense maxima in the patterns to the interference between two particular emitters-scatterers since the unit cell is big and each

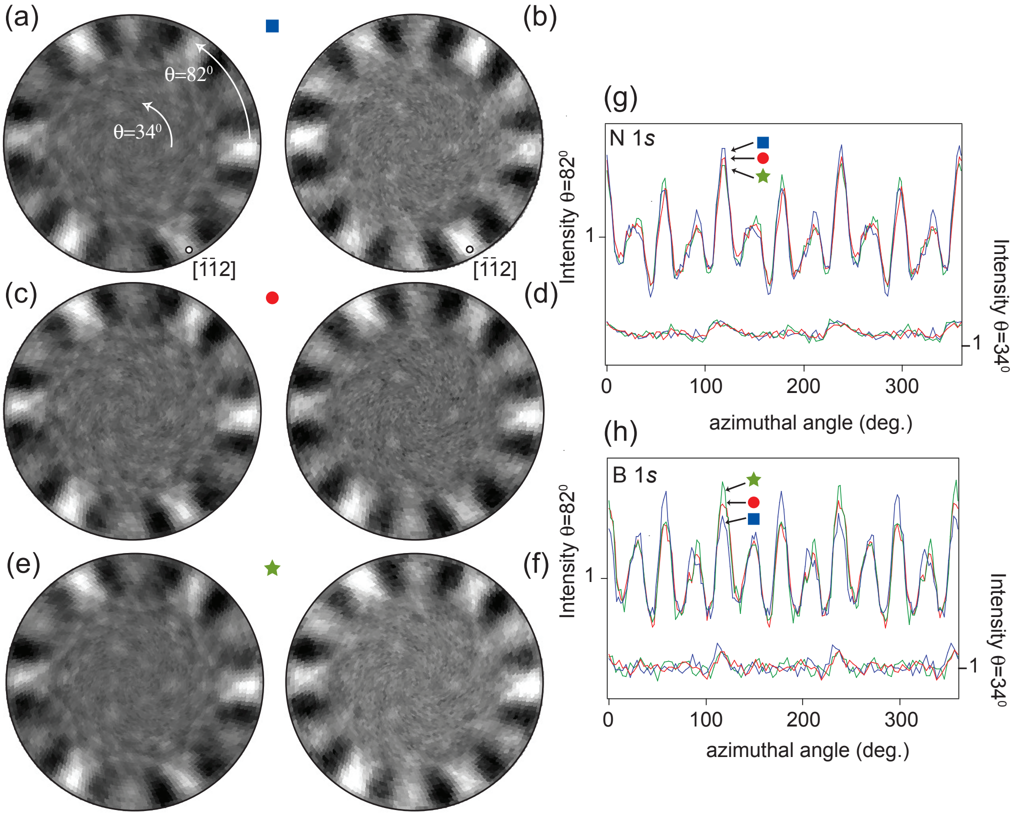

Figure 35: *XPD patterns measured for different h-BN/Rh(111) preparations. On the left column are shown the N 1s XPD pattern while on the right the corresponding B 1s. In (g) and (h) the azimuthal cuts are plotted taken respectively in the N 1s XPD and in the B 1s ones at the angle indicated in (a): θ=82° and θ=34°. The values for the anisotropy in the cuts is reported in Table (3). The symbols in the graph show the correspondence between the lines and the patterns.*

	A(N 1s) Fig. 35(a)	A(N 1s) Fig. 35(c)	A(N 1s) Fig. 35(d)
$\theta = 82^\circ$	36%	31%	32%
$\theta = 34^\circ$	6%	7%	5%
	A(B 1s) Fig. 35(b)	A(B 1s) Fig. 35(d)	A(B 1s) Fig. 35(e)
$\theta = 82^\circ$	31%	34%	32%
$\theta = 34^\circ$	10%	8%	9%

Table 3: *The table reports the values for the anisotropy in the azimuthal cuts shown in Fig. 35(g) for the N 1s XPDs and in Fig. 35(h) for the B 1s XPDs.*

atom has its own chemical surrounding. Also for the nanomesh different domains can be found. The three-fold symmetry can change and get enhanced from preparation to preparation. A systematic study has not been done in order to control this phenomenon but the results in Fig. 35 indicate that the energy balance in the system is so subtle that small changes in the kinetics or thermodynamics of the self-assembly process can lead to different morphology of the film. Small changes in the temperature, in the duration of the annealing time during the nanomesh preparation or in the quantity of O_2 used in the cleaning process of the substrate, can be some of the causes. In Fig. 35 the XPD of the N 1s and the B 1s signals have been measured for three different h-BN/Rh(111) structures prepared in the same experimental conditions. As can be seen in Fig. 35 the symmetry of the pattern changes: for the B 1s the peaks at grazing emission are 60° rotated from (b) to (d) and (f) indicating a switching between the preferential adsorption sites of the B atoms, while the N 1s pattern changes from three-fold in (a) to more six-fold in (c) and (e). In all the XPD patterns, three maxima emerge always in the same position at polar angles around $\theta = 34^\circ$. The anisotropies of these peaks remain constant (6% for the N 1s and 9% for the B 1s) and are not correlated to the changes in the anisotropies of the peaks at grazing emission ($\theta = 82^\circ$) as shown in Fig. 35(g) and (h) and tabulated in Table (3). In order to verify that these peaks belong to N or B species and not to the substrate, the whole N 1s peak (E_{kin} from 849.5 to 861.5 eV) has been measured at $\theta = 32^\circ$ (Fig. 36(a)) and $\theta = 34^\circ$ in an azimuthal range of $\Delta\phi = 168^\circ$ and $\Delta\phi = 240^\circ$ respectively. The data have been analyzed in different ways. (i) Each spectrum has been fitted with a Gaussian curve with a linear background and fixed FWHM (1.72 eV). The resulting variation of the normalized intensity of the peak and of the background with respect to the azimuthal angle for the spectra measured at $\theta = 32^\circ$ is plotted in Fig. 36(d). Clearly two maxima appear in the position expected from the azimuthal cuts in the XPD patterns in Fig. 35(g), i.e at $\phi = 115^\circ$ and at $\phi = 234^\circ$. The third peak is not contained in the azimuthal angle range used in the experiments. The spectra

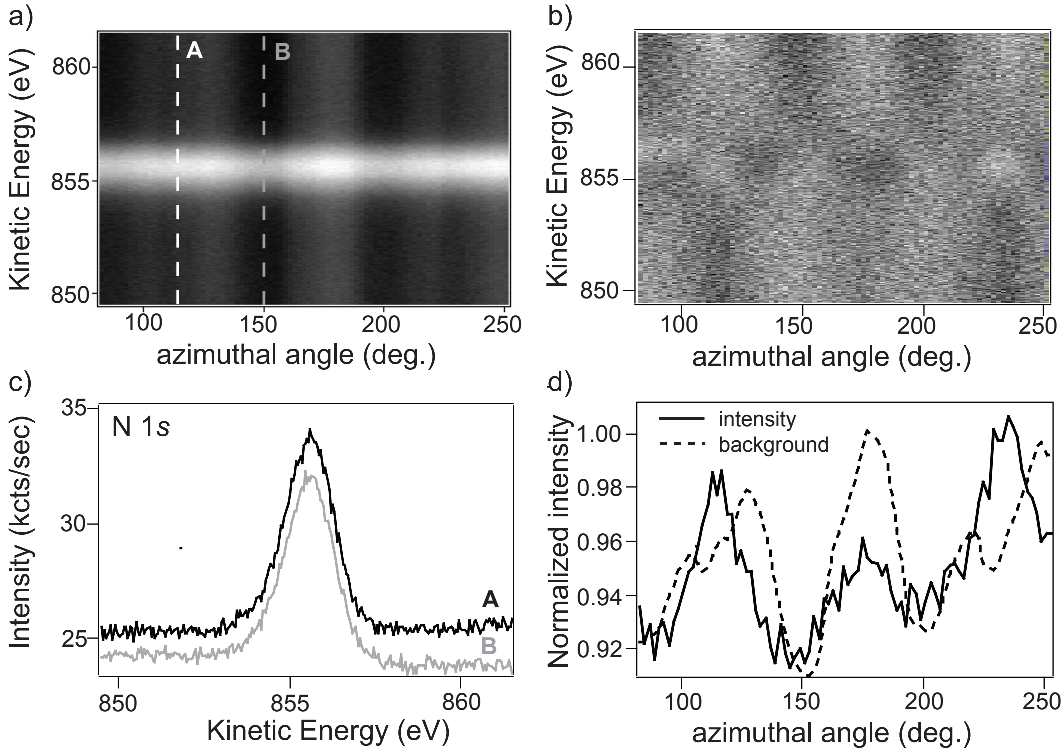

Figure 36: *(a) Energy scan measured with Mg Kα at θ=32°, as a function of the azimuthal angle in the range from 849.5 to 861.5 eV, corresponding to the N 1s emission in h-BN/Rh(111). The angles are given referring to the sample orientation in Fig. 35. (b) The spectra in (a) have been first averaged in energy and then in angle. The resulting anisotropy in the N 1s spectra shows bright spots at the position of the inner maxima in the XPD patterns in Fig. 35. (c) The spectra on the peak at 115° and on the background 155° corresponding to the lines in (a) are shown. (d) Variation of the normalized intensity of the peak and of the background of each spectrum in (a) with respect to the azimuthal angle. They are found by fitting each spectrum with the same Gaussian curve with a linear background and fixed FWHM.*

measured on the peak (at $\phi = 115°$) and at the minimum (at $\phi = 153°$) are shown in Fig. 36(c). As can be seen in Fig. 36(d), also the intensity of the background is modulated in a similar way as that of the N 1*s* peak but there is a shift of $\sim 12°$, suggesting that the photoelectrons emitted at these energies undergo different scattering processes. As already well described in previous studies [119], the electrons constituting the inelastic tail of XPS core lines are reflected off low-index crystal planes before they leave the crystal. They produce diffraction patterns like the elastically scattered electrons, but in directions different from those defined by the crystal planes. Furthermore they are highly sensitive to the geometry of the electron source which could lead to asymmetric diffraction patterns. The background intensity can show anisotropies as high as 10% in

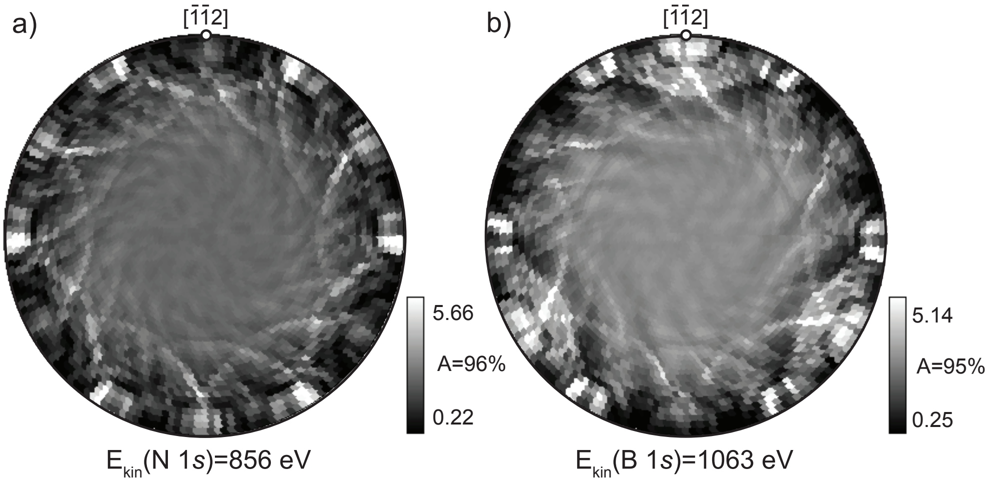

Figure 37: *Multiple scattering X-ray photoelectron diffraction calculations of h-BN on Rh(111) for a unit cluster optimized within an ab initio force field approach. (a) N 1s (E_{kin}=856) emission. (b) B 1s (E_{kin}=1063) emission.*

the patterns [119]. Therefore it is not surprising to see that also for the intensity of the background discussed here the anisotropy is as high as the one of the elastically scattered N 1s electrons. (ii) Each spectrum in Fig. 36(a) has been normalized in the energy- and in the angular-range so that each peak has the same area. The variation of the normalized intensity is shown in Fig. 36(b). This plot gives information on the anisotropy in the spectra: it is enhanced in the white spots that again appear around $\phi = 115°$ and $\phi = 234°$, while it decreases at the dark spots which are due to the background. To conclude the peaks that appear at $\theta = 32°$ and $\theta = 34°$ in the XPD patterns belong to the N 1s emission and are not due to the background, and have an anisotropy of 7% as found from the two measurements at the two different polar angles. In the N 1s and B 1s XPD patterns, while the peaks far from the center are due to the atoms on top of the Rh layers, thus belonging to the nanomesh, the three inner spots are due to emitters which are placed below the surface, subsurface N or B atoms.

Multiple scattering calculations (MSC) for the *h*-BN on Rh(111) XPD patterns have been performed on a nanomesh cluster theoretically optimized by *Laskowski et al.*, where the *h*-BN forms a corrugated layer, but still the positions of the Rh atoms are kept fixed. From the entire cluster with (13 × 13) *h*-BN units, only a part with (8 × 8) *h*-BN units around the emitter has been considered. Since all the B and N atoms occupy unequivalent positions within the nanomesh unit cell, the patterns from all the different B and N emitters have been simulated. The resulting sum of 169 patterns for the N 1s and of 169 patterns for the B 1s are shown in Fig. 37(a) and (b) respectively. The calculations have been optimized with an inner potential of 13 eV, a mean square displacement of 0.002 $Å^2$ and an inelastic attenuation length of 11 $Å^{-1}$. The multiple scatting level used is 3. The three-fold symmetry of the experimental patterns in Fig. 32 is reproduced in these simulations, as well as the bright interference fringes. An higher order level in the multiple scattering and an optimization of the vertical displacement of the B, N and Rh atoms in the cluster could lead to a better agreement between theory and experiments.

4.6 The nanomesh as template

The fabrication of regular and periodic metal and semiconductor nanostructures or molecular arrangements at surfaces on the nanoscale is still a challenging task. The ideal approach is to grow them on pre-patterned substrates which are able to guide and impose a preferential ordering. The nanomesh represents an ideal template. It is highly ordered on the entire Rh surface, it has a periodicity of only 3.2 nm and since it is an insulating layer, it can decouple the adsorbed species from the metal below. Can the nanomesh be used as molecular trap? C_{60} molecules have been used as first nanomesh 'guest' molecules since their size of ~ 1 nm can match the nanomesh lattice. The bond strength and character observed in the interaction between the C_{60} and the various substrates on which it has been deposited ranges from weak van der Waals interactions on inert surfaces such as graphite [120], SiO_2 [121], GeS(001) [122] or *h*-BN/Ni(111) [123] to chemisorption on metal surfaces [124,125]. In the last case the degree of hybridization of the C_{60} molecular orbitals with the substrate electronic states and the charge transfer differ significantly from metal to metal. At high coverages usually these molecules arrange in close-packed overlayers with intermolecular distances close to that of the van der Waals bonded solid C_{60} of 10.02 Å [126]. C_{60} can be responsible for strong surface reconstructions as seen for C_{60} on Ni(110) [127] and on Au(110) [128]. C_{60} is observed to be adsorbed with different geometries and orientations on metal surfaces (e.g. sitting on a hexagon or on a pentagon), and due to the interaction with the substrate the molecules are not freely rotating as in the bulk. The distinct adsorption configurations of the C_{60} induce different charge transfer from the substrate to the C_{60} lowest unoccupied molecular orbital (LUMO) and the resulting electronic arrangement can be recognized by STM. In fact C_{60} molecules are frequently observed with different imaging height or intramolecular features. Nevertheless since STM images a convolution of the surface electronic and geometric structure, it is often controversial to determine unambiguously weather the contribution to the contrast is due to a difference in the geometrical height or to electronic effects. XPD on the other hand has proven to be a powerful means to determine the orientation of the C_{60} cage at surfaces [124,129,130].

4.6.1 C_{60}/*h*-BN/Rh(111)

C_{60} powder (with purity of 99.9%) was sublimated from a Ti crucible onto *h*-BN on Rh(111) while keeping the surface at $\sim 370\,\mathrm{K}$. The LEED patterns of 1 ML C_{60} show an ordered $(2\sqrt{3} \times 2\sqrt{3})\mathrm{R}30^{\circ}$ structure (as seen often on metal surfaces) and the nanomesh superlattice spots as in Fig. 38(a) and (b). When this single C_{60} layer covers the entire nanomesh, the (12×12) Rh units periodicity of the nanomesh is retained and a hexagonally packed corrugated C_{60} layer, (in the fashion shown by LEED) results on the surface. The ordered C_{60} hexagonal overstructure can be seen in Fig. 38(c) and (d).

The mesh wires are decorated by lines of individual molecules, whereas either six or seven molecules can be distinguished inside the holes. In each nanomesh unit cell either 12 or 11 C_{60} molecules are found. The apparent height difference between the lowest C_{60} molecules, i.e. those in the centers of the mesh holes, and the other 6 C_{60} molecules in the holes is 0.7 Å, while it is 2 Å up to the molecules on the wires (even if within the wires locally small variations can be identified). The average lateral distance between the molecules is 9.4 ± 0.1 Å (Fig. 38(e)). In Fig. 38(f) a model of the arrangement of the C_{60} molecules along part of the line in Fig. 38(d) is shown, with the values measured with STM and a corrugation of 0.7 Å for the *h*-BN layer. In this way, if the C_{60} molecules would behave as spheres, the first which reach the surface would occupy the centers of the holes. Then the others would sit on the rims thus assuming a tilted position to get closer to the previous ones and this explains why they are imaged 0.7 Å higher. As last, the other molecules would sit between those in the rims of two neighboring unit cells, occupying the sites of the nanomesh wires but not contacting them. If this view of the C_{60} structure formation is correct, then it still needs to be explained why in the unit cells with 11 C_{60} molecules no C_{60} are found in the centers of the holes but all the others in the unit cell still occupy the same positions as those with 12 molecules. It might happen that the central molecule gets too pressed by the neighbors and in a second moment is expelled from the holes. Or it might be possible that the holes are not really empty but the molecules inside are sometimes seen as depressions by the STM at the scanning voltages used. Often some molecules within a C_{60} layer appear darker or brighter as has already been seen on various surfaces [128, 131]. The effect is assigned to C_{60} with different orientations and in distinct electronic states, thus creating a local work function change that gives a different apparent height in STM. In some cases the contrast is explained with the ordering-disordering state between the defect-like C_{60} molecule and the neighboring ones [129]. If even this is not the case and the hole centers are really empty, then the strong bond to the rims could be responsible for the molecular arrangement. Occasionally a fourth kind of molecule is found; two of them can be seen in Fig. 38(d). These brightest C_{60}, 0.7 ± 0.1 Å higher than those on

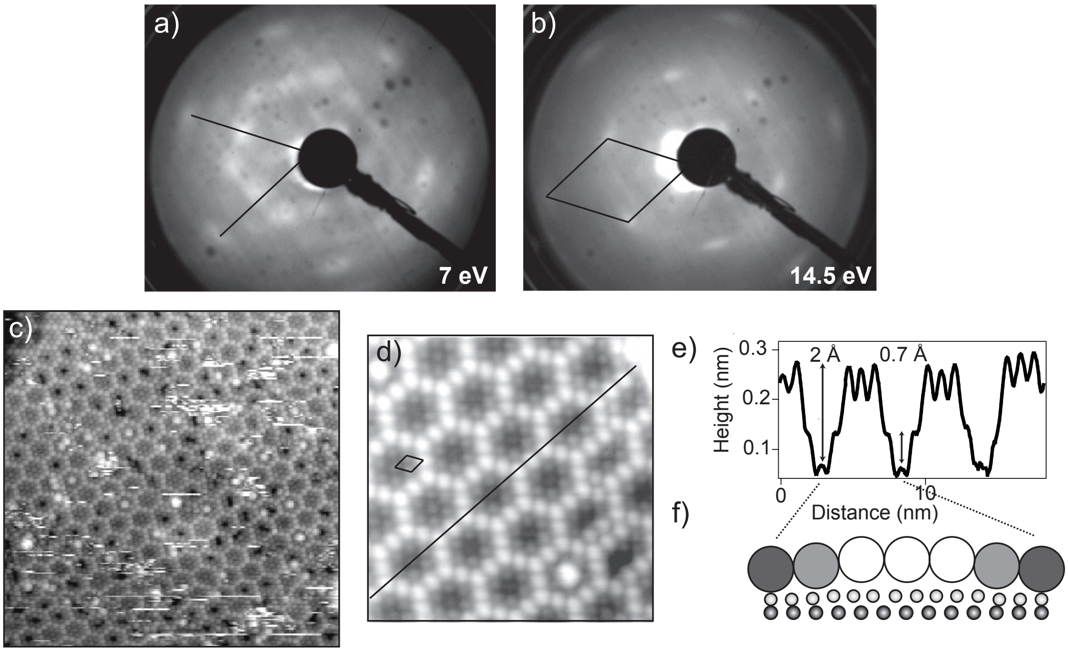

Figure 38: *(a-b) LEED patterns at 7 eV and 14.5 eV of 1 ML C_{60}/h-BN/Rh(111). The C_{60} forms a $(2\sqrt{3} \times 2\sqrt{3})$ R30° overstructure as indicated. The nanomesh superlattice spots can be seen around the (0, 0) Rh-principal lattice spot. (c) STM image of 1 ML C_{60}/h-BN/Rh(111) (47.5×47.5 nm^2, I_t=0.5 nA, V_s=2 V). (d) High resolution of the nanomesh area decorated by C_{60} molecules (15×15 nm^2, I_t=1.5 nA, V_s=-2 V). The unit cell found from the LEED is shown. Three kinds of individual molecules can be distinguished due to their height difference: the darkest ones at the center and bottom of the mesh, other 6 in the holes and the brightest ones in the position of the mesh wires. At two places large protrusions may represent additional corralled molecules. (e) Cross-sectional profile along the line in (d). The height difference between the lowest molecule and the others is indicated, taking heights and distances from the measured STM values. The distance between all the nearest neighbor C_{60} molecules is ∼9.4 Å. (f) Model of the atoms and molecules arranged in the portion of the profile as indicated. The smallest dark atoms are Rh, the light gray ones are N. On top of the N C_{60} molecules considered as spheres are drawn.*

the wires, occupy the positions on top of the dim molecules in the centers of the mesh holes and may represent corralled molecules with interesting zero-dimensional properties. Nevertheless, the growth of the C_{60} is driven by the nanomesh and its functionality as template is demonstrated. In fact not only the C_{60} layer is corrugated because of the height modulation of the mesh below, but the mesh also induces modifications in the molecule layer. In order to fit into the 3.2×3.2 nm *h*-BN supercell, it needs to be sterically compressed (the intramolecular distance of 9.4 ± 0.1 Å is $\sim 6\%$ smaller than the bulk value of 10.02 Å). If the STM would not show the real topography of the surface,

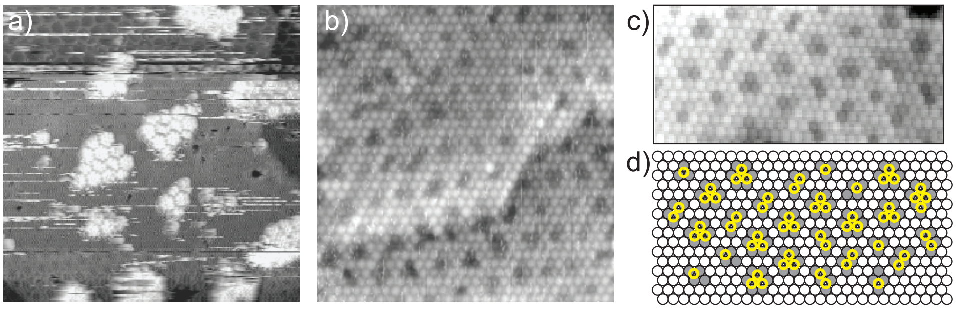

Figure 39: *(a) Submonolayer C_{60} on h-BN/Rh(111) (60×60 nm^2, I_t=0.5 nA, V_s=-1 V). The C_{60} aggregate in islands retaining the nanomesh periodicity. (b) Two terraces covered by 2 ML of C_{60} (26×26 nm^2, I_t=1 nA, V_s=1 V). (c) Small area where the arrangement of the molecules in the second layer is modeled in (d) (25×10 nm^2, I_t=1 nA, V_s=1.5 V). The single C_{60} layer below the one in (c) is shown in (d) where the dark circles are the first layer holes. If this layer is covered by spheres then one can reconstruct the geometry of the second layer whose holes are drawn as bright circles.*

the molecules with 10.02 Å diameter would sit not 2 Å but ∼ 6 Å higher on the wires. A compression of up to 20% has been observed for C_{60} on Au(001), where it is found that the charge density around the C_{60} molecule is deformed to an ellipsoid with uniaxial stress caused by the lattice mismatch with the substrate [132].

At submonolayer coverages the molecules aggregate in islands retaining the nanomesh periodicity as in Fig. 39(a). The islands seem not to have preferential sites for growing, and are found mainly in the terraces. The island height is ∼ 6 Å. At submonolayer coverages the molecules aggregate in islands retaining the nanomesh periodicity as in Fig. 39(a). The islands seem not to have preferential sites for growing, and are found mainly in the terraces. The island height is ∼ 6 Å. At longer exposures times, a second C_{60} layer grows in a layer-by-layer fashion, and it still presents a sort of periodicity driven by the first layer. It can be simulated with a hard sphere model, where the buckyballs fill the holes in the first layer as shown in Fig. 39(c) and (d). Different kinds of unit cells can be identified, due to the local irregularities on the first layer unit cells and probably also on the *h*-BN ones. The C_{60} can be removed from the surface with a short annealing at temperatures T ∼ 540 K, indicating that the layer is not strongly bonded on the *h*-BN film [123]. In the third C_{60} layer no periodicity induced by the one below is found. It is still unclear which sorts of interactions between the nanomesh and the C_{60} induce its molecular arrangement. The lock-in energy might be due to the *h*-BN units in the holes with a metal substrate-mediated interaction and to units on the rims where a polar-like bonding due to charge accumulation induced by the bending of the *h*-BN bonds can occur.

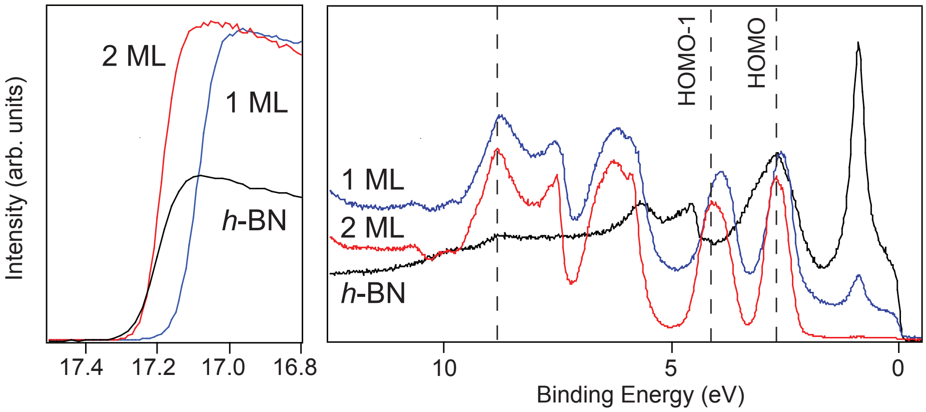

Figure 40: *He Iα normal emission UP spectra for bare h-BN/Rh(111) or covered by 1 ML C_{60} or 2 ML C_{60} as indicated. On the left a zoom on the region of the work function is displayed.*

The bonding between the C_{60} and the *h*-BN on Rh(111) has been investigated by UPS with He Iα as photoelectron excitation source. The characteristic peaks due to the C_{60} adsorption modify the appearance of the spectra of the bare *h*-BN on Rh(111) (Fig. 40). The formation of chemical bonds mainly influences the LUMO and the highest occupied molecular orbital (HOMO). Charge transfer to the C_{60} results in filling the LUMO. Since the unoccupied states are not accessible with direct UPS, attention has to be paid to the HOMO of C_{60} which is modified with respect to the cases of bulk-like C_{60} if the layer hybridizes with the substrate. For a single C_{60} layer the Rh bands are still visible, while they are completely suppressed when a second layer is added. The σ and the π bands due to the *h*-BN structure are buried below the C_{60} orbitals. The widths of valence states are a measure of the combined substrate/C_{60} and C_{60}/C_{60} bonding, together with vibrational effects. If the intramolecular distance is close to the van der Waals separation in bulk C_{60}, then the vibrational effects are not important and the broadening can be considered as a measure of the bond strength. For C_{60} on *h*-BN on Rh(111) the FWHM of the HOMO is 0.57 ± 0.05 eV similar for 1 ML and 2 ML coverages, close to the value of 0.5 eV for bulk C_{60} [133]. In strongly chemisorbed systems with covalent bonds between C_{60} and the substrate, values twice as much as this one have been found. For example in 1 ML C_{60}/Al(111) it is 1.2 eV [133], therefore, in this case the C_{60} is only weakly bonded. The position of the HOMO shifts by 93 ± 5 meV to higher binding energies from 1 ML to 2 ML, and the HOMO-1 shifts by 120 ± 5 meV in the same way. The HOMO binding energy for 1 ML is centered at 2.58 ± 0.05 eV and the HOMO-1 at 3.91 ± 0.05 eV, lower values than in the case of *h*-BN/Ni(111) [123] but still higher than typical values of 2 eV for the HOMO and 3.5 eV for the HOMO-1 [134]. The work function for 1 ML C_{60} is 4.25 eV, 100 meV higher than *h*-BN/Rh(111) but with the second C_{60} layer the work function decreases again to the value of the *h*-BN/Rh(111). If the C_{60} bands are plotted with respect to the vacuum level (E_v) instead than to E_f, then the HOMO peaks for 1 ML and 2 ML are aligned to the value of $6.83 \pm 0.05\,\text{eV}$, close to the HOMO ionization potential of $6.90 \pm 0.04\,\text{eV}$ found in [135]. In photoemission, the bands for conducting solids and chemisorbed monolayers are usually referred to a common Fermi level of the adsorbate and the substrate. Since the position of E_f varies with respect to E_v, such a referencing is valid only for systems in electrical contact with each other. Otherwise for weakly interacting (physisorbed) adsorbates the overlap between the wave functions of the substrate and the adsorbate is low enough that the screening charge is not capable to hop onto the adsorbate in the timescale of the ionization process. Such physisorption bonds are thus present for 1 ML and 2 ML C_{60} on *h*-BN on Rh(111).

4.7 Nanomesh formation

The mechanism of self-assembly of the nanomesh involving around 400 atoms per unit cell, is an intriguing aspect that is not understood yet. Preliminary tests on the nanomesh formation under different conditions have been performed mainly changing two parameters: the borazine vapor pressure during exposure and the growth temperature. At low values for the borazine exposure ($< 1\ L$) it has been possible to 'freeze' the system during its growth process. In Fig. 41 'a snapshot' of the nanomesh formation is shown. In the image three regions can be distinguished: in the top part a bare Rh area with small irregular units (may be *h*-BN), in the middle a disordered area where broken nanomesh wires start to join together and in the bottom part an ordered island is formed. It is not clear if at higher exposures the mesh grows carpet-like above steps or has different nucleations points and then the different islands formed join together. Moreover it is not even known if the *h*-BN units grow intact on the surface or BN fragments or broken hexagons are involved during the self-assembly process, as found in the formation of *h*-BN islands on Ni(111) [136]. At exposures lower than the saturation value the UPS normal emission

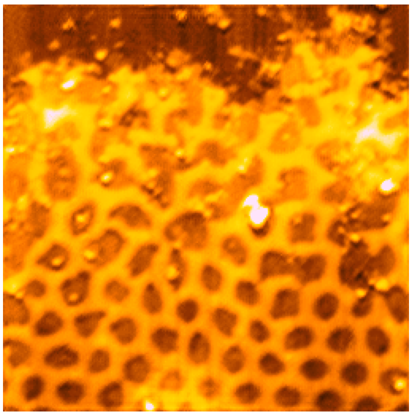

Figure 41: *STM image of a Rh(111) surface that was exposed to 1 L of borazine. It shows a boundary region of a nanomesh in which one can see the transition from an uncovered Rh surface and a regular nanomesh structure behind a transition state. Considering that the film was grown at 1070 K where the BN units are very mobile, this RT image shows a frozen snapshot of the self-assembly process.*

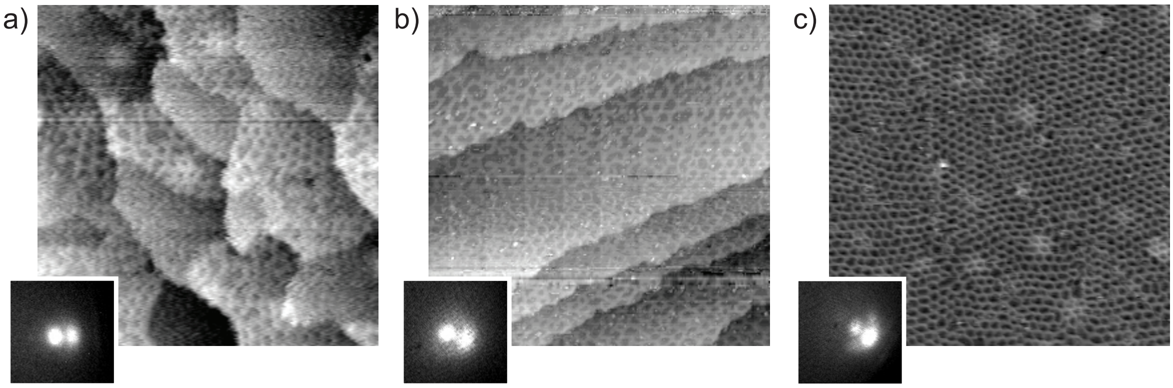

Figure 42: *STM and corresponding LEED images of the nanomesh grown at different temperatures. In the insets the LEED patterns show mainly the principal Rh spot (0,-1) and the h-BN one. In all the cases 40 L of borazine were used. In (a) the clean sample was at RT during exposure and then annealed to 1050 K (STM image 75×75 nm^2 recorded at I_t=3 nA and V_s=-1 V; LEED measured at 61 eV). The STM image is not sharp due to an external frequency during scanning. In (b) the sample was at 740 K (STM image 100×100 nm^2 recorded at I_t=2 nA and V_s=-2 V; LEED measured at 70 eV). In (c) the temperature was 900 K (STM image 100×100 nm^2 recorded at I_t=0.4 nA and V_s=-2 V; LEED measured at 70 eV). In this image the tip contrast particularly enhances the wires.*

spectra do not show the σ and π bands, but the presence of the *h*-BN on the surface can be recognized by the double cutoff in the secondary edge in the spectra. One belongs to the Rh substrate and one (shifted by 330 meV) is due to the overlayer. The nanomesh can form also at different temperatures even if the best order results from the preparation at $\sim$ 1050 K and 40 L of exposure to $(HBNH)_3$. A clean Rh(111) surface kept at room temperature was exposed to 40 L of borazine. In the LEED patterns, besides some faint Rh principal lattice spots, a lot of background was present but no other spots appeared. The sample was annealed and the evolution of the structure was checked by LEED. At 675 K the principal spots of the *h*-BN lattice showed up and they became sharp once a temperature of 1050 K was reached (inset in Fig. 42(a)). STM images showed small terraces covered with the nanomesh as in Fig. 42(a). If the sample was at 740 K during borazine deposition, then a disordered mesh could form on the surface, with unit cells characterized by distorted shapes (as in Fig. 42(b)). A sample temperature of 900 K during exposure was not yet enough to get a regular nanomesh even if in the LEED weak superlattice spots could be found at different energies. These simple experiments demonstrate that a high temperature during the formation process is necessary to get the most ordered structure and the most energetically stable configuration of the nanomesh.

5 Is the nanomesh unique?

After the discovery of the nanomesh, the question arised whether Rh(111) was the only surface where this peculiar *h*-BN structure forms or if it can be grown also on other substrates. Since one of the major factors for the mesh formation is the lattice mismatch of boron nitride and the metal underneath, the choice of substrate could allow to tailor the mesh hole size. One of the first candidates chosen as alternative nanomesh support is the Ru(0001) surface [137]. Rhodium and ruthenium are near neighbors in the periodic table and therefore share similar physical and chemical properties. The hexagonal Rh(111) and Ru(0001) surfaces are almost identical with 2.69 Å and 2.70 Å corresponding in-plane lattice constants. As a consequence also the tensile lattice mismatch with *h*-BN is almost the same: $\sim -6.8\%$ and $\sim -7.3\%$. A major difference is in their bulk structure: Rh is an *fcc* crystal while Ru is *hcp*. Therefore for the Rh the stacking of the atomic planes in the direction orthogonal to the [111] orders in an ABCABC fashion, while for the Ru along the [0001] is ABAB. The first structural difference then comes only in the third layer below the surface. While a perfect *hcp* (0001) surface has threefold symmetry as a *fcc* (111) surface, the diffraction patterns commonly obtained are sixfold symmetric. This apparent change in symmetry is due to the presence of steps. In fact the different stacking on adjacent terraces, with termination ...ABAB and ...BABA, respectively, results in the rotation by 60° of the surface atomic layers. Diffraction from neighboring terraces yields threefold patterns that are rotated by 60° with respect to each other.

5.1 *h*-BN on Ru(0001)

The experiments were performed on two Ru(0001) single crystals and on 150 nm thick Ru(0001) films grown on $Al_2O_3(0001)$. The crystals were most efficiently cleaned by repeated cycles of Ar^+ ion sputtering at high temperatures $\sim 950\,K$ (10 to 30 min, acceleration voltage of 1 to 1.5 keV and sputtering current of ~ 2 to $3\,\mu A/cm^2$) and exposure to 20 L of O_2 at 950 K with subsequent annealing to 1120 K. The films were cleaned in the same way as the Rh(111)/$AlO_2(0001)$ ones as indicated in section 4.1. The *h*-BN layers were produced as for the Rh, by exposing the clean Ru surface to 41 L of $(HBNH)_3$ while keeping the surface at 1050 K, followed by 1 min of post-annealing at the same temperature. The cleanliness of the Ru(0001) samples was judged by the sharpness of the spots on the LEED patterns and by the value of the work function measured with UPS. Here for a clean sample it is measured as $5.44 \pm 0.1\,eV$, in good agreement with the value of 5.4 eV from [138] and 5.52 eV from [139]. Due to the overlapping of the C 1*s* peak with the Ru 3*d* peaks, it is not possible to estimate the carbon contamination with

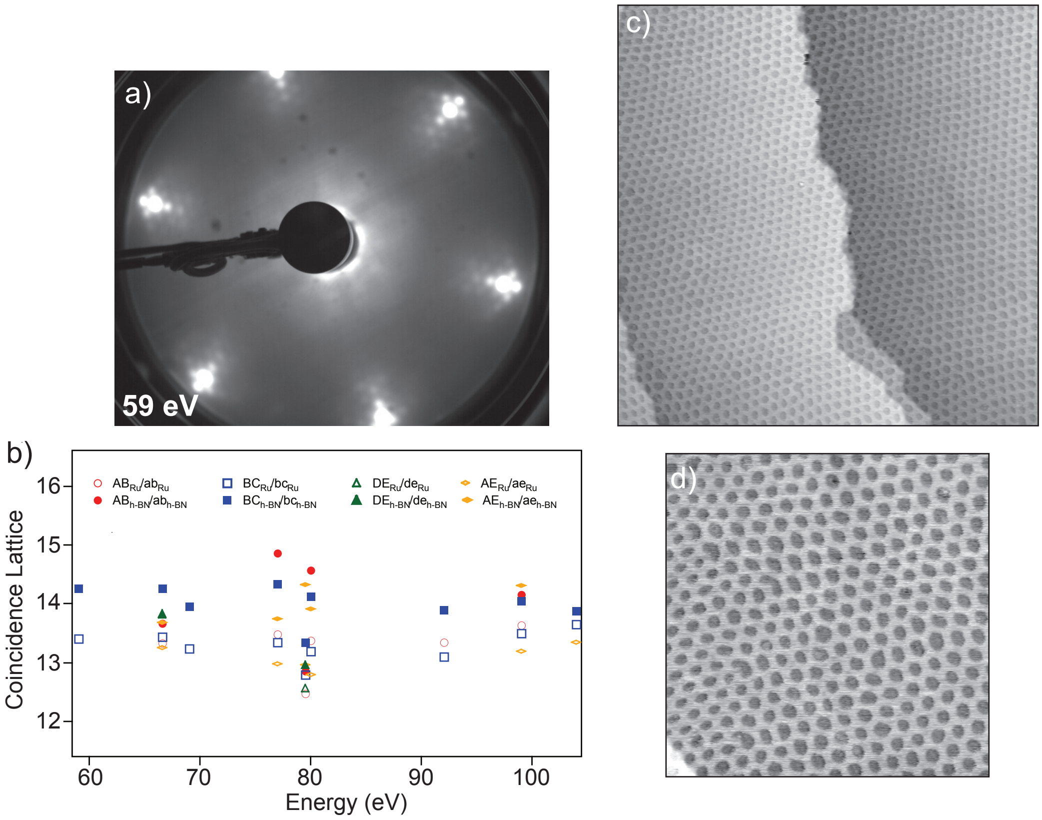

Figure 43: *(a) LEED pattern of h-BN on Ru(0001) measured at 59 eV. In (b) the values for the h-BN coincidence lattice on Ru are plotted. The same analysis described for Fig. 14 is done here, and the same terminology is used. The opened symbols correspond to the ratios between the two h-BN principal lattice spots and two overstructure spots in the same line profile, while for the closed the Ru-Ru lattice spots distance is considered. The points correspond to different series of measurements on different samples. (c) Constant current STM image (120×120 nm^2 I_t=1 nA, V_s=-1 V) of h-BN on Ru(0001), a smaller area is shown on the other STM image in (d) (50×50 nm^2 I_t=1 nA, V_s=-1 V). Clearly a nanomesh forms on this surface but many distorted unit cells are found in the mesh that appears therefore less ordered than in the case of the one grown on Rh(111).*

XPS, nevertheless its presence is easily identified with STM as will be explained later. LEED patterns of the *h*-BN on Ru(0001), as in Fig. 43(a), show the hexagonal spots of the *h*-BN superstructure arranged as in the case of the *h*-BN on Rh(111). A similar analysis for the periodicity has been done as the one already described for the Rh case in the section 4.2. The result is shown in Fig. 43(b) where different *h*-BN/Ru(0001) preparations are compared. The estimate for the *h*-BN coincidence lattice is (13.23×13.23)±0.34 Ru in plane lattice distances and (14.0 × 14.0) ± 0.5 *h*-BN units. Therefore from this

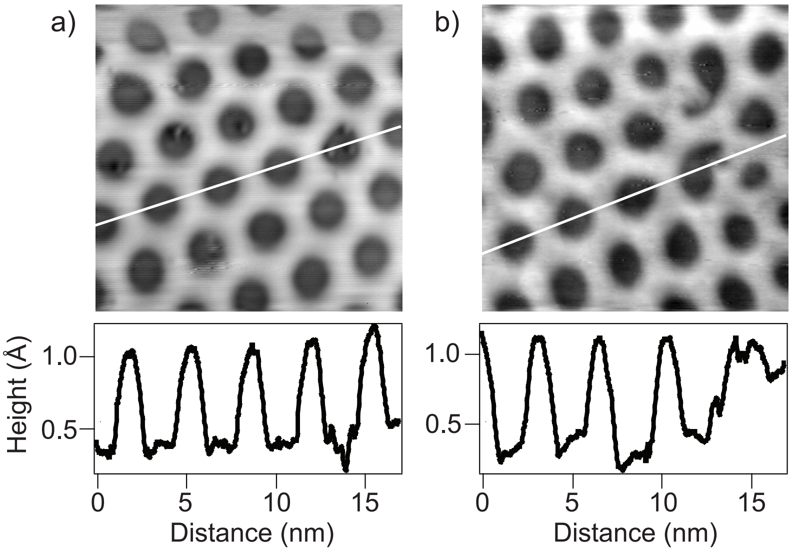

Figure 44: *Constant current STM images (13×13 nm^2) of h-BN on Rh(111) in (a) and of h-BN on Ru(0001) in (b) both measured at I_t=1 nA, V_s=-2 V. The cross-sectional profiles correspond to the white lines on the pictures above them. Two 'bean-like' shaped distorted mesh unit cells can be seen in (b).*

analysis the BN-superstructure should arise from (14 × 14) *h*-BN units on (13 × 13) Ru lattice unit cells, which would correspond in real space to 3.5 nm. This value is higher than the one given in LEED studies on *h*-BN on Ru(0001) published in the past [81]. *Paffet et al.* found that the *h*-BN overstructure was growing on (12×12) Ru lattice units. The lack of STM and UPS data led them to propose a simple *h*-BN coincidence lattice forming on the surface, while no mesh-like arrangement was introduced. STM images clearly show that the nanomesh on Rh(111) is not unique: it forms also on the Ru(0001) surface. An example is shown in Fig. 43(c) where the nanomesh covers homogeneously all the Ru terraces. A smaller image taken in a portion of the lower terrace of Fig. 43(c) is shown in Fig. 43(d). As compared to the nanomesh on Rh(111), measured in the same tunneling conditions, the two are identical. In Fig. 44 cross-sectional profiles were taken along a similar number of mesh unit cells on the two surfaces. The same corrugation of 0.7 ± 0.2 Å, wire thickness of 1.2 nm and hole size of 2 nm are derived. Nevertheless, the long range ordering between the two nanomeshes is different: while on Rh the nanomesh grows regular on many terraces and the deviation from a perfect hexagonal network is mainly due to the Ar$^+$ bubbles, the mesh on Ru appears often with distorted units, and several kinds of defects can be identified. Among these single deformed units with a 'bean-like' shape arising from the fusion of two nanomesh holes and domain boundaries that separate different mesh areas terminating with broken unit

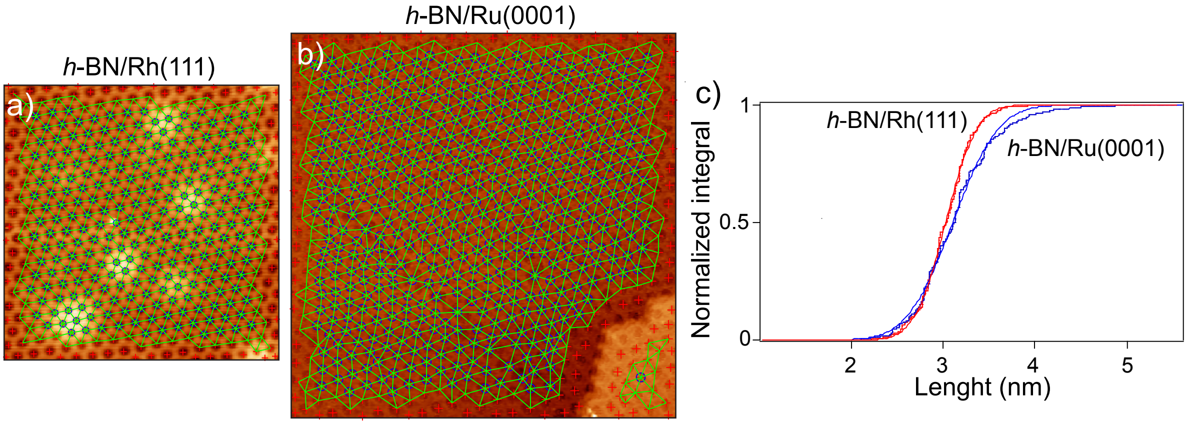

Figure 45: *Constant current STM images of h-BN on Rh(111) in (a) (50×50 nm^2, I_t=1.8 nA, V_s=-2 V) and of h-BN on Ru(0001) in (b) (70×70 nm^2, I_t=1 nA, V_s=1 V). The green network connects each hole center (blue circles) with the nearest neighbor. The units at the borders and around the steps were excluded. The bright spots in (a) are Ar$^+$ bubbles. A domain boundary runs across the large terrace in (b) (from top left to bottom right). In (c), the normalized cumulative distribution of the nearest neighbor distances is plotted. The measured data were fitted with the cumulative distribution function, displayed with a thin line, as presented in Eq. 24.*

cells are found. In order to quantify the degree of ordering of one system with respect to the other, several STM pictures of typical nanomeshes grown on two Rh(111) and two Ru(0001) single crystals have been analyzed. The degree of order is defined from the distribution of all the distances between the nanomesh hole centers and by the number of defects. The mesh hole centers were found in each image using the 'Watershed' transform. This procedure is suitable for the images of the nanomesh since it is able to identify the holes from their surrounding ridges. The center of each mesh hole was defined as the mass point of the corresponding region. To find the nearest neighbors for each center point, the 'Delaunay' triangulation algorithm on the set of detected centers was applied. The statistical distribution of the distances between the nearest neighbor centers was gathered and the neighbors at the borders of the image, where incomplete units are found, were not considered. The units close to the steps have not been taken into account as well since it is not clear how the mesh grows across steps. Similarly, the number of nearest neighbor unit cells is found by discarding the cells at the boundary and at the steps. In Fig. 45(a) and (b) two images are shown as outcome of this analysis. The green network joins the nearest-neighbor centers indicated by the blue circles. In Fig. 45(c) the normalized distribution of the lengths, found from several STM images of different areas, is shown. In particular, statistical data from approximately 17.000 and 21.000 distances were obtained for the *h*-BN/Rh(111) and for the *h*-BN/Ru(0001), respectively. The distribution curves have been fitted with the Cumulative Distribution Function which calculates the probability of finding a distance (d) with a value equal or less then mean value (d_0), it is defined as:

$$F(d, d_0, \sigma) = \frac{1}{\sigma\sqrt{2\pi}} \int\limits_{-\infty}^{d} \exp\left(-\frac{(x-d_0)^2}{2\sigma^2}\right) dx = \frac{1}{2}\left[1 + erf\left(\frac{x-d_0}{\sigma\sqrt{2}}\right)\right] \tag{24}$$

where σ is the standard deviation and *erf* is the Error Function. From this fit the mean value for the distances of *h*-BN/Rh(111) and of *h*-BN/Ru(0001) were found as $3.02 \pm 0.27\,\mathrm{nm}$ and $3.10 \pm 0.39\,\mathrm{nm}$ respectively. These numbers are smaller than those detected just from line profiles measured along the fast-scanning direction (3.2 nm). This is due to the averaging of the lengths on all the directions on the surface plane, but since the STM scanning is not homogeneous then the images are slightly distorted. The error bar given in the mean values is the standard deviation calculated from Eq. 24. This quantity indicates that the distances between the nanomesh holes on Ru vary by 44% more than on the Rh, clearly suggesting that the Rh-nanomesh is more regular than the Ru one. Concerning the number of nearest neighbors, this value can vary from the expected 6 to 4, 5, 7, and 8. This is due to the distorted mesh units, to the broken unit cells and to the presence of domain boundaries. For the Rh approximately 4700 centers and for the Ru around 5500 centers were analyzed. For the case of Rh, only 1.1% of the unit cell centers were not surrounded by 6 nearest neighbors, while this number is 12.9% for the Ru where often 5 or 7 surrounding centers were found.

The analysis of these STM images leads also to the conclusion that on the Ru(0001) surface the coincidence lattice is due to (13 × 13) *h*-BN units on (12 × 12) Ru lattice spacing, in contrast to the results from the analysis of the LEED patterns. SXRD experiments could lead to a solution for this inconsistency.

Recently *Blaha et al.* have calculated the binding energy of *h*-BN on different transition metals surfaces [104]. The calculations were done on a 7-layers slab of metal atoms covered on both sides by *h*-BN in a (1×1) geometry with N on top sites and B on *fcc* ones. The standard 'Generalized Gradient Approximation' (GGA) in the form proposed by Perdew, Burke and Ernzerhof (known as PBE) was used. Weak bonding is found in general on noble metals, but it is strong on Ru(0001) and on Rh(111). For the first a value of $\sim 0.6\,\mathrm{eV}$ per BN unit is found, while for the second it is $\sim 0.3\,\mathrm{eV}$. The stronger bonding of *h*-BN units on the Ru surface can be responsible for the poorer nanomesh ordering. In fact in the regions of strong bond (i.e. in the holes) the BN units can be 'fixed' so strongly to the substrate that it is more favorable for the system to break the mesh wires than move the atoms away from the nearly commensurate regions during the growth process. On the Rh, since the bonding is less strong, the mesh is still able to

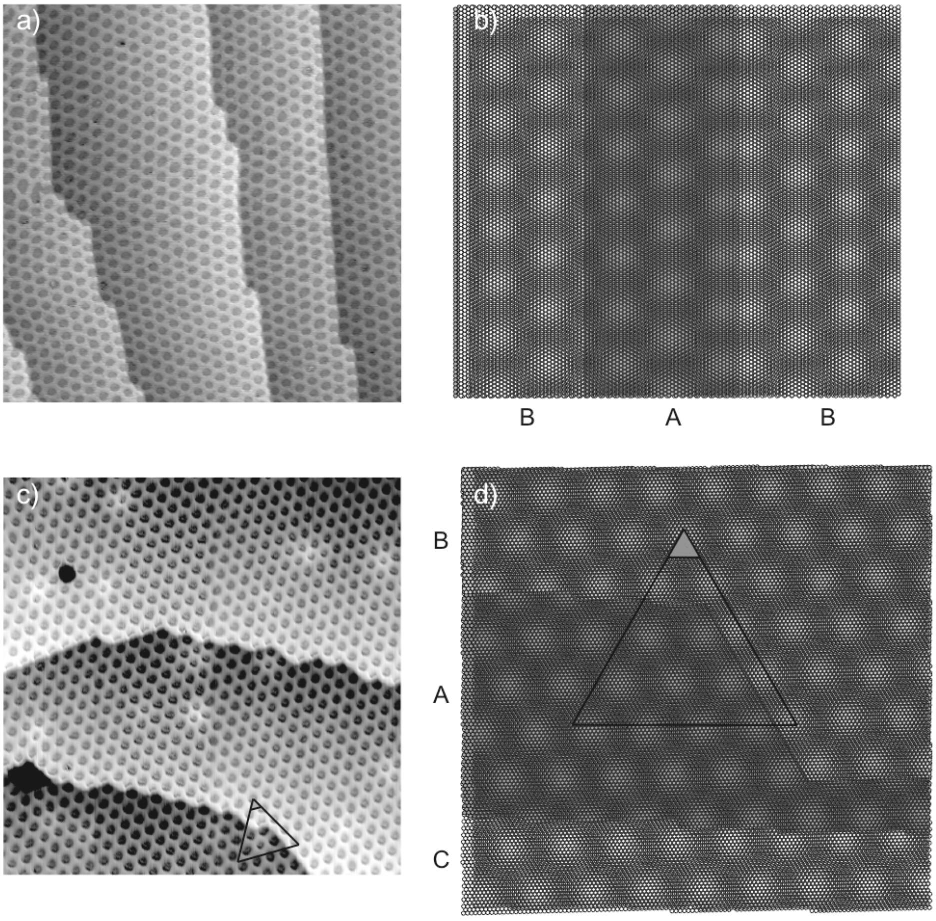

Figure 46: *Constant current STM images of h-BN on Ru(0001) in (a) (80×80 nm^2, I_t=1 nA, V_s=-1 V) and of h-BN on Rh(111) in (c) (80×80 nm^2, I_t=2.5 nA, V_s=-1 V). In (b) and (d) atomistic models are shown of the nanomesh arrangement on the different terraces of (a) and (c) respectively. A layer of N atoms is plotted against the substrate terraces and the Moiré contrast is due to N on top sites in the bright areas (i.e. nanomesh holes).*

accommodate to the substrate keeping its structure intact. On the other hand also the different relaxation of the Ru(0001) and Rh(111) surfaces and the different residual stress during the nanomesh growth at high temperatures 1050 K can influence the *h*-BN growth. The mesh on Ru can be pictured as a rigid network that favors short range atomic order, while on the Rh the mesh is soft and capable to maintain the long range order. The nanomesh discriminates the crystal structure of the Rh and Ru substrates, this can be seen in the STM images of the steps. In Fig. 46(a) five different Ru(0001) terraces are covered with *h*-BN. The nanomesh layer at the step edges can terminate either with closed unit cells or with open units that are completed in the terrace just below the step. Then if the nanomesh film on a terrace finishes with a closed unit, on the lower one it ends with opened units and continues in an alternating fashion on the next ones. This can be modeled by superimposing N (or B) atomic layers on the Ru(0001) A-type or B-type terraces. In Fig. 46(b) a model is shown to explain the step arrangement in Fig. 46(a): a single N (or B) atomic layer is plotted on three different Ru(0001) terraces with B-A-B stacking as indicated. A hexagonal Moiré pattern is generated where the brightest contrast is given by the regions where the N atoms occupy on top Ru sites, therefore corresponding to the holes, while the darkest area are due to the nitrogens on bridge and hollow sites, giving the contrast of the wires. The N atoms prefer to bind on top sites near the A-type $\{11\bar{1}\}$ microfacets (where half mesh hole is seen) while on the $\{100\}$, the B-type ones, the other adsorption sites is favored (or induced).

In Fig. 46(c) three different Rh(111) terraces covered by *h*-BN can be seen. The nanomesh holes change registry from terrace to terrace: they follow the same line in the highest and lowest terrace but they are shifted by half a mesh unit cell in the middle one (as shown by the left side of the triangle plotted on Fig. 46(c)). A-B-C- types of steps are needed to model the structure as expected for this *fcc* crystal. In Fig. 46(d) the horizontal steps end with $\{100\}$ microfacets and $\{11\bar{1}\}$ on the kinks, while the diagonal step terminates with $\{11\bar{1}\}$ microfacets. The triangle is drawn to identify the corresponding areas in the STM image and in the simulation.

5.2 The electronic structure of *h*-BN on Ru(0001)

The normal emission UP spectra measured with 21.22 eV photon energy for the clean Ru(0001) and the *h*-BN covered surface are shown in Fig. 47 together with the spectrum of *h*-BN on Rh(111). All the *h*-BN related bands (σ_α, σ_β, π_α, π_β) found in the case of Rh, are present also when the Ru(0001) surface is covered by *h*-BN. They lie at binding energies: $E_B(\sigma_\alpha) = 4.97 \pm 0.08\,\mathrm{eV}$, $E_B(\sigma_\beta) = 5.91 \pm 0.15\,\mathrm{eV}$, $E_B(\pi_\alpha) = 9.00 \pm 0.08\,\mathrm{eV}$ and $E_B(\pi_\beta) = 9.83 \pm 0.10\,\mathrm{eV}$. They appear at slightly different energies than on *h*-BN/Rh(111), and this energy shift can be due to the different work functions of the two systems ($\Phi_{h-BN/Rh}= 4.15 \pm 0.10\,\mathrm{eV}$ and $\Phi_{h-BN/Ru}= 4.0 \pm 0.1\,\mathrm{eV}$) and to a slightly different bond strength of *h*-BN to Ru or Rh. The σ_β band compared to the σ_α has a weight of $69 \pm 1\%$, similar to the Rh nanomesh.

The nature of the features labeled *A* and *A'* in Fig. 47 is investigated with ARUPS. In Fig. 48(a) and (c) the valence band dispersion of the clean Ru(0001) surface is shown. The boundaries of the first SBZ of Ru(0001) are at $\overline{\Gamma\mathrm{M}} = 1.34\,\text{Å}^{-1}$ and at $\overline{\Gamma\mathrm{K}} = 1.54\,\text{Å}^{-1}$. The electronic structure of Ru has already been measured several times in the past mainly along the [0001] direction [140] but also along $\overline{\Gamma\mathrm{M}}$ and $\overline{\Gamma\mathrm{K}}$ [141] and theoretical studies can be found as well [114]. In the work presented in reference [141], the experiments

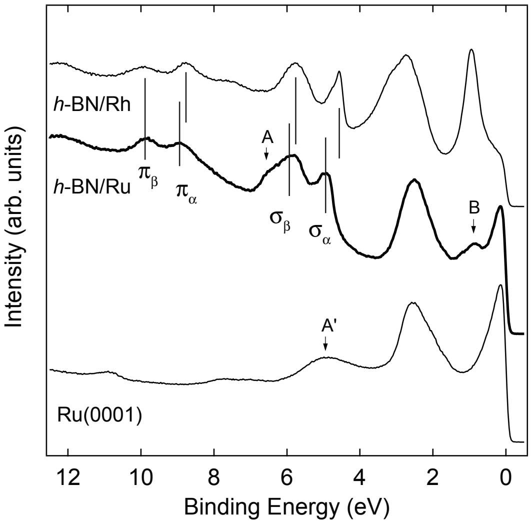

Figure 47: *He Iα normal emission UP spectra for Ru(0001), h-BN/Ru(0001) and h-BN/Rh(111). The h-BN related bands* σ_α, σ_β, π_α, π_β *found for the Rh case, are also present for h-BN/Ru(0001). The letters A and A' indicate bands related to the Ru. The area ratio* $\sigma_\beta/\sigma_\alpha = 2.19 \pm 0.14$ *is calculated from the analysis of 9 UPS spectra belonging to different h-BN preparations.*

were performed with synchrotron radiation with photon energies from 15 to 45 eV. The binding energy values are given with respect to the Fermi level. At $\overline{\Gamma}$ several states can be measured: the state found at a binding energy ~ 0.5 eV is attributed to the topmost *d*–like band, the one at ~ 2.0 eV is due to the lower *d*–like bands and the upper flat *sp*–like band. The one around 5 eV is a surface state. At higher photon energies (hν ~ 40 eV) two other states are found at 5.3 eV and 7.3 eV. The UP spectra measured here agree well with those data. In particular three states are visible at $\overline{\Gamma}$: the most intense one is at the Fermi level and disappears at 1 eV, the second is at 2.50 ± 0.10 eV and the last one at 5.15 ± 0.10 eV (labeled A' in Fig. 47). Theoretically, two surface states degenerate at $\overline{\Gamma}$ are also predicted at 1.5 eV and two in the higher gap at $\overline{\mathrm{K}}$ at an energy around 1.8 eV. The last two were detected at 20 eV photon energy in [141], but none of these surface states are observed in the data presented here. When the Ru(0001) is covered with *h*-BN, the Ru bands get attenuated and besides the pairs of σ and π states, a new state appears at $\overline{\Gamma}$ at 0.85 ± 0.10 eV. It is labeled B in Fig. 47. This state can be found on the bare and on the *h*-BN covered surface at $k_{||} = 0.15$ Å at ~ 0.76 eV. Therefore it is not a pure new *h*-BN feature but it gets enhanced when *h*-BN is adsorbed. The higher binding energy sigma band (σ_β) is close to a Ru state (indicated with A in Fig. 47), probably the surface state (A' in Fig. 47) that due to the overlayer shifts to a much higher binding energy (~ 6.5 eV). The positions of the *h*-BN related bands that can be found from these measurements are: $E_{\overline{\mathrm{K}}}(\pi_\alpha) = 3.4\,\mathrm{eV}$, $E_{\overline{\mathrm{K}}}(\pi_\beta) = 5.2\,\mathrm{eV}$, $E_{\overline{\mathrm{M}}}(\pi_\alpha) = 4.25\,\mathrm{eV}$, $E_{\overline{\mathrm{M}}}(\sigma_{\alpha 1}) = 7.95\,\mathrm{eV}$. The associated band widths are then: $\Delta E_{\overline{\Gamma\mathrm{K}}}(\pi_\alpha) = 5.6\,\mathrm{eV}$ and $\Delta E_{\overline{\Gamma\mathrm{K}}}(\pi_\beta) = 4.63\,\mathrm{eV}$ similar to those for the Rh nanomesh. The *h*-BN bands have been measured with higher energy and angular resolution as done for the *h*-BN on Rh(111). The dispersion plots are shown in Fig. 49 and can be compared with those in Fig. 29. Also in this case several bands appear, but they are less sharp than in the Rh, perhaps

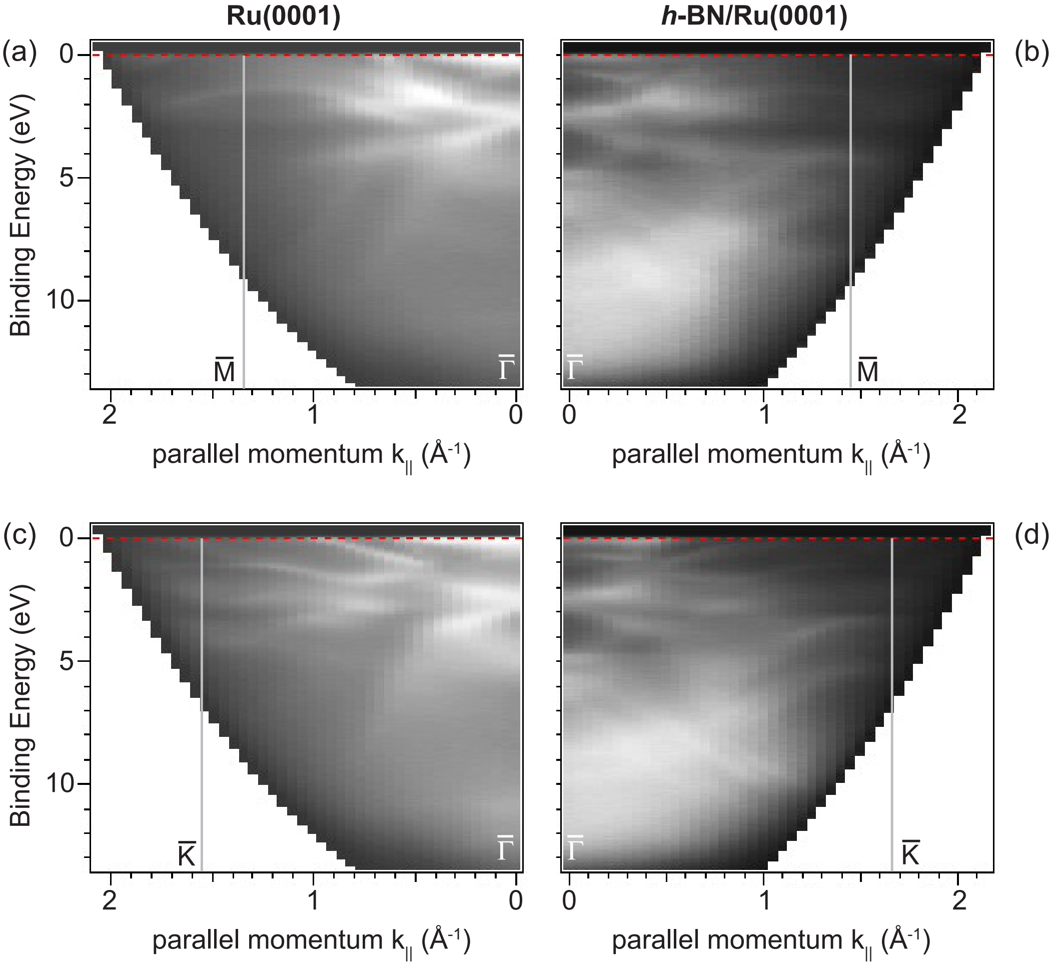

Figure 48: *Angle resolved He Iα dispersion plot for clean Ru(0001) surface ((a) and (c)) and h-BN/Ru(0001) ((b) and (d)) along the azimuths* $\overline{\Gamma M}$ *and* $\overline{\Gamma K}$ *respectively. The data are plotted with respect to the Fermi level. The* $\overline{\Gamma}$, $\overline{M}$, $\overline{K}$ *points in the first SBZ are indicated.*

due to the overlap of some Ru bands in this energy region (especially along the $\overline{\Gamma\mathrm{M}}$ direction). The same band assignment can be done. Two constant-energy maps have been measured, one at a biding energy of 6.81 eV, that corresponds to a cut which includes the π bands, and one at 10.04 eV, mainly around the σ bands. In the energy map measured at 6.81 eV, quite surprisingly, the brightest feature appearing is due to the π_δ band. It is found at a parallel momentum $\mathrm{k}_{||}(\pi_\delta)$=1.03 $\mathrm{Å}^{-1}$ along $\overline{\Gamma\mathrm{K}}$. In this direction besides π_δ all the other π bands are less intense, especially the σ bands. The energy map measured at 10.04 eV can be directly compared to the one of *h*-BN on Rh(111) in Fig. 31(a). The same features explained already in section 4.4.2 can be identified. Anyway, on Ru the central hexagon is not as sharp as for Rh and the 6 bright spots that surround it in the $\overline{\Gamma\mathrm{K}}$ direction are very faint. This observation suggests that for the highly ordered Rh

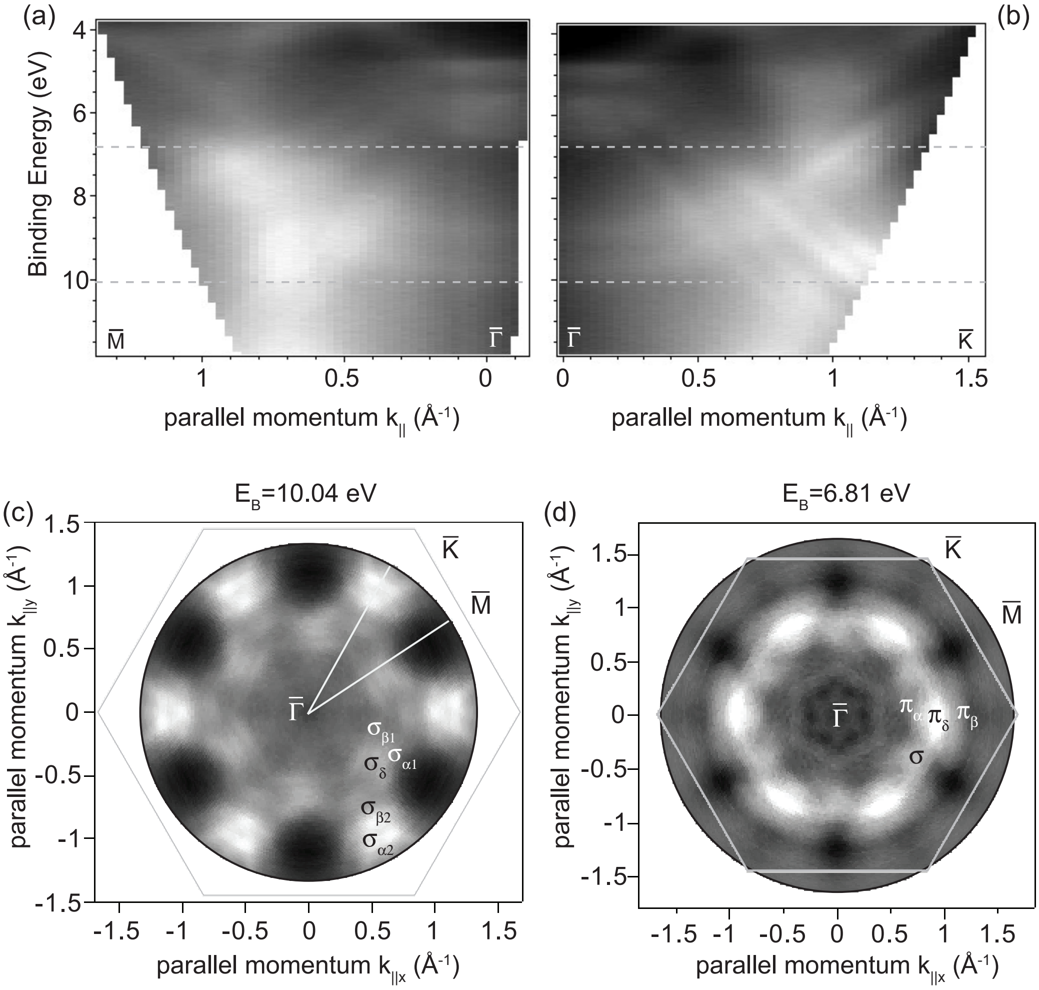

Figure 49: *High resolution angle resolved He Iα dispersion plot for h-BN/Ru(0001) along the azimuths* $\overline{\Gamma M}$ *(a) and* $\overline{\Gamma K}$ *(b). In (c) an energy map measured in the region of the σ bands at* E_b*=10.04 eV as indicated by the lower energy dashed line in (a) and (b). This map can be directly compared to the one in Fig. 31(a) since the difference in the binding energy compensates for the work function shift between the two systems. In (d) an energy map measured in the region of the π bands.*

nanomesh they can be really due to the mesh periodicity appearing in the first SBZ. Since in Ru this periodicity is often lost due to the defects, such *umklapp* processes are less favored. On the other hand, the variety of differently bonded N and B species in the nanomesh on the two metals is so large that the outcome of the photoemission processes is not easy to predict and this makes it difficult to interpret these data.

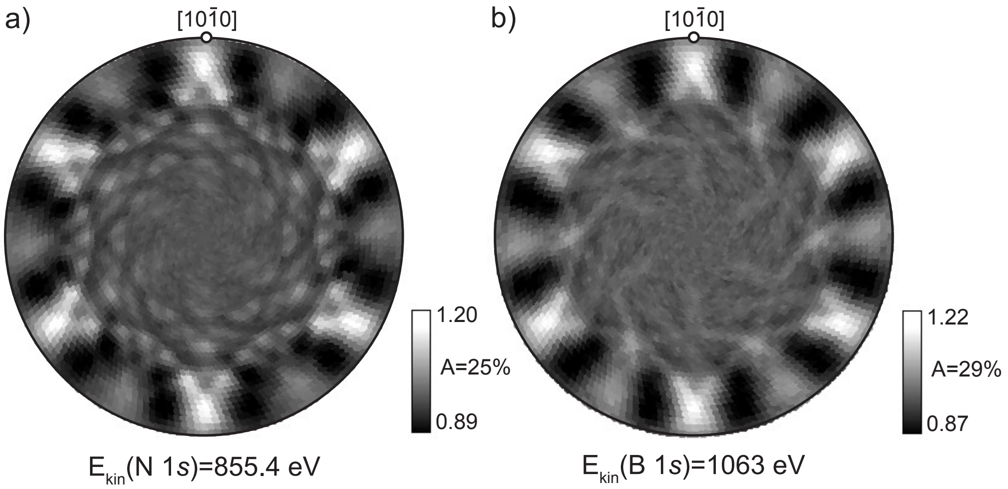

Figure 50: *XPD patterns for h-BN on Ru(0001). (a) N 1s pattern measured at 855.4 eV, (b) B 1s pattern measured at 1063 eV. The patterns are shown in stereographic projection and are azimuthally averaged.*

5.3 Atomic order in the Ru-nanomesh

XPD patterns for the N 1s and B 1s emitters have also been measured for the *h*-BN on Ru(0001) (Fig. 50). Even if the anisotropies in these measurements are lower than for those of *h*-BN on Rh(111) (see Fig. 32) and on Ni(111) (see Fig. 33), extremely sharp features can be identified. Several interference fringes are found around the maxima at grazing emission and intense peaks are produced whenever the interference cones cross each other. The patterns are six-fold symmetric. This is due to the Ru crystal structure. In the ABAB stacking of the atomic layers, the *hcp* sites are rotated by 60° in two subsequent planes. Therefore an emitting adatom occupying *hcp* sites on an A-type and one on a B-type terrace will produce two patterns rotated by 60° one with respect to the other. Since the final pattern is an average of them, a six-fold symmetry is obtained. The high coherence seen in these XPD patterns is certainly produced by a great order at the atomic level around the emitting atom. This seems to contradict the STM data where the long range order is lower than in the Rh case. The XPD patterns measured for the N 1s and B 1s on the Ru-nanomesh represent higher coherence than those belonging to the Rh-nanomesh. Nevertheless a quantitative discrimination between the order appearing in the different XPD patterns is not addressed here. In fact the quality of the crystals used for these experiments could favor the overall ordering of one system over the other (for example due a larger terrace size).

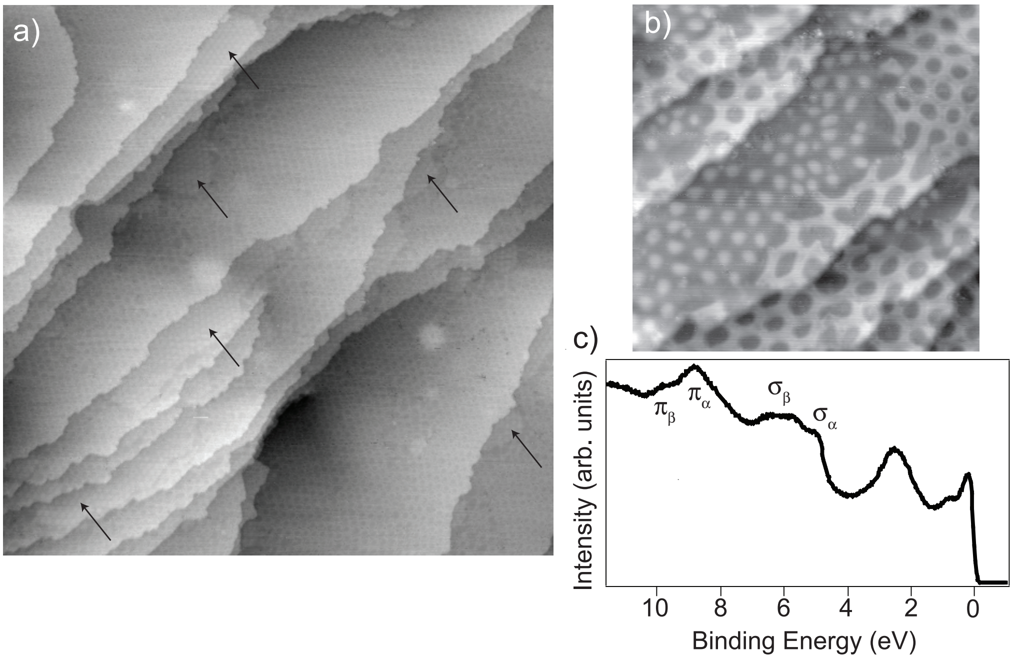

Figure 51: *Constant current STM images of coexisting nanomesh and graphite on Ru(0001). In the large scale image (a) several terraces covered with h-BN are shown (200×200 nm^2, I_t=1 nA, V_s=1 V). The arrows point on some island containing the graphite Moiré layer. In (b) the two structures can be distinguished (40×40 nm^2, I_t=1 nA, V_s=-2 V). (c) is the UP spectrum measured for the h-BN/Ru(0001) in (a) and (b). The σ and π bands of the nanomesh are indicated.*

5.4 Nanomesh and Nanodots

In the data presented so far it has always been assumed that the crystals were free from contaminants. The difficulty in the identification of carbon species on the surface from XPS could still bring us to the conclusion that the lower ordering on the Ru is locally due to undetected adsorbates (such as C) on the surface. STM turned out to be a suitable tool to define the cleanliness of the surface and the purity of the nanomesh structure thus allowing to discard unsuccessful sample preparations. It is known since many years that the annealing at high temperatures of a Ru(0001) surface can lead to the formation of graphite layers on the surface due to the diffusion of carbon atoms from the bulk [142]. LEED patterns at 800 K were showing a hexagonal coincidence lattice (similar to the one of the nanomesh) [142]. At 1300 K the sharp spots were due to the arrangement of (12×12) C-units on (11×11) Ru-unit cells. In STM images a Moiré pattern was recognized. This appeared on the surface as an array of small islands arranged in a hexagonal fashion with a periodicity of $(30 \times 30) \pm 0.3$ Å. Such a structure is also seen to coexists with the nanomesh for samples that did not undergo many cycles of sputtering, oxidation and annealing. In Fig. 51(a) a large area of the Ru surface with several terraces covered with *h*-BN in shown. The regions indicated by the arrows are graphite islands. They are segregated below the step edges while the nanomesh covers the remaining part of the terraces. As can be seen in detail in Fig. 51(b) the carbon layer appears as a bunch of dots. They are separated by a distance of $2.7 \pm 0.1\,\mathrm{nm}$ and have an apparent height of $0.65 \pm 0.1\,\mathrm{\AA}$. The nanomesh units around them have broken wires and distorted shapes. The presence of graphite at these sub-monolayer coverages creates in normal emission UP spectra a decrease of the σ-band intensities. The work function of the sample remains the same and no double cut-off in the secondary photoelectron peak can be resolved. The spots of this superstructure were not recognized in the LEED patterns, which are dominated by the nanomesh periodicity.

6 h-BN on Palladium surfaces

The formation of a nanomesh on Rh(111) and Ru(0001) arose interest in the growth of similar structures also on other metal substrates with even larger lattice mismatches and different surface symmetries. For this reason the (111) and (110) surfaces of palladium were investigated [116, 143]. The Pd(111) surface was chosen because of the presence of a coincidence lattice observed by LEED after the exposure to $(HBNH)_3$ and the lack of previous STM studies on the resulting *h*-BN films [91]. The Pd(110) surface, was the first non-hexagonal surface that we investigated with the purpose to understand if a 'stretched'-honeycombed mesh can be grown on a rectangular substrate.

6.1 h-BN on Pd(111): Nanomesh or Moiré pattern?

The experiments were performed on a Pd(111) single crystal that was cleaned by repeated cycles of Ar^+ ion sputtering (15 min, acceleration voltage of 1 keV and sputtering current $\sim 1.5\,\mu\mathrm{A/cm^2}$) and exposure to 20 L of O_2 at 750 K with subsequent annealing to 1000 K. The *h*-BN layers were produced by exposing the clean Pd surface to $50-60$ L of $(HBNH)_3$ while keeping the surface at 1000 K. The carbon contamination estimated with XPS was below 1% of a monolayer.

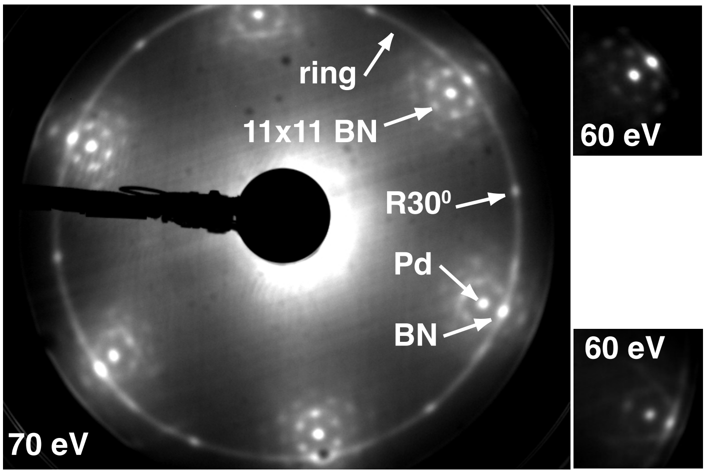

Figure 52: *LEED image of 1 ML of h-BN on Pd(111) recorded at 70 eV. The principal Pd lattice spots are surrounded by BN spots as indicated. Several h-BN structures can be identified: the predominant one is a (10×10) Pd unit cells, a R30°, and a ring containing BN spots which correspond to azimuthally disordered BN units on the surface. On the right-side, details of the same pattern recorded at 60 eV show the threefold symmetry of the fcc crystal. In the top-detail the BN spots are clearly visible, while on the bottom one the BN structure is smeared out to a ring.*

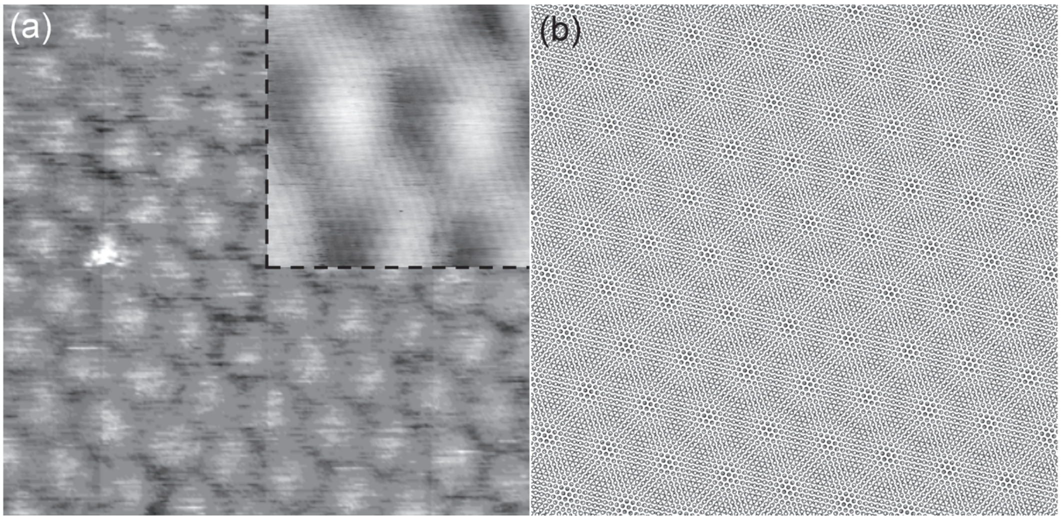

Figure 53: *(a) Constant current STM image of a Moiré pattern found on h-BN on Pd(111)* (20×20 nm^2, I_t=1 nA, V_s=1 V). *The inset in the upper right corner* (2.5×2.5 nm^2) *measured in the same tunneling conditions as (a), shows atomic resolution. The pattern is reproduced in (b) using an overlay of two atomic grids with lattice constants corresponding to the h-BN on Pd(111). The grids are not rotated against each other, i.e. the* (10×10) *structure is shown.*

LEED images show that on the surface there is a dominant hexagonal coincidence lattice with (11 × 11) *h*-BN units on top of (10 × 10) Pd unit cells, as shown in Fig. 52. This periodicity is expected from the −9% tensile lattice mismatch at RT between the in-plane nearest neighbor distance on the Pd(111) surface (2.751 Å) and the *h*-BN that gets reduced to 0.1% with this coincidence lattice. Besides these spots, also a ring that surrounds the (0,0) Pd lattice spot is visible on the images, indicating the presence of azimuthally rotated *h*-BN units on the surface. On the ring twelve spots can be easily identified: six belong to the BN units oriented along the Pd surface crystallographic directions, the other six to a R30°-structure where the *h*-BN lattice is rotated by 30° with respect to the substrate. The relative intensities of the ring and the R30°-spots vary in different experiments but a systematic dependence on the preparation conditions, such as contamination, deposition rate or dose, has not been found. A possible dependence on the sample temperature during deposition or a faster or slower sample cooling rate after deposition might be possible causes, but they were not investigated intentionally in these studies. Even if an ordered coincidence lattice is found with LEED, as in the case of *h*-BN on Rh(111) and Ru(0001), STM images do not show a nanomesh structure, but several Moiré patterns with different periodicities (from 11 to 27.5 Å) appear. At atomic resolution only one of the two different atoms in the *h*-BN lattice is imaged, as already seen in the STM images measured at low temperature for the *h*-BN on Rh(111).

It is likely that also in this case the atomic species imaged in STM are N. Also for the Moiré patterns created by NaCl on Cu(111) and Al(100) [41, 144] only the Cl^- ions are imaged as protrusions. These patterns arise from the superposition of two atomic layers with different periodicities and can be graphically reproduced by overlaying and rotating a *h*-BN layer, represented by only one atomic species, on the Pd atomic lattice. The darkest gray scale value is produced whenever a N atom sits on top of a Pd atom. This procedure reproduces quite well the observed STM contrast indicating that N-top sites have a higher tunneling resistance than bridge or hollow sites. The corrugation of the *h*-BN Moiré patterns ranges from values as small as 0.3 Å to values as high as 1.6 Å. This last corrugation, unusual for purely geometrical Moiré effects (ie. height difference between N on top and on hollow sites) could be related to changes in the local work function as shown recently for some ionic layers on metal substrates [43, 44].
The adsorption of *h*-BN induces a change in the Pd work function which gets reduced from 5.65 to 4.26 ± 0.05 eV. This value is slightly higher than the one of 4.0 eV published by Nagashima et al. [85]. The analysis of the valence band dispersion shows unambiguously that no structure with two *h*-BN species (as in the nanomesh) is present but a flat compact layer forms on this surface. In UP spectra measured at normal emission only one σ- and π-band are found at $\overline{\Gamma}$. The similarity between *h*-BN on Pd(111) and *h*-BN on Ni(111) is then clear. Differences arise if one looks at the dispersion along the $\overline{\Gamma \mathrm{K}}$ and $\overline{\Gamma \mathrm{M}}$ directions in the reciprocal space. The σ-bands described by *Grad et al.* [88] for Ni(111) seem to split up into different branches on Pd(111). This can be caused by the superposition of the band structures along the two directions due the presence of the R30°-structure. The coexistence of rotated *h*-BN domains is also observed with ARUPS for Ni(110) (as described in section 3.2.1) where the predominant (1×6) and (7×5) structures (rotated by 90° one to the other) can be identified in constant energy maps [96]. The role of the R30°-structure is not clear yet, the related six spots in LEED images have never been observed for *h*-BN layers grown on Ni surfaces, on Mo(110) or Ru(0001) but sometimes on Rh(111) and on Pt(111) [82] where the behavior of the *h*-BN seems to be similar to Pd. In this case the authors propose a R30°-structure with N atoms adsorbed on alternating on top and on bridge sites and suggest that its formation reduces the lattice mismatch between the BN and the Pt layers to $\sim 4\%$. In the same way on Pd(111) the lattice mismatch would be reduced to 5.1% but a $(\sqrt{3} \times \sqrt{3})$ R30° would be a structure more suitable to fit with the model proposed for Pt. However, no additional LEED spots are observed and therefore a compressed and thus corrugated layer is unlikely for Pd(111). A (11×11) overstructure with *h*-BN units rotated by 30° would lead also to a reduced lattice mismatch of 0.36% but again no LEED spots corresponding to such a coincidence lattice were observed.

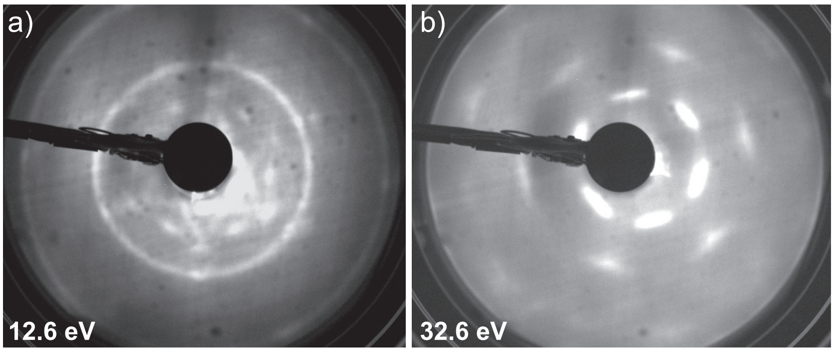

Figure 54: *(a) LEED image recorded at 12.6 eV of 1 ML of C_{60} grown at RT on 1 ML h-BN on Pd(111). The C_{60} spots are smeared out to a ring since no preferential orientation is favored. (b) After annealing to 600 K for 10 min the C_{60} layer orders. This LEED image is taken at 32.6 eV.*

The *h*-BN layer on Pd(111) has been exposed to C_{60} molecules. If 1 ML of molecules is adsorbed at RT no ordered overstructures appear in LEED patterns but again an intense ring around the (0,0) Pd principal spot indicates random orientations on the surface Fig. 54(a). From the analysis of the ring size, a distance of 9.8 ± 0.3 Å between C_{60} molecules is found. This indicates that the molecules lay flat and uncompressed on the surface as it is also found in STM images. If the C_{60} layer is annealed at 600 K (for 10 min), the molecules order along the Pd crystallographic directions Fig. 54(b).

6.2 h-BN on Pd(110)

The Pd(110) single crystal was cleaned by repeated cycles of Ar^+ ion sputtering (15 min, acceleration voltage of 750 eV and sputtering current $\sim 1.0\,\mu A/cm^2$) and exposure to 10 L of O_2 at 750 K with subsequent annealing to 1000 K. 90 L of $(HBNH)_3$ were used to grow *h*-BN layers at 1000 K and also in this case the carbon contamination was below 1% of a monolayer.

The STM pictures of *h*-BN on Pd(110) show again several Moiré patterns that arise from the incommensurate growth. The domains extend up to 100 nm and across steps. Different domains can coexist on the same terrace, as in Fig. 55, where two different domains (a 'stripe-like' and a 'dot-like') are separated by a boundary represented by a line of white features that are 1.3 ± 0.2 Å high. 'Stripe-like' domains were not found on the (111) surface, because they are due to the rectangular symmetry of the Pd(110) surface. The Pd-Pd distance is 2.75 Å along the close-packed $[1\bar{1}0]$ direction and 3.89 Å along the [001]. Also in this case, one atomic species in the *h*-BN layer is imaged with STM. The Moiré patterns reproduced with graphical overlap of a N (or B) and a Pd atomic grid, are six-fold periodic: for a 60° rotation the same kind of pattern is found. Defining as

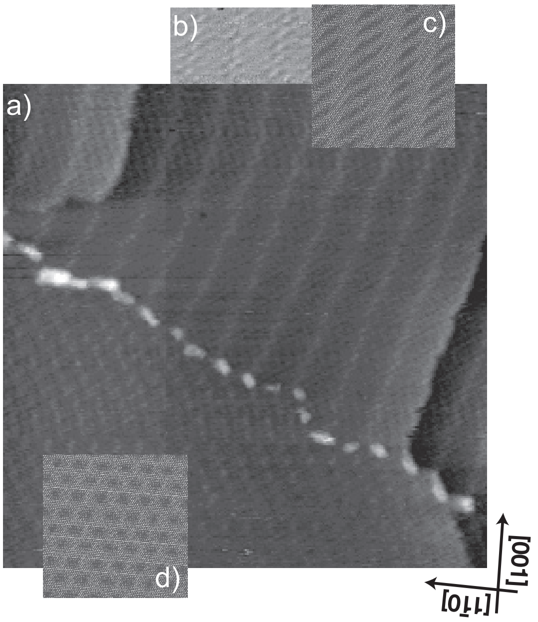

Figure 55: *(a) STM image (50×50 nm^2, I_t=1 nA, V_s=1 V) of 1 ML h-BN/Pd(110). Two Moiré patterns (a 'stripe-like' and a 'dot-like') separated by a domain boundary are imaged on the same terrace. The upper 'stripe-like' domain extends over three different terraces. (b) High resolution STM image for a region of the 'stripe-like' domain of (a). (c) and (d) represent atomic models. The domain in (c) is reproduced by a clockwise rotation by 5° of a hexagonal layer of N atoms with respect to the* [1$\bar{1}$0] *on the Pd(110) surface. The 'dot-like' domain in (d) corresponds to the 0° orientation where one of the N-N Bravais vectors is aligned along the* [1$\bar{1}$0].

0° rotation the configuration in which one of the primitive lattice vectors of the *h*-BN layer is parallel to the [1$\bar{1}$0] crystallographic direction of the substrate, the 0° domain ('dot-like' in Fig. 55 (d)) appears as a hexagonal lattice with a lattice constant of 27.5 Å, which corresponds to 10 Pd lattice constants along the close packed [1$\bar{1}$0] direction. The domain in the upper part of Fig. 55(a) can be simulated with a clockwise rotation of 5° with respect to the [1$\bar{1}$0] direction of the substrate (Fig. 55(c)). The atomic model reproduces the Moiré pattern measured in a high resolution image (Fig. 55(b)) in great detail, including the dark parallel lines that cross the bright stripes at a slanted angle. It seems that the microscope images bright ridges along the darker Moiré stripes (Fig. 55(b)), leading to the continuous bright stripes appearing in the STM image. Therefore besides topographic effects, also electronic effects seem to be present. The domain in Fig. 56(a) can be created with a counterclockwise rotation of 6° as seen in the atomistic plot in Fig. 56(b). The line profile in Fig. 56(c) shows the small apparent corrugation of the Moiré contrast that does not necessarily reflect the true topography of the *h*-BN overlayer but can also be due to its insulating nature. Many STM images taken on different sample preparations and surface positions have been analyzed but it was not possible to identify and determine the absolute predominance of one Moiré pattern with respect to the others. For a wide range of orientations (for example between 20° and 40° of rotation from the [1$\bar{1}$0] direction) the contrast reproduced in the atomic models is not very distinctive, thus not easy to distinguish with the microscope.

The global information on the distribution of different rotated domains can be extracted from LEED images. LEED patterns recorded over a wide energy range (from 50 to 300 eV) show the large BN-ring that surrounds each Pd principal lattice spot.

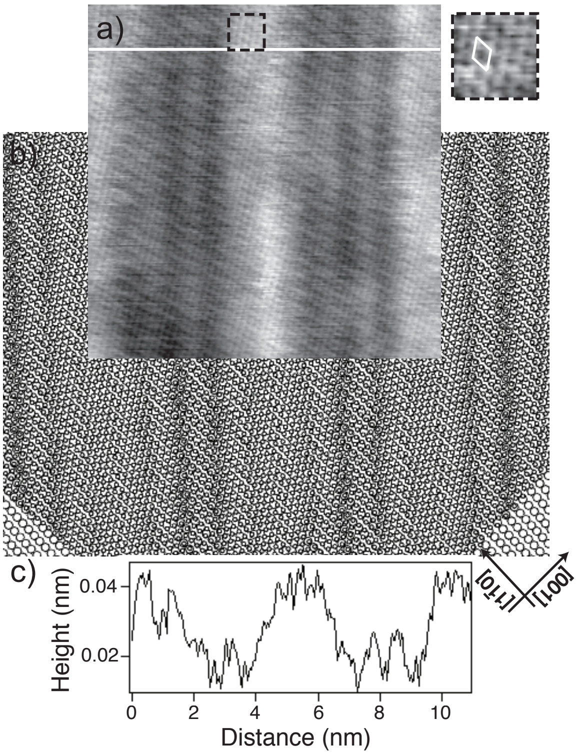

Figure 56: *(a) STM image (10×10 nm^2, I_t=2 nA, V_s=1 V) of a single h-BN domain on Pd(110). This Moiré pattern is reproduced in an atomic model (b) with a counterclockwise rotation of 6° of the N layer with respect to the* $[1\bar{1}0]$ *direction on Pd(110). The dashed square selection in (a) is enlarged in the insert (1×1 nm^2) on the right. It shows with atomic resolution the hexagonal layer and its unit cell. In (c) the cross-sectional profile along the horizontal white line in (a).*

When the energy of the electrons is increased, the diameter of the rings shrinks which is characteristic of the simple in-plane scattering process within the BN layer:

$$d\sin(\theta) = n\lambda, \quad \theta = \arcsin\left(\frac{n}{d}\sqrt{\frac{150}{E(eV)}}\right) \tag{25}$$

where d is the in-plane distance between atomic rows, n is the diffraction order, θ is the scattering polar angle and E is the electron energy. A simple scheme can be found in Fig. 57(e). A plot of dependence of θ on the energy E is shown in Fig. 57(f) for a series of subsequent LEED images. The dispersion of the data points is fitted with Eq. 25 using $d = 2.165$ Å for the h-BN lattice and in the first order diffraction limit (n =1). The data fit well with the proposed model. From the radii of the circles a lattice constant of 2.51 ± 0.05 Å is found for the N-N or B-B distance in a h-BN unit.

Fig. 58(a) and (c) show two LEED images measured at 70 eV for two different h-BN on

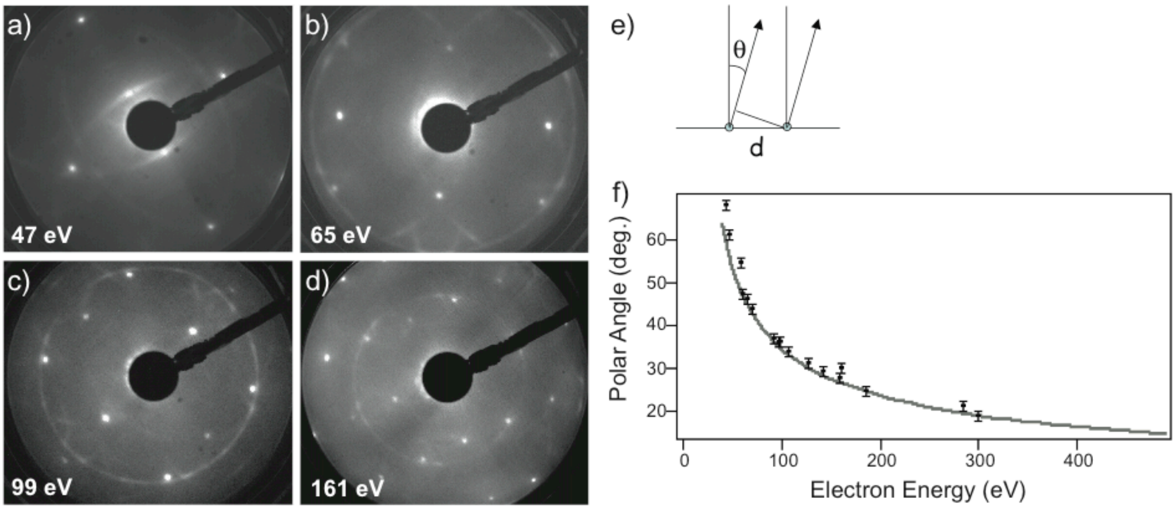

Figure 57: *(a-d) LEED patterns of h-BN on Pd(110) measured at the energies indicated. As the energy is increased, the diameter of the ring, which is due to electron diffraction within the BN layer, decreases as expected from the simple in-plane scattering model as in (e). This can be seen from the behavior of the polar angle at which the electrons are diffracted (which is proportional to the ring diameter) calculated from Eq. 25 which decreases as the electron energy increases.*

Pd(110) preparations, while Fig. 58(b) and (d) are the corresponding distributions of the intensities along the circles centered at the (0,0) Pd lattice spot. The most intense peaks (twin-peaks) in the profile of Fig. 58(b) appear at the angles where the circle is crossed by other circles centered at some other Pd principal lattice spot. The minor peaks that show up in between contain information on domain abundances. Three series of peaks, each with a periodicity of 60°, can be found (the first one of each series is labeled 'A', 'B' or 'C', respectively) corresponding to three preferred orientations of the *h*-BN layer. In the convention introduced for the STM images, series 'B' corresponds to *h*-BN aligned with the [001] direction (30° orientation), series 'A' and 'C' to a counterclockwise and a clockwise rotation of $17.0 \pm 0.5°$ respectively. The profile in Fig. 58(d) reflects a dramatically different domain distribution: besides the intense twin-peaks only two series of peaks clearly stand out, labeled 'D' and 'B'. The peaks 'D' appear in the center of the twin-peaks and correspond to *h*-BN oriented along the $[1\bar{1}0]$ direction (0° orientation). The peaks 'B' correspond again to *h*-BN aligned along the [001] direction (30° orientation) as in the previous profile (Fig. 58(b)). The Moiré pattern that would correspond to this latter configuration is not distinctive. The coincidence of N on top positions should appear every 9 palladium lattice constants or every 14 nitrogen atom along [001]. The reason for the different domain distributions formed in this case is not clear; it might

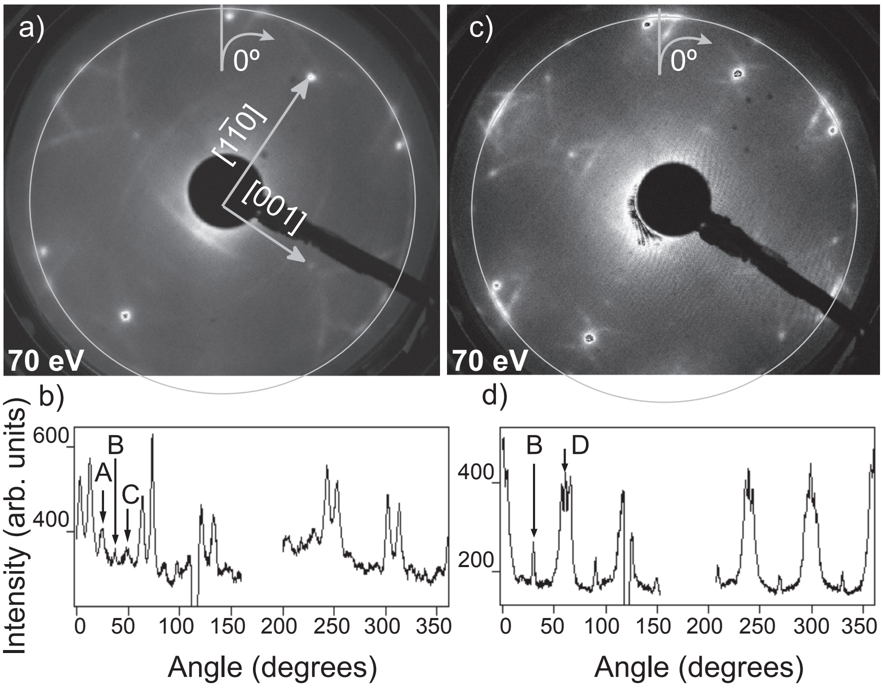

Figure 58: *(a) and (c) LEED images of 1 ML h-BN on Pd(110) recorded at 70 eV from two different preparations of the same structure. In (b) the variation of the intensity along the circle centered at the (0,0) lattice spot of (a) is plotted. The zero azimuthal angle scale is given in the upper part of (a) and the angles are measured clockwise from there. Dominant twin peaks occur at crossing with higher-order circles. In the region between 150° and 200° the circle is off limits of the image and at 115° the fixture of the electron gun is crossed. The peaks labeled 'A'-'C' and 'B' represent preferred domains (17° and 30°, respectively). (d) shows the same profile taken in (c). The predominant domains labeled 'B' and 'D' in this sample preparation appear at 30° and 0° respectively.*

be attributed to the different procedure used to clean the Pd sample. After the cycles of sputtering in the case of the first profile (Fig. 58(b)) the sample was exposed to 8 L of O_2, while in the second case (Fig. 58(d)) 45 L of O_2 have been used. The exposure to high doses of oxygen is known to be efficient for removing carbon contaminants. Another possible reason might be the slightly contaminated $(HBNH)_3$ precursors used in the second case. In the analysis of several LEED profiles (as those of Fig. 58(b) and (d)) obtained from images recorded at different energies and for different but equivalent sample preparations, the domain with 30° orientation (peak 'B') has always been found. Therefore this configuration is one of the energetically most stable. The other domains do not always appear predominantly. To test the thermal stability of the Moiré structures in general, the sample was annealed under the LEED apparatus. The ring shows up to at least 950 K and the domain distribution along it does not change significantly.

6.2.1 C_{60} decoration: Moiré patterns on Moiré patterns

The features of a single layer of C_{60} molecules adsorbed on the *h*-BN on Pd(110) domains have been characterized with LEED and STM. Besides the principal Pd spots, the LEED patterns do not show extra spots due to the C_{60} adlayer; the *h*-BN ring is strongly suppressed and only the twin-peaks (as in Fig. 58(d)) are still visible.

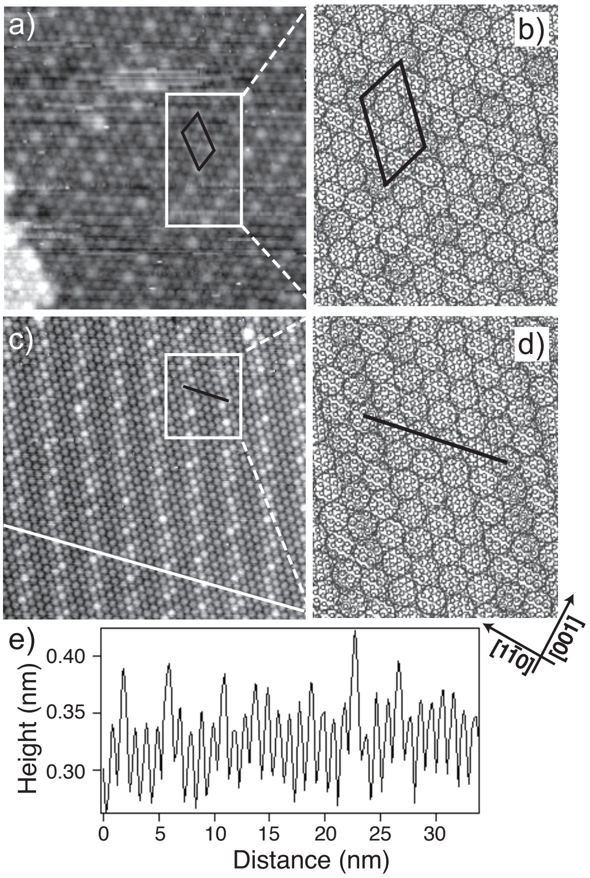

Figure 59: *(a) and (c) STM images (a: 23×23 nm^2, I_t=1 nA, V_s=2 V; c: 30×30 nm^2, I_t=2 nA, V_s=1 V) of 1 ML C_{60} on 1 ML h-BN/Pd(110). The bright contrast in these two coexisting domains is interpreted as a C_{60} layer following the configuration of the h-BN Moiré pattern. In a microscopic model ((b) and (d)) the global Moiré contrast is mainly defined by the orientation of the h-BN layer. Thus the bright molecules appear as dark spots since they correspond to C_{60} covering areas with a high density of N atoms on top or nearly on top of Pd atoms (darkest regions). (b) and (d) reproduce atomically the rectangular areas of (a) and (b) respectively. While in (a) the h-BN layer is rotated by 1° counterclockwise away from the crystallographic direction of the substrate, in (c) the layer is rotated of 5° counterclockwise. Black lines follow periodic features of the patterns. (e) Cross-sectional profile along the diagonal continuous white line in (c).*

Nevertheless the STM images (Fig. 59(a) and (c)) show highly regular domains that are interpreted as C_{60} Moiré patterns on top of *h*-BN Moiré patterns. In the model depicted in Fig. 59(b) the *h*-BN layer is rotated counterclockwise by 1° with respect to the substrate (a domain similar to the 'dot-like' of Fig. 55), and in Fig. 59(d) there is a 5° counterclockwise rotation. A distance of $10\,\text{Å}$ between the C_{60} molecules has been used in the model, since an average value of $9.7 \pm 0.7\,\text{Å}$ has been determined from several STM images. The brightest C_{60} molecules in the STM images correspond, in the model, to molecules covering an area with a high density of N atoms placed on top or nearly on top of Pd atoms. The Moiré contrast is mainly defined by the orientation of the *h*-BN layer while the C_{60} molecules accommodate themselves in order to follow the topography below. Since the C_{60} molecules form a conducting overlayer, it is possible to estimate a corrugation of the Moiré pattern from STM line profiles (as Fig. 59(e)). The differences in height between the brightest and darkest C_{60} molecules yield a value of $0.53 \pm 0.12\,\text{Å}$ as determined from the analysis of different images recorded at tunneling voltages between 1 V and 2 V. Moreover, by means of LEED and STM it has been demonstrated that nanostructures formed in 1 ML *h*-BN/Pd(110), and 1 ML of C_{60} adsorbed on it, are stable even after air exposure.

As conclusion of this study, *h*-BN on the Pd surfaces considered forms a weakly physisorbed layer. The binding energy per *h*-BN unit is $\sim 0.2\,\text{eV}$ [104], less than on Rh and Ru. The Pd atomic potential is not strong enough to elastically distort the *h*-BN overlayer in order to form a pseudomorphic film, therefore it grows incommensurate in some domains on Pd(111) and on the entire surface on Pd(110). The strain induced by the lattice mismatch is relieved in the formation of Moiré patterns. Rotated *h*-BN domains arise in order to minimize the energy of the system [145]. The *h*-BN on Pd(110) can be considered as a model system for 'tunable nanostructures'. The exposure to specific doses of H_2, for example, might lead to the disappearance of some domains at the expense of the most favored ones. Moreover, the choice of a particular Pd(110) vicinal surface might give the possibility to grow films with a single Moiré domain and thus with a single mono-periodicity and symmetry. The potential utility of this system is even enhanced when C_{60} layers are grown on top of the *h*-BN. The C_{60} molecules on *h*-BN/Pd(110) 'memorize the substrate corrugation', following the topographic patterns generated by the underlying *h*-BN film.

7 Flat layers or nanomesh?

In the previous chapters a description of the different *h*-BN nanostructures forming on the Rh, Ru, Ni, and Pd hexagonal surfaces has been given in detail. Further information on these systems can be gained from the direct comparison between them. In particular the focus is now given to the valence band structure and the quantification of *h*-BN coverage from XPS data.

7.1 Vacuum alignment in UP spectra

The experiments done so far show that whenever *h*-BN grows on the (111) surface of a transition metal, and if the system is lattice mismatched, then in the LEED patterns a hexagonal superlattice appears. It can be due either to a nanomesh structure or to an almost flat layer of the Moiré kind. An efficient way, besides STM, to recognize if a nanomesh forms on the surface, is the observation of the UP spectra measured at normal emission. While for a single flat *h*-BN layer only one σ and π bands are present, for the nanomesh two pairs of σ and π bands appear. If the spectra are plotted with respect to the Fermi level, then the bands of the same nature have different positions.

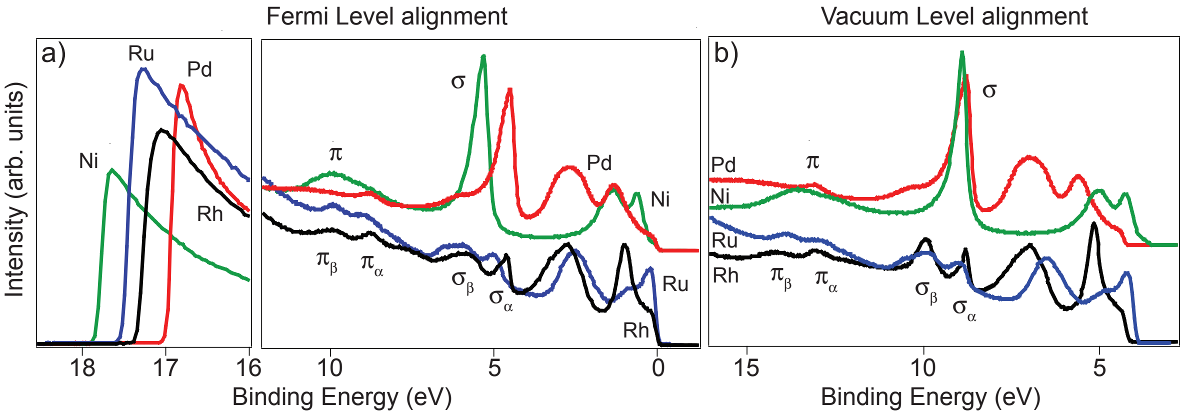

Figure 60: *He Iα excited valence band spectra measured at $\overline{\Gamma}$ for h-BN on Ni(111), Pd(111), Rh(111) and Ru(0001). For simplicity the spectra are named as the substrate covered by h-BN. (a) The different spectra are plotted with respect to the Fermi level. On the left a zoom on the energy range of the work function. The position of the σ and the π bands and the value of the work function are different in the four systems. In (b) the UP spectra are referred to the vacuum level, as for the corresponding figure in (a) the h-BN/Pd(111) and h-BN/Ni(111) spectra are intentionally shifted in intensity. In (b) the σ bands of h-BN on Pd(111), Ni(111) and the σ_α of h-BN on Rh(111) and Ru(0001) are aligned, thus showing a similar weak bonding to the substrate.*

E_f	ϕ_{clean}	ϕ_{h-BN}	σ_α	σ_β	π_α	π_β
Ni(111)	5.35	3.53	5.3		10.0	
Pd(111)	5.65	4.26	4.61		9.02	
Rh(111)	5.50	4.15	4.57	5.70	8.76	9.83
Ru(0001)	5.44	4.00	4.97	5.91	9.00	9.83
E_v	ϕ_{clean}	ϕ_{h-BN}	σ_α	σ_β	π_α	π_β
Ni(111)	5.35	3.53	8.83		13.53	
Pd(111)	5.65	4.26	8.87		13.28	
Rh(111)	5.50	4.15	8.72	9.85	12.91	13.98
Ru(0001)	5.44	4.00	8.97	9.91	13.00	13.83

Table 4: *Experimental values in (eV) for the work function of the clean and h-BN covered surfaces in the first column, the binding energies of the different bands.* σ_α *and* π_α *indicate* σ *and* π *for h-BN/Ni(111) and h-BN/Pd(111). In the top part of the table the binding energies are given with respect to the Fermi level (*E_f*), while in the bottom part to the vacuum level (*E_v*). All the values are estimated with ±0.1 eV as error bar.*

Nagashima et al. [85] already showed that for *h*-BN on Ni(111), Pd(111) and Pt(111) (where flat layers form) the σ-band binding energies are aligned when referred to the vacuum level (with a value of $8.9 \pm 0.1\,\text{eV}$ for Ni and $8.8 \pm 0.1\,\text{eV}$ for Pd and Pt). This behavior is expected since no *h*-BN related states are present at E_f. The vacuum alignment is a consequence of the poor hybridization or state mixing of the σ bands with the substrate bands (in particular those of *d* character) and the correspondingly similar charge distribution at the interface between the *h*-BN and the vacuum which determines the ionization potential. Therefore, if the vacuum level is used as reference, i.e. if the work function is summed to the value of the binding energy, then the σ bands of the flat layers (Pd and Ni) align with the σ_α of the nanomesh (Rh and Ru). This suggests that the σ_α is a band with weak bonding as for 'physisorbed' systems, while for the σ_β the bond is stronger, similar to chemisorption. The values for the aligned σ bands well agree to the published ones [85]. In Table (4) all the values of the binding energies of the σ and π bands and of the work functions are given for the different systems.

7.2 Coverage calculation from XPS spectra

In order to calculate the coverage of *h*-BN on different substrates we quantify XPS data by comparing the intensity of an overlayer core-level signal to one of the substrate. The measured peak intensity (or photoelectrons current) at a certain energy level of an element A in a sample (M), can be expressed theoretically as [146, 147]:

$$I_A = C\ \sigma_A\ T_A \int_z N_A(z)\ exp\left(\frac{-z}{\lambda_M(E_A)cos\theta}\right)\ dz \tag{26}$$

where C is a proportionality factor which depends on the detector efficiency and the angular asymmetry of the emitted intensity, σ_A is photoionization cross section, N_A the density of atoms A, T_A the analyser transmission, $\lambda_M(E_A)$ is the inelastic mean free path (IMFP) in the matrix M, θ is the detection angle and z is the coordinate orthogonal to the sample surface.

The intensity recorded for the pure element A is:

$$I_A^0 = C\ \sigma_A\ \lambda_M(E_A)\ N_A^0\ T_A \tag{27}$$

where N_A^0 is atom density (atoms/unit volume) in the pure reference bulk sample and is simply a_A^-3 where a_A is the 'atomic size' or the 'monolayer thickness' and it can be expressed (in nm) as:

$$a_A = \left(\frac{W}{\rho n N_{AV}} \times 10^{24}\right)^{\frac{1}{3}} \tag{28}$$

W is the atomic or molecular weight, n is the number of atoms in the molecule, N_{AV} is the Avogadro's number and ρ is the bulk atomic density in $\mathrm{kg\,m^{-3}}$. In this analysis N_A^0 will be expressed as ratio between the surface atom density (atoms/unit area) n_A^0 and the distance a_A^0 between neighboring atomic planes. The IMFP of electrons in solids obeys an universal curve, which for elements with energies (E) from 1 to 1000 eV is written as (in nm) [148]:

$$\lambda_A(E) = a_A\left(\ \frac{538}{E^2} +\ 0.41\ (a_A\ E)^{\frac{1}{2}}\right). \tag{29}$$

In order to find the coverage of an adsorbate A on a substrate B one calculates the ratio of the photoelectron current due to the adsorbates I_A and to the substrate I_B. If one assumes that A forms a thin overlayer of thickness d_A on B then:

$$I_B = I_B^0\ exp\left(\frac{-d_A}{\lambda_A(E_B)cos\theta}\right), \qquad I_A = I_A^0\ \left[1 - exp\left(\frac{-d_A}{\lambda_A(E_A)cos\theta}\right)\right]. \tag{30}$$

The ratio becomes:

$$\frac{I_A}{I_B} = \frac{I_A^0}{I_B^0}\ \frac{\left[1 - exp\left(\frac{-d_A}{\lambda_A(E_A)cos\theta}\right)\right]}{exp\left(\frac{-d_A}{\lambda_A(E_B)cos\theta}\right)} = \frac{\lambda_A(E_A)}{\lambda_B(E_B)}\ \frac{T_A}{T_B}\ \frac{n_A^0 a_B^0}{a_A^0 n_B^0}\ \frac{\sigma_A}{\sigma_B}\ \frac{\left[1 - exp\left(\frac{-d_A}{\lambda_A(E_A)cos\theta}\right)\right]}{exp\left(\frac{-d_A}{\lambda_A(E_B)cos\theta}\right)} \tag{31}$$

using Eq. 27 for I_A^0 and I_B^0. Eq. 31 can be simplified if $d_A << \lambda_A$, so that the exponential terms can be expanded in Taylor series:

$$1 - exp\left(\frac{-d_A}{\lambda_A(E_A)cos\theta}\right) \sim \frac{d_A}{\lambda_A(E_A)\cos\theta}, \qquad exp\left(\frac{-d_A}{\lambda_A(E_B)cos\theta}\right) \sim 1 - \frac{d_A}{\lambda_A(E_B)\cos\theta}. \tag{32}$$

The most simple expression for Eq. 31 becomes:

$$\frac{I_A}{I_B} = \frac{T_A}{T_B}\frac{n_A^0 a_B^0}{a_A^0 n_B^0}\frac{\sigma_A}{\sigma_B}\frac{d_A}{\lambda_B(E_B)\cos\theta}. \tag{33}$$

From Eq. 33 it is possible to determine directly the number of monolayers (N_{ML}^0) of an adsorbate A on the substrate B without knowing the monolayer thickness of the overlayer a_A^0:

$$N_{ML}^0 = \frac{d_A}{a_A^0} = \lambda_B(E_B)\cos\theta\,\frac{I_A}{I_B}\frac{\sigma_B}{\sigma_A}\,\frac{n_B^0}{a_B^0 n_A^0}\frac{T_B}{T_A}. \tag{34}$$

If one considers all the first order terms in the expansion of the exponential terms, then Eq. 31 becomes:

$$\frac{I_A}{I_B} = \frac{T_A}{T_B}\frac{n_A^0 a_B^0}{a_A^0 n_B^0}\frac{\sigma_A}{\sigma_B}\frac{d_A}{\lambda_B(E_B)\cos\theta}\left(1 - \frac{d_A}{\lambda_A(E_B)\cos\theta}\right)^{-1} \tag{35}$$

and the number of monolayers is:

$$N_{ML} = N_{ML}^0\left(\frac{\lambda_A(E_B)\cos\theta}{\lambda_A(E_B)\cos\theta + N_{ML}^0\ a_A^0}\right). \tag{36}$$

The transmission function of our spectrometer has been determined experimentally from the analysis of clean Au polycrystal spectra with monochromatized Al Kα radiation. From the plot of the peak-areas of the Au peaks (4*f*, 4*d*, 4*p* and 4*s*) divided by the corresponding cross sections with respect to the corresponding kinetic energy it is found that:

$$\frac{I_{Au4x}^0}{\sigma_{Au4x}} \propto T_{Au}\lambda_{Au}(E_{Au4x}) = (E_{Au4x})^{0.85\pm0.2} \tag{37}$$

which with Eq. 29 suggests a general dependence for the transmission to the kinetic energy of the type $T_A \propto E_A^{0.35}$.

7.2.1 *h*-BN coverage on Rh(111), Ru(0001), Ni(111) and Pd(111)

The coverage of B and N in *h*-BN on Rh(111), Ru(0001), Ni(111) and Pd(111) has been calculated with the three different degrees of approximations that can be done in the simplification of Eq. 31. In the first case (i) the B and N coverages have been calculated from the exact solution of Eq. 31, in the second case (ii) via the simple Eq. 34 where the advantage is that no assumption has to be made on the BN layer thickness (d_{hBN})

and in the third case (iii) from Eq. 41 keeping the first order terms in the exponential series expansion. In this way it is possible to understand how critical the simplification of the exponential terms in Eq. 31 can be for the calculation of the absolute values of the coverage.

For the case (i) d_{hBN} is calculated as:

$$\frac{I_A}{I_B}\frac{\lambda_B(E_B)}{\lambda_A(E_A)}\frac{\sigma_B}{\sigma_A}\left(\frac{n_B^0 a_{hBN}^0}{n_A^0 a_B^0}\right)\left(\frac{E_B}{E_A}\right)^{0.35} exp\left(\frac{-d_{hBN}}{\lambda_A(E_B)}\right)+exp\left(\frac{-d_{hBN}}{\lambda_A(E_A)}\right)-1\ =0. \quad (38)$$

where A represent the nitrogen or boron in the *h*-BN overlayer and B is the substrate analyzed (Ni, Rh, Ru or Pd) and considering that for normal emission experiments $\cos\theta = 1$. The coverage or number of layers (N_{ML}) is given by:

$$N_{ML} = \frac{d_{hBN}}{a_{hBN}} \quad (39)$$

where for the thickness of a single *h*-BN layer is taken the experimental value of 0.22 nm [86]. For the case (ii) the number of monolayers is calculated simply as:

$$N_{ML} = \frac{d_{hBN}}{a_{hBN}} = \lambda_B(E_B)\ \frac{I_A}{I_B}\frac{\sigma_B}{\sigma_A}\ \frac{n_B^0}{a_B^0 n_A^0}\ \left(\frac{E_B}{E_A}\right)^{0.35} \quad (40)$$

For the case (iii) the number of monolayers is given by Eq. 36:

$$N_{ML} = N_{ML}^0\left(\frac{\lambda_A(E_B)\cos\theta}{\lambda_A(E_B)\cos\theta + N_{ML}^0\ a_{hbn}^0}\right). \quad (41)$$

where N_{ML}^0 is the number of monolayers calculated from Eq. 40. The values for the kinetic energies are found from the centres of Gaussian fits of the experimental peaks. The intensities are determined calculating the area under the peak with a linear background. The statistical and systematic errors in the evaluation of the peak intensity is ∼7%.

Since Ru is a *hcp* crystal, at normal emission the intensity of the Ru peaks is higher than for the Rh, Ni and Pd. For this reason the intensities of the Ru 3*s* peaks have been divided by the correction factor 1.33. This value has been found considering the difference in intensity in the [111] direction between the XPD-patterns of the Ru 3*s* and the one of Rh 3*s* peaks measured when the surface was covered by *h*-BN. The parameters used for the calculation of the coverage are summarized in Table (5) and Table (6). The values of the IMFP for the metals have been taken from the NIST database [149], while in order to evaluate the IMFP of substrate photoelectrons through the BN layer, the experimental value of the IMFP of the bulk *h*-BN $\lambda_{hBN} \sim 1.8$ nm at 1000 eV [150] has been scaled for the different substrate or N 1*s* or B 1*s* kinetic energies.

The data analyzed here belong to different experiments performed in three years, with different borazine or trichloroborazine fillings, different Al Kα source performances (especially count rates) and on single crystals or thin films (in the case of Rh(111), Ru(0001)

	N^0 (atoms/ cm^2)	a_B^0(Å)	level	E_{kin} (eV)	σ (Mb)
Rhodium	1.60 10^{15}	2.194	$Rh3s$	859.0	0.038
Ruthenium	1.58 10^{15}	2.204	$Ru3s$	901.2	0.036
Nickel	1.86 10^{15}	2.032	$Ni3s$	1376.0	0.012
Palladium	1.53 10^{15}	2.246	$Pd3s$	814.7	0.036
nitrogen	1.84 10^{15}		$N1s$	1088.6	0.024
boron	1.84 10^{15}		$B1s$	1296.4	0.0066

Table 5: *Parameters used in the calculation of the coverage of h-BN on Rh(111), Ru(0001), Ni(111) and Pd(111). The cross sections (σ) are taken from [151] (σ is measured in barn: 1b=$10^{-28}m^2$), the surface atomic densities with the surface lattice constants from Table (1) and the a_B^0 are the distances between neighboring crystallographic planes in the direction orthogonal to the (111) or (0001) surfaces of the single crystals here used.*

IMFP (nm)					
$\lambda_{Rh}(E_{Rh3s})$	1.254	$\lambda_{hBN}(E_{Rh3s})$	1.675	$\lambda_{hBN}(E_{N1s})$	1.885
$\lambda_{Ru}(E_{Ru3s})$	1.394	$\lambda_{hBN}(E_{Ru3s})$	1.715	$\lambda_{hBN}(E_{B1s})$	2.057
$\lambda_{Ni}(E_{Ni3s})$	1.888	$\lambda_{hBN}(E_{Ni3s})$	2.120		
$\lambda_{Pd}(E_{Pd3s})$	1.631	$\lambda_{hBN}(E_{Pd3s})$	1.631		

Table 6: *The IMFPs of the different substrates for the kinetic energies given in Table (5) are taken from experimental data [149]. While the $\lambda_{hBN}(E_{kin})$ are calculated scaling experimental values for bulk h-BN [150].*

and Pd(111)). In this analysis 20 preparations of *h*-BN on Rh(111), 4 for Ru(0001), 6 for Ni(111) and 7 for Pd(111) are considered.

The mean values for the N and B coverages found for different experiments with the three approximation (i) and (ii) and (iii) are summarized in Table (7) and the error bars associated with these values are the statistical errors on the data that mainly reflect the reproducibility of the preparations. The N and B coverages are shown in Fig. 61 where they are calculated with the exact method (i) and are plotted versus the *h*-BN film stoichiometry (S_{NB}), defined as:

$$S_{NB} = \frac{I_{Nitrogen}}{I_{Boron}} \frac{\sigma_{Boron}}{\sigma_{Nitrogen}} \left(\frac{E_{Boron}}{E_{Nitrogen}}\right)^{0.35} . \tag{42}$$

A possible source of error in the estimation of S_{NB} can be due to the value of the B and N photoionization cross sections. In fact in this analysis it is not considered that possi-

Method (i)	N_{ML} N	N_{ML} B	S_{NB}
Rh(111)	1.01 ± 0.26	0.97 ± 0.28	1.04 ± 0.24
Ru(0001)	0.85 ± 0.14	0.98 ± 0.18	0.84 ± 0.05
Ni(111)	1.05 ± 0.20	1.22 ± 0.22	0.85 ± 0.12
Pd(111)	0.93 ± 0.38	0.85 ± 0.24	0.97 ± 0.24
Method (ii)	N_{ML} N	N_{ML} B	S_{NB}
Rh(111)	1.08 ± 0.29	1.05 ± 0.33	1.04 ± 0.24
Ru(0001)	0.90 ± 0.15	1.05 ± 0.20	0.86 ± 0.05
Ni(111)	1.10 ± 0.22	1.30 ± 0.26	0.85 ± 0.12
Pd(111)	1.00 ± 0.36	0.92 ± 0.28	1.10 ± 0.16
Method (iii)	N_{ML} N	N_{ML} B	S_{NB}
Rh(111)	0.95 ± 0.22	0.91 ± 0.24	1.04 ± 0.24
Ru(0001)	0.80 ± 0.18	0.93 ± 0.20	0.86 ± 0.05
Ni(111)	0.98 ± 0.12	1.15 ± 0.16	0.85 ± 0.12
Pd(111)	0.88 ± 0.28	0.81 ± 0.22	1.10 ± 0.16

Table 7: *Mean values of the coverage of h-BN on Rh(111), Ru(0001), Ni(111) and Pd(111) calculated from Eq. 38 and Eq. 39 on the top part, from Eq. 40 in the middle part and from Eq. 41 on the bottom part. In the last column on the right the mean values of the N:B stoichiometry (S_{NB}) are shown. The error bars here given are twice the standard deviation of the data.*

ble charge transfer between the two atomic species can influence the atomic potential, leading to deviations to the one of isolated species here used (from [151]). The resulting mean values obtained with all the methods are compatible with 1 ML of B and N on all surfaces. The use of the simplified formula to calculate the coverage (method (ii)) overestimates of 5 to 8% the exact solutions, while there is an underestimation of 5 to 7% within the first oder exponential expansion considered with method (iii) as shown in Fig. 62. The high values found for the coverage of the B on the case of Ni can be connected to the asymmetric shape of the B 1*s* peak at higher binding energies with respect to the peak position, a feature that is not present in the B 1*s* peaks for the other systems (Fig. 65). It is unlikely that this is connected to the presence of subsurface B atoms. For *h*-BN on Ni(100) [93], for example, produced with CVD of B_2H_6 and NH_3, the B 1*s* peak has two components: the one at higher binding energy is associated with B atoms belonging to BN units, while the one that belongs to a pure B phase sits at $\sim 2\,\mathrm{eV}$ lower binding energy and not at higher. If one would not consider the asymmetric peak tail in the peak area then the intensity would decrease by 26±0.4%, and for example the B

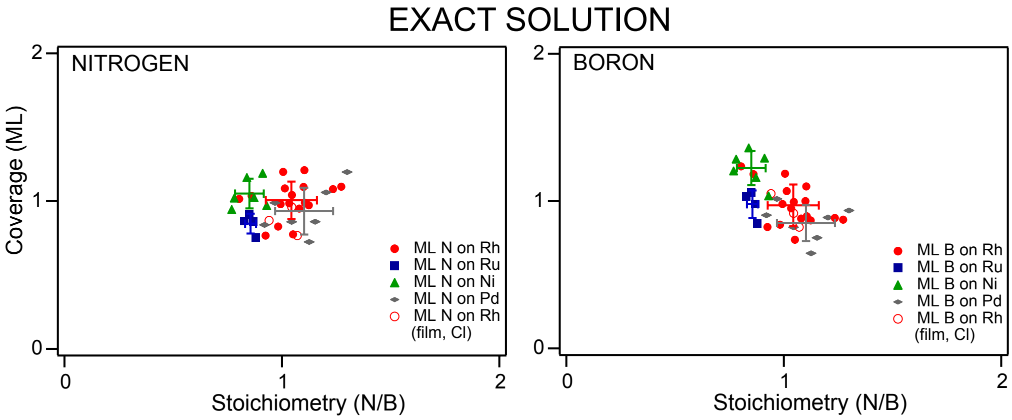

Figure 61: *Coverage of h-BN on Rh(111), Ru(0001), Ni(111) and Pd(111) calculated from Eq. 38 and Eq. 39 and plotted versus the stoichiometry (S_{NB}). The error bars in the mean value in the figure are the standard deviation of the data. The open circles belong to h-BN films prepared either on thin Rh(111) films, either on Rh(111) single crystals but with ($ClBNCl)_3$ instead of $(HBNH)_3$.*

on Ni(111) coverage calculated with method (i) would be only 0.89 ML. This result has been obtained by fitting the B 1*s* peaks with Guassians and comparing the area under the curve with the total area of the measured peak.

Regarding the relative concentrations of B and N atoms in the BN layers for the different systems, on Rh the film is stoichiometric, on Pd it is N rich and on Ni and Ru it is B rich (Table (7)). A few points in Fig. 61 show that an extra presence of boron is connected

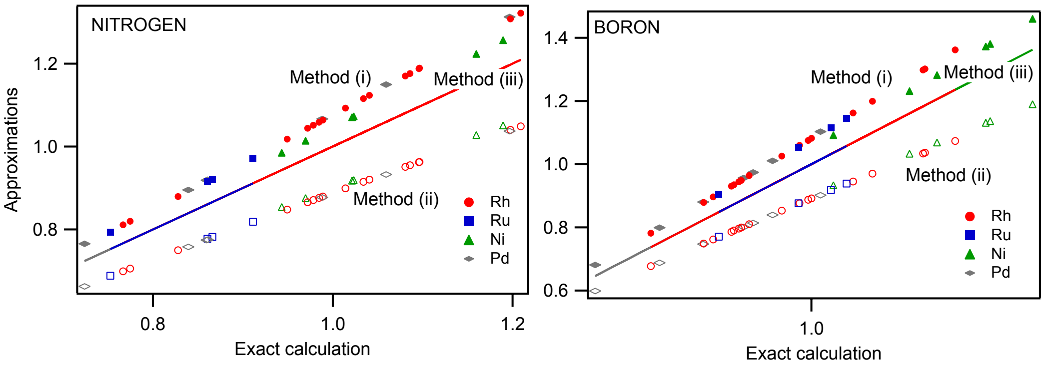

Figure 62: *The value for the coverage of N (left) and B (right) found with the three different methods ((i) exact solution, (ii) simplified solution and (iii) first order solution) are plotted versus those found with the analytic solution (i) of Eq. 38 and Eq. 39. The straight line represent the exact solution, method (ii) overestimates the exact coverage and method (iii) gives underestimated values as can be seen from the deviations from the lines.*

	$N^0_{sub}/N^0_{N\ or\ B}$	T_{sub}/T_N	T_{sub}/T_B	$N^0_{sub}T_{sub}/N^0_N T_N$	$N^0_{sub}T_{sub}/N^0_B T_B$
Rhodium	0.869	0.932	0.865	0.81	0.75
Ruthenium	0.859	0.936	0.880	0.80	0.76
Nickel	1.011	1.086	1.021	1.097	1.11
Palladium	0.812	0.90	0.850	0.73	0.69

Table 8: *The values of the surface atom densities ratios between the substrates in the first column (sub) and the one of N or B used in the calculation are summarized in the second column from the left. In the third and fourth column the transmission ratios and on the fifth and sixth column the products of the atom densities ratios and the transmission ratios are given.*

to a respectively low quantity of nitrogen and vice versa (on Rh, Ni and Pd). This can be due to extra exposure to borazine (caused by an unstable leak valve) or changes induced by a prolonged x-ray or UV radiation as found from the history of the data.

Published data for *h*-BN on Ni(111) [85, 87] demonstrated that *h*-BN forms a stoichiometric BN monolayer on Ni(111), which is in contrast with the present B rich films. Nevertheless the absolute values of 1 ML for the B and N coverage on Ni and Pd [85] agree well with those publications. For *h*-BN on Ru(0001) the value here calculated is smaller than the 1.16 ML given by Paffet et al. [81]. Our resulting low value (<1 ML) might suggest that in our calculation there is a systematic error that leads to this underestimation, for example due to the XPD correction factor. Data published earlier [18], based on the analysis of a few *h*-BN on Rh(111) preparations, claimed that the BN coverage is 1.5 ML and the film is stoichiometric. This result has been obtained by a data analysis in which Eq. 40 has been even more simplified taking the atomic density ratios and the transmission ratios equals to 1. This approximation leads to coverages 20% heigher than the one correctly calculated in the present analysis (see Table (8)). In this way without considering the product of the atom densities and transmission ratios the results of method (i) would become 1.33 ML for N on Rh(111) and 1.44 ML for B. The analysis of these XPS data leads to the conclusion that *h*-BN forms a single layer on the four different surfaces (with $<$ 120 L $(HBNH)_3$ exposure).

7.2.2 Direct comparison of XPS data

The data analysis reported so far is based on many approximations in the parameters needed in the theoretical models used (e.g. the inelastic mean free path values, the surface atomic densities or the analyzer transmission). A second set of experiments has been done in order to minimize as much as possible systematic errors induced by these

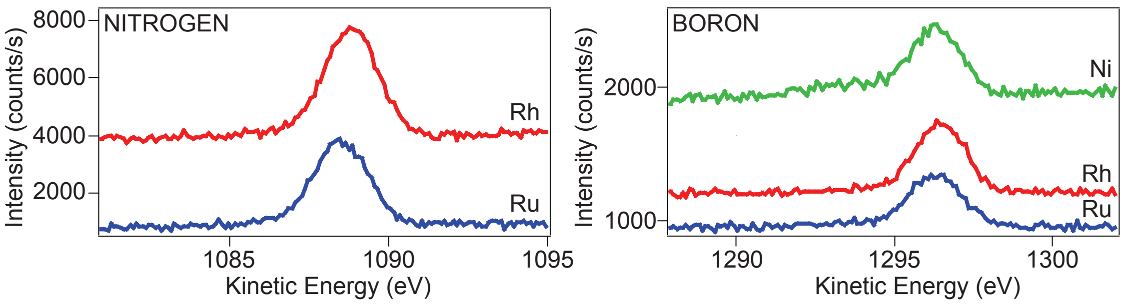

Figure 63: *N 1s (left) and B 1s (right) peaks measured with Al Kα (hν=1486.6 eV) excitation source for h-BN on Rh(111), Ni(111) and Ru(0001). The N 1s peak for the h-BN on Ni(111) has not been measured due to the unstable behavior of the source.*

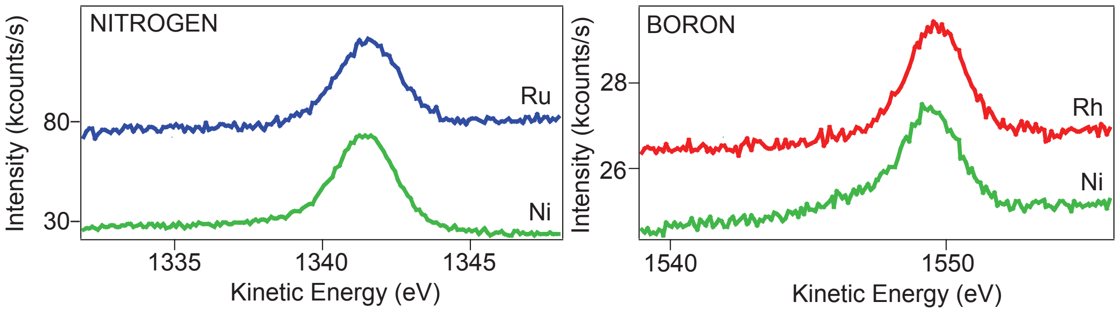

Figure 64: *N 1s (left) and B 1s (right) peaks measured with Si Kα (hν=1740 eV) excitation source for h-BN on Rh(111), Ni(111) and Ru(0001). The N 1s peak for the h-BN on Rh(111) and the B 1s h-BN on Ru(0001) are not shown because they are overlapped by other 'ghost' peaks.*

factors. The total intensities of the N 1s and of the B 1s for h-BN on Ni(111), on Rh(111) and on Ru(0001), all prepared within a few hours, were measured in the same day under the same experimental conditions. The experiment was done twice: once using Al Kα as photoelectron excitation source and once using Si Kα, in order to discard again errors due to the instability of the source during the measurements. Between the measurement of each sample, a spectrum of the 3d peaks of a Ag polycrystal was taken with the purpose of monitor such instabilities that eventually appeared.

In Fig. 63 the different N 1s and B 1s spectra are shown, measured with Al Kα ($h\nu = 1486.6\,\text{eV}$) radiation. The peak intensity (i.e. the area below the curve) has been taken in the range of $1290 - 1299\,\text{eV}$ for the B 1s and $1083 - 1092\,\text{eV}$ for the N 1s. The source was not stable during the experiment so that it was not possible to measure the intensity of the N 1s in h-BN/Ni(111) (the last peak of the series). Each peak has been

	B1s (Al Kα)	B1s (Si Kα)	N1s (Al Kα)	N1 (Si Kα)
Rh/Ni	1.00	1.08		
Ru/Ni	1.05			0.83
Rh/Ru	0.95		1.04	

Table 9: *Intensity ratio of the B 1s and of the N 1s peaks for h-BN on the substrates indicated in the first column. The values are given for the two experiments performed with the Al Kα and Si Kα sources. The error bar for the ratio is ±0.1 mainly due to the variation induced by the integration range.*

normalized with the area of the Ag 3d peaks calculated for the moment at which each spectrum was measured in order to compensate for the instrumental drift. The ratio N 1s σ_{Boron}/B 1s $\sigma_{Nitrogen}$ for *h*-BN on Ru(0001) is 0.9 and for *h*-BN on Rh(111) is 0.97. For the second experiments with Si Kα ($h\nu = 1740\,\mathrm{eV}$) radiation, the source was very stable and the intensity of the Ag 3d peaks remained always constant (within 1%). Therefore the intensity of the N 1s and of the B 1s peaks was not normalized. Due to the presence of 'ghost' lines in the spectra (i.e. replica of some peaks due to excitations sources different than Si Kα) the B 1s for *h*-BN on Ru(0001) and the N 1s for *h*-BN on Rh(111) were overlapped by other peaks and therefore it was not possible to extract their intensities, the other peaks are shown in Fig. 64. The integration range chosen for the B 1s is $1544 - 1554\,\mathrm{eV}$, and for the N 1s it is $1333 - 1346\,\mathrm{eV}$. The film on Ni(111) is stoichiometric with a ratio N 1s σ_{Boron}/B 1s $\sigma_{Nitrogen}$ of 1.02. The experiment has not been repeated with Mg Kα radiation ($h\nu = 1253.6\,\mathrm{eV}$) because also in that case not all the peaks can be measured (the N 1s for *h*-BN/Ni(111) is overlapped by some Auger lines). The results of the direct comparison of the absolute values of the intensities in the two experiments is shown in Table (9). The values that could be found in the two experiments suggest that the quantity of B and N in the *h*-BN films grown on the three surfaces is the same. Therefore, since it is known that for the *h*-BN/Ni(111) a single layer is formed on the surface, then it can be concluded that also from XPS studies 1.0±0.2 ML of *h*-BN is found on Rh(111) and on Ru(0001).

7.2.3 Peak positions and FWHM

Besides the values of the coverages, interesting hints on the features of these different *h*-BN structures come from the analysis of the N 1s and B 1s peak positions and their full-width-half-maximum (FWHM). The binding energies of N 1s (E_B(N 1s)) and B 1s (E_B(B 1s)) are reported in Table (10) with the values referred to the Fermi level and to the vacuum level. The first are shown in Fig. 65. Particular care has been taken in the

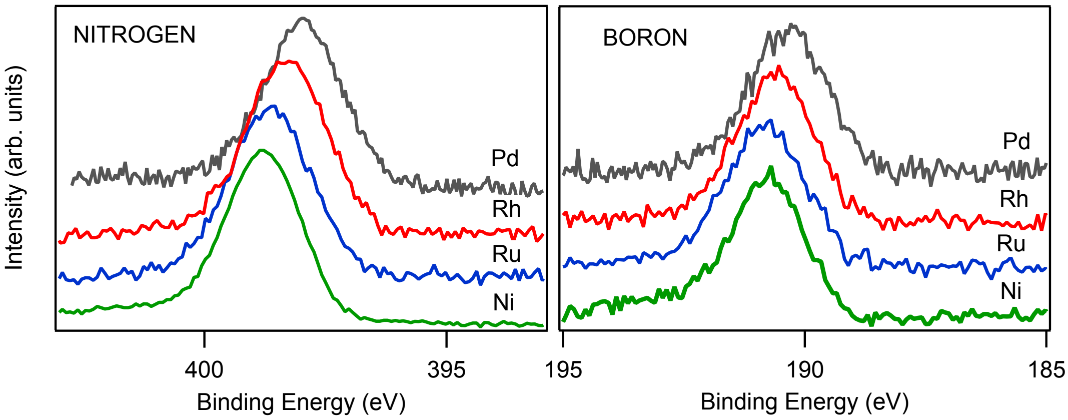

Figure 65: *N 1s (left) and B 1s (right) peaks measured with Al Kα radiation for h-BN on Rh(111), Ru(0001), Ni(111) and Pd(111) and referred to the Fermi level.*

	Φ_{hBN}	E_B^F(N 1s)	E_B^V(N 1s)	E_B^F(B 1s)	E_B^V(B 1s)
Rh(111)	4.15 ± 0.10	398.30 ± 0.16	402.32 ±0.10	190.65 ± 0.24	194.37 ± 0.13
Ru(0001)	4.00 ± 0.10	398.63 ± 0.15	402.31 ±0.10	190.83 ± 0.15	194.72 ± 0.10
Ni(111)	3.53 ± 0.10	398.79 ± 0.20	402.63±0.12	190.84 ± 0.15	194.83± 0.10
Pd(111)	4.26 ± 0.10	398.05 ± 0.27	402.45±0.14	190.46 ± 0.25	194.80 ± 0.13

Table 10: *Summary of the values for the binding energy (E_B) of N 1s and B 1s peaks on the h-BN on the different substrates. All the values are measured in eV and are referred either to the Fermi level E_B^F, either to the vacuum level E_B^V using the values of the work function of the h-BN covered substrates given in the first column. The errors are twice the standard deviation of the data.*

correct calibration of the peak positions with our spectrometer. The binding energy of both N 1s and B 1s for each BN system referred to the Fermi level shifts in going from one substrate to the other, and in particular it decreases by 0.74 ± 0.17 eV for N 1s and 0.38 ± 0.15 eV for B 1s in going from Ni(111) to Pd(111). While the position of N 1s and B 1s is very similar for h-BN on Ni(111) and on Ru(0001), it moves to smaller values for Rh (0.49 ± 0.13 eV for N 1s and 0.19 ± 0.14 eV for B 1s). If one aligns the peaks to the vacuum level, then Ni has highest values, followed by Pd and Ru and Rh.

Besides the analysis of the binding energies, also the FWHM of the N 1s and B 1s peaks have been considered. They are shown in Table (11) and in Fig. 66. The FWHM is calculated as the value given by Gaussian fits of the peaks, taking into account also the asymmetric peak-tales mostly present in the B 1s peak on Ni. The N 1s and B 1s peaks on Rh and Ru are ∼ 200 meV and ∼ 150 meV broader than on Ni, suggesting that on

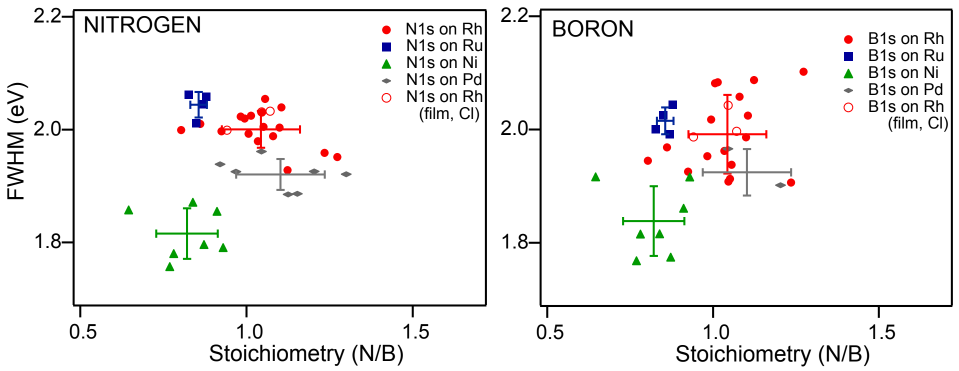

Figure 66: *FWHM of the N 1*s *(left) and B 1*s *(right) for h-BN on Rh(111), Ru(0001), Ni(111) and Pd(111) plotted versus the corresponding stoichiometry. The error bars in the mean values are the standard deviation of the data.*

	FWHM N 1s	FWHM B 1s
Rh(111)	2.00 ± 0.07	1.99 ± 0.14
Ru(0001)	2.04 ± 0.05	2.02 ± 0.05
Ni(111)	1.82 ± 0.09	1.84 ± 0.12
Pd(111)	1.92 ± 0.06	1.92 ± 0.08

Table 11: *Summary of the values of the FWHM for the N 1*s *and B 1*s *peaks on the h-BN on the different substrates in the first column. All the values are measured in eV. The errors are twice the standard deviation of the data.*

the nanomesh different N and B species are present.

8 Nanomesh properties

8.1 Different precursors and substrates

The possibility to tailor the nanomesh with desired properties in order to induce particular functionalities can follow different directions. On one side one could try to change the mesh once it is already formed on a surface. On the other side one can choose to grow it in a different way: either using substrates with different lattice mismatches (to change the hole size) or with a particular surface symmetry (to change the hole shape) (Ir(111), Rh(110) or metal-alloys are suitable future candidates) or using alternative precursors than borazine. In the latter possibility the chemical nature of the atomic species involved in the layer growth could change the bonding properties. So far this research has been focused on *h*-BN layers produced on different metals exposed to borazine. Now the possibility to use B-trichloroborazine $(ClBNH)_3$ to grow the nanomesh is briefly addressed.

8.2 Synthesis of the nanomesh from B-Trichloroborazine

B-trichloroborazine $(ClBNH)_3$ has been chosen because it is a compound easier to handle than borazine. In its equilibrium form at RT it is a white solid while borazine is liquid and highly reactive with air and water. In a B-trichloroborazine molecule the B atoms in the six-member ring are bonded to Cl atoms instead of H as for the borazine, thus this molecule could introduce new features in the *h*-BN assembly. In order to grow *h*-BN films from this precursor, as already done for *h*-BN on Ni(111) [136], pure B-trichloroborazine crystals were inserted in a glass tube directly connected to a leak valve mounted on the UHV chamber. The glass tube was evacuated by an auxiliary turbomolecular pump. The crystals were heated until some of them were melted ($\sim 350\,\mathrm{K}$). When the vapor phase is monitored by a quadrupole mass spectrometer upon opening the leak valve, just after melting, a lot of HCl (mass 36) but no B-trichloroborazine (mass 183) appears in the mass spectrum. Only after pumping away the HCl from the tube, mass 183 is present in an amount high enough to produce boron nitride films.

After this procedure, the exposure to 40 L of $(ClBNH)_3$ of a clean Rh(111) surface at 1050 K leads to the formation of a nanomesh as the one grown with $(HBNH)_3$. The STM images (as in Fig. 67(a)) and the LEED patterns (as in Fig. 67(b)) reveal virtually the same structure. No indications for Cl atoms in the mesh are observed by STM and no Cl peaks appear in XPS (a Cl concentration below 5% of a monolayer is estimated).

UP spectra taken in normal emission show the same *h*-BN bands in both cases and they are at the same positions, as shown in the plot in Fig. 68(a). ARUPS measurements

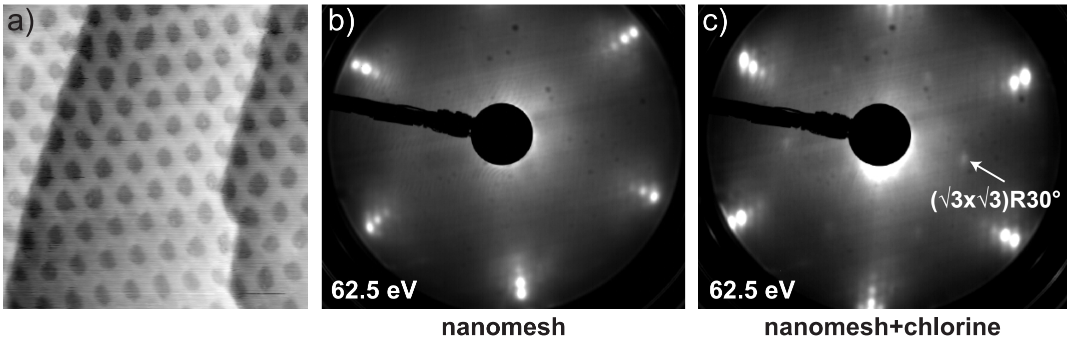

Figure 67: *(a) Constant current STM image (30×30 nm^2, I_t=1 nA, V_s=-2 V) of h-BN on Rh(111) grown using (ClBNH)$_3$ instead of (HBNH)$_3$. Three different terraces can be seen. (b) is the LEED pattern of the structure in (a) recorded at 62.5 eV. (c) LEED picture belonging to another h-BN preparation showing the presence of two superstructures: the nanomesh and the ($\sqrt{3} \times \sqrt{3}$)R30° of Cl (or HCl) (as indicated).*

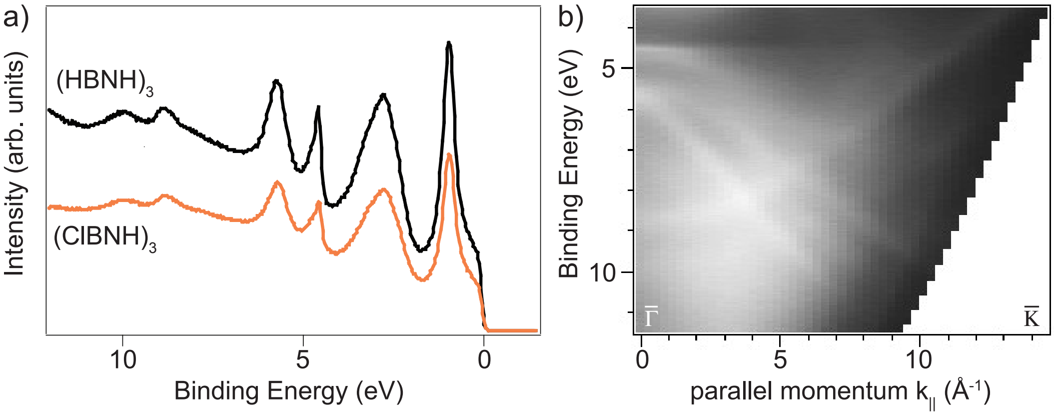

Figure 68: *(a) Normal emission He Iα excited UP spectra of h-BN/Rh(111) grown with (ClBNH)$_3$ and (HBNH)$_3$. The two spectra present the same features. (b) High resolution angle resolved dispersion plot measured along the azimuth $\overline{\Gamma K}$ for h-BN/Rh(111) grown using (ClBNH)$_3$. This can be directly compared with the one shown in Fig. 29(b). No new bands arise with the use of this alternative Cl containing precursor.*

taken along the azimuth $\overline{\Gamma \mathrm{K}}$ show the same dispersion of the σ and π bands (Fig. 68(b) and Fig. 29(b) can be directly compared). However, depending on the quantity of HCl present in the glass tube just before exposure, it is possible to obtain either chlorine adsorbate structures (($\sqrt{3} \times \sqrt{3}$)R30° or ($2\sqrt{3} \times 2\sqrt{3}$)R30°) alone or coexisting with the nanomesh (but not within the nanomesh). The LEED pattern in Fig. 67(c), shows a

$(\sqrt{3}\times\sqrt{3})$R30° periodicity due to the Cl (or HCl) and the nanomesh superlattice spots. It seems that the Cl (or HCl) superstructure is located on separate terraces. In fact in LEED it is observed only at some sample locations (it is not always present if the sample is moved under the LEED screen), and in STM images areas without mesh are found, but no Cl superstructures nor domain boundaries were clearly resolved. Moreover, it has been found in previous studies that Cl adsorbed on a clean Rh(111) [152] and on some other *fcc* metals forms a $(\sqrt{3}\times\sqrt{3})$R30° superstructure [153].

A drawback in the use of the B-trichloroborazine as a precursor is the high amount of HCl gas which is released upon formation of the *h*-BN layer. Even if it is no harm for standard UHV systems, the vacuum recovers much more slowly compared to when borazine is used.

8.3 Nanomesh stability

An important aspect for the application of the nanomesh as a template for regular nanostructures, or as a functional surface for nanocatalysis or biocatalysis, is its stability in various environments. Experiments were done to test at first the stability of the nanomesh to air exposure. A nanomesh prepared in UHV has been exposed to air for 60 hours. Once reintroduced in UHV the status of the structure has been checked with different techniques. In XPS spectra the N 1*s*, B 1*s*, C 1*s* and O 1*s* peaks were detected as shown in Fig. 69.

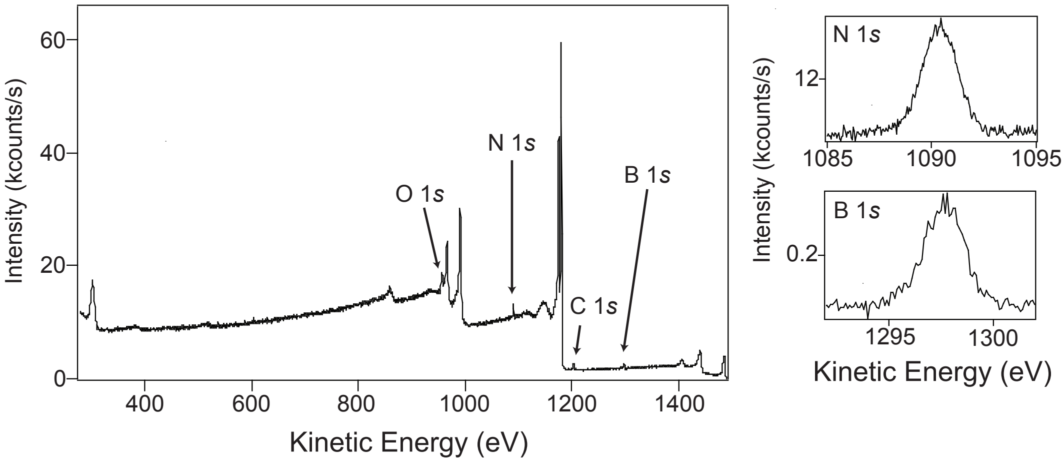

Figure 69: *XPS spectra measured with Al Kα radiation of the h-BN/Rh(111) after 60 hours air exposure. Clearly the B 1s and the N 1s peaks are resolved, indicating that BN is still present on the surface. The spectra measured at the kinetic energies of these two species are shown in detail on the right. C 1s and O 1s are the major contaminants detected on the surface.*

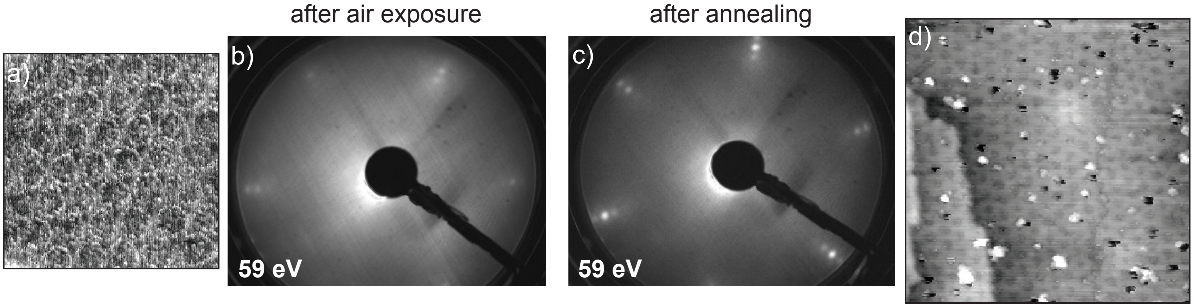

Figure 70: *The h-BN/Rh(111) nanomesh is stable under ambient conditions. It survived the exposure to air for 60 hours as demonstrated by STM (a) (20×20 nm^2, I_t=1 nA, V_s=-1 V) and LEED images (b). A short annealing up to 950 K is enough to remove a consistent part of the contaminants from the surface (as H_2O, O_2, CO_2 and CO) and bring the nanomesh almost back to its initial (pre-air exposure) configuration, as shown in the LEED image (b) and in the STM image (d) (45×45 nm^2, I_t=1 nA, V_s=-1 V).*

LEED and STM images (Fig. 70(a) and (b)) clearly show that not only was BN remaining on the surface but the nanomesh structure survived. A short annealing up to 950 K is enough to remove the major part of the contaminants. The species desorbing from the surface were monitored by a quadrupole mass spectrometer. At 400 K H_2O molecules were detected, from 700 to 870 K CO_2 and from 660 to 950 K CO. LEED patterns taken after the annealing show again sharp spots as from a freshly prepared mesh (Fig. 70(c)) while in STM images some contaminants can still be found (Fig. 70(d)). They appear on the surface as randomly distributed bright features with different sizes. The nanomesh is also still present on the surface if the annealing is done at 1100 K. SXRD experiments at the Swiss-Light-Source gave a further confirmation that the nanomesh was stable under prolonged air exposure to ambient atmosphere and X-ray radiation [101].

9 Conclusions and outlook

In this thesis the structural and electronic properties of different hexagonal boron nitride (*h*-BN) nanostructures, grown on the high symmetry surfaces of some transition metals, have been measured with high accuracy. The combined information obtained with several experimental techniques allowed to understand them in detail. The binding energy to the substrate and the lattice mismatch are the main responsible for the self-assembly of the *h*-BN on these surfaces, leading to different growth regimes. In the case of a single layer of *h*-BN on Ni(111) the compressive lattice mismatch between the *h*-BN and the substrate is very small (only +0.6%), therefore the *h*-BN grows pseudomorphic and slightly buckled on the surface. Here this system is only studied with the XPD technique in view of new experimental data, but it was already the object of previous work [63].

In the case of *h*-BN on Pd(111) the tensile lattice mismatch is very large (-9.7%). Theoretical calculations predict that the binding energy of *h*-BN on this surface is around 0.2 eV per BN unit and not strong enough to force the *h*-BN layer to a strained pseudomorphic growth. Therefore, the *h*-BN maintains its own structure, lies flat on the surface and is only physisorbed on this metal. Different rotated domains are found on the surface, appearing as Moiré patterns in STM images and as rings in LEED pictures. This system is well described also in comparison to the similar case of *h*-BN on Pd(110). While on the (111) surface a preferential coincidence lattice is formed, with (11×11) *h*-BN units grown on (10×10) Pd unit cells, on the (110) the *h*-BN layer is completely incommensurate.

The main result of this thesis is the discovery of a peculiar *h*-BN nanostructure that forms on Rh(111) and on Ru(0001). *h*-BN grows commensurate on these surface, a coincidence lattice with a periodicity of (12×12) substrate units is found. We call this nanostructure 'nanomesh' since it appears as a network at the nanoscale with its 3.2 nm periodicity, 2 nm hole size and 1.2 nm wire thickness. Low temperature STM measurements allowed to resolve its structure at the atomic level. In the nanomesh no real holes are present, no bare Rh surface is exposed to the vacuum but the appearance of 'holes' is due to the corrugation of the *h*-BN layer. The Rh(111) and the Ru(0001) are very similar surfaces and the tensile lattice mismatch with *h*-BN is -7%. On these substrates the bonding between the B and N atoms is stronger (~ 0.3 eV and ~ 0.6 eV, respectively) than on Ni and Pd. Therefore the system is characterized by locally chemisorbed areas (the nanomesh holes) where the mismatch is minimized, and by strained regions (the nanomesh wires) less bonded to the substrate. Even if the nanomeshes grown on Rh(111) and Ru(0001) exhibit the same properties, the one on Rh shows a higher degree of long-range order.

A direct comparison between the *h*-BN nanostructures grown on several hexagonal surfaces, examined in this thesis, is given with respect to their valence band structure measured with UPS and the quantification of the *h*-BN coverage from XPS data.

The nanomesh can be used as template to organize molecules, as demonstrated with the decoration experiments with C_{60} molecules, or to grow regularly spaced arrays of nanoclusters. Since it is stable in air and at high temperatures (up to 1100 K, at least) it can be seen as promising nanostructure for future applications in nanoelectronics, nanocatalysis and whenever an insulating patterned film on a metal surface is needed. Therefore, in view of a possible nanomesh mass production, it is demonstrated that the same nanomesh can be easily grown by chemical vapor deposition with different precursors (here borazine and B-trichloroborazine have been used) and not only on costly single crystals but also on less expensive crystalline thin films that are easy to handle.

A *h*-BN on Ir(111)

In the search for alternative substrates to grow the nanomesh, also iridium thin films grown on $Al_2O_3(0001)$ have been exposed to borazine. The tensile lattice mismatch with *h*-BN is $\sim -7.7\%$, again similar to the one for Rh and Ru. The resulting *h*-BN structure is still under investigation. The films were cleaned with the same procedure as used for the Rh ones (outgassing in UHV followed by cycles of Ar^+ sputtering, oxidation and annealing). The quality of the films was investigated with different techniques. The XPD and LEED patterns show a six-fold periodicity due to the *fcc* and *hcp* type of domains coexisting on the surface, as found also on the Rh(111), Ru(0001) and Pd(111) crystalline films.

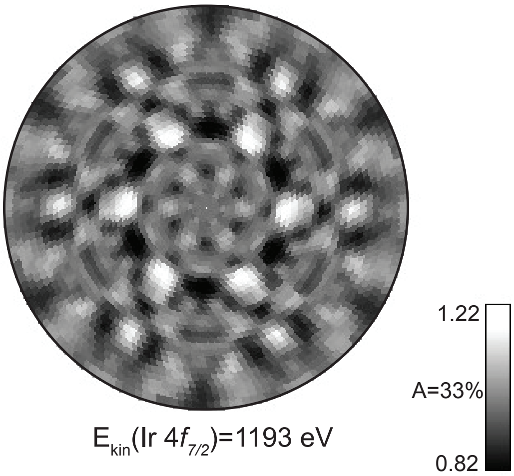

Figure 71: *XPD pattern for clean Ir(111). Ir 4f pattern measured at 1193 eV kinetic energy with Mg kα as photoelectrons excitation source. The pattern is shown in stereographic projection.*

In Fig. 71 a XPD pattern measured for the clean Ir(111) surface at 1193 eV kinetic energy, corresponding to the emission line of the Ir $4f_{7/2}$, is shown. This six-fold symmetry is caused by the twinned growth of the metal substrate, where both ABC and ACB stacking of the atomic planes is found on the surface. The cleanliness of the sample has been assured by XPS measurements on the bare surface, by the presence of sharp Ir spots present in LEED images and by STM where terraces with different sizes appeared (8 to 60 nm). *h*-BN layers were grown exposing to $\sim$ 40 L of $(HBNH)_3$ (i.e. $3 \cdot 10^{-7}$ mbar for 3 min) the hot (1050 K) Ir(111) followed by 1 min of post-annealing at the same temperature. Preliminary experiments show that the Ir(111) surface is covered by *h*-BN units (as measured with XPS). LEED pictures (as Fig. 72(a)) show diffuse coincidence lattice spots around the principal ones with periodicity (12.5×12.5)±0.5 Ir lattice units (measured around the (0, 1) and the (-1, 1) Ir principal lattice spots). In STM images an overstructure with different periodicities between 1.4 and 2.6 nm is seen (Fig. 72(b) and (c)). The corrugation varies from 0.5 to 1.0 Å. If this structure would be a nanomesh

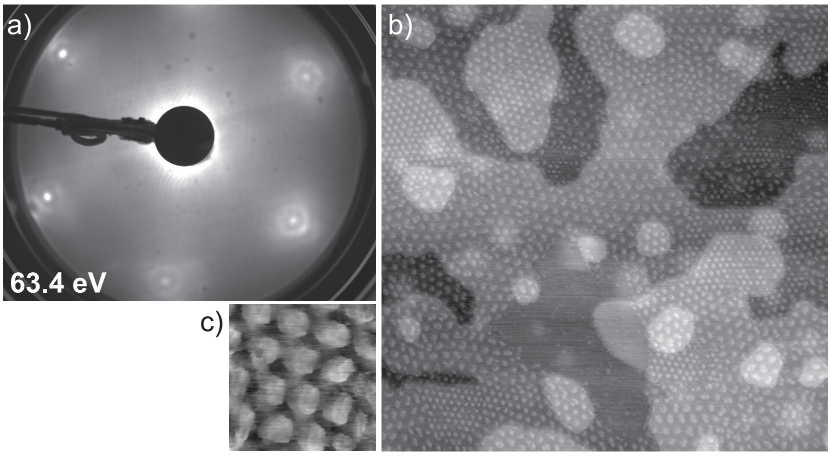

Figure 72: *(a) LEED pattern of h-BN on a Ir(111) film grown on* Al_2O_3*(0001) recorded at 63.4 eV. (b) Constant current STM image of the same structure (100×100* nm^2*,* I_t*=1 nA,* V_s*=1 V). Different terraces appear, covered by a hexagonal superstructure with different periodicities. It resembles a disordered nanomesh measured with reversed contrast. In the image an area uncovered by h-BN is also present. (c) Highly resolved constant current STM image of the same structure for another preparation (10×10* nm^2*,* I_t*=0.5 nA,* V_s*=0.5 V).*

then most of the STM images were recorded (at positive and negative voltages) in the reversed contrast (holes seen as protrusions) suggesting therefore a different density of states for this system with respect to the nanomesh on Rh(111) and on Ru(0001), where usually the pores are imaged as depressions, but both contrasts are occasionally visible. Also the 'usal' nanomesh contrast for the *h*-BN on Ir(111) was rarely observed. The different periodicites would then be due to a disordered mesh, perhaps caused by an annealing temperature too low for the system for better self-assembly. Another possibility is that not a nanomesh but different Moiré patterns in domains with several periodicities (as in the case of *h*-BN on Pd(111) or graphite on Ru(0001)) are imaged. Nevertheless, in normal emission UP spectra there is not an intense single σ band as for *h*-BN on Ni(111) and Pd(111), but two bands similar to σ_α and σ_β, suggesting that the electronic structure is close to the one of the nanomesh (Fig. 73). The value found for the work function of the clean Ir(111) surface is $\sim 5.12 \pm 0.10\,\mathrm{eV}$, for Ir covered with *h*-BN it is reduced to $\sim 4.5 \pm 0.1\,\mathrm{eV}$. At $\overline{\Gamma}$ three states are observed for *h*-BN/Ir(111), which are found at binding energies: $E_B(\sigma_\alpha) = 4.4 \pm 0.10\,\mathrm{eV}$, $E_B(\sigma_\beta) = 5.7 \pm 0.1\,\mathrm{eV}$, $E_B(\pi_\alpha) = 8.46 \pm 0.10\,\mathrm{eV}$. If aligned to the vacuum level, the binding energies are: $E_B^V(\sigma_\alpha) = 8.9 \pm 0.10\,\mathrm{eV}$, $E_B^V(\sigma_\beta) = 9.97 \pm 0.10\,\mathrm{eV}$, $E_B^V(\pi_\alpha) = 12.96 \pm 0.10\,\mathrm{eV}$. Also in this case σ_α aligns to the vacuum level with the same value as all the other σ bands of the *h*-BN on the different transition-metal hexagonal surfaces. It should be noted

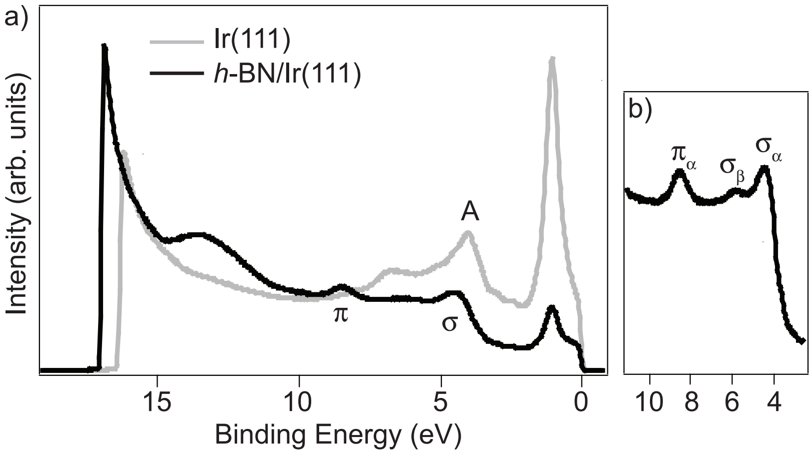

Figure 73: *He Iα normal emission UP spectra for clean Ir(111) film grown on* Al_2O_3*(0001) and covered with h-BN. On the right a spectrum measured around the h-BN bands. Two* σ *(*σ_α*,* σ_β*) and one* π *bands are visible.*

that the σ_α band is close to a broad Ir band (labeled A in Fig. 73) for the clean surface (FWHM $\sim$ 1.15 eV) centered at $\sim$ 4 eV. It is still unclear why only one π band is observed from the *h*-BN layer (the π_α) and not two. ARUPS experiments will be done in order compare the resulting band structure measured along $\overline{\Gamma K}$ and $\overline{\Gamma M}$ with those known for the other *h*-BN systems where one single layer or two layers are present in order to shed light on this interesting system. Useful information will also be obtained from highly resolved measurements of the N 1*s* and B 1*s* XPD patterns.

References

[1] J. Zhang, Z. Wang, J. Liu, S. Chen, and G. Liu, *Self-Assembled Nanostructures*, Kluwer Academic Publishers, New York, 2003.

[2] Y. Xia, J. A. Rogers, K. E. Paul, and G. M. Whitesides, *Unconventional Methods for Fabricating and Patterning Nanostructures*, Chem. Rev. **99**, 1823 (1999).

[3] T. Ito and S. Okazaki, *Pushing the limits of lithography*, Nature (London) **406**, 1027 (2000).

[4] K. Deguchi and T. Haga, *Proximity X-ray and extreme ultraviolet lithography*, C. R. Acad. Sci. Paris, t. 1, **4**, 829 (2000).

[5] P. Vettiger, G. Cross, M. Despont, U. Drechsler, U.Dürig, B. Gotsmann, W. Häberle, M. A. Lantz, H. E. Rothuizen, R. Stutz, and G. K. Binnig, *The 'millipede'–nanotechnology entering data storage*, IEEE Trans. Nanotechnol. **1**, 39 (2002).

[6] B. D. Gates, Q. Xu, J. C. Love, D. B. Wolfe, and G. M. Whitesides, *Unconventional Nanofabrication*, Annu. Rev. Mater. Res. **34**, 339 (2004).

[7] H. Kind, J.-M. Bonard, C. Emmenegger, L.-O. Nilsson, K. Hernadi, E. Millard-Schaller, L. Schlapbach, L. Forró, and K. Kern, *Patterned Films of Nanotubes Using Microcontact Printing of Catalysts*, Adv. Mater. **11**, 1285 (1999).

[8] S. J. Tans, A. R. M. Verschueren, and C. Dekker, *Room-temperature transistor based on a single carbon nanotube*, Nature (London) **393**, 49 (1998).

[9] Ph. Avouris, R. Martel, V. Derycke, and J. Appenzeller, *Carbon nanotube transistors and logic circuits*, Physica B **323**, 6 (2002).

[10] B.-K. Kim, N. Park, P. S. Na, H.-M. So, J.-J. Kim, H. Kim, K.-J. Kong, H. Chang, B.-H. Ryu, Y. Choi, and J.-O Lee, *The effect of metal cluster coatings on carbon nanotubes*, Nanotechnol. **17**, 496 (2006).

[11] N. Bowden, S. Brittain, A. G. Evans, J. W. Hutchinson, and G. M. Whitesides, *Spontaneous formation of ordered structures in thin films of metals supported on an elastomeric polymer*, Nature (London) **391**, 146 (1998).

[12] S. A. Jenekhe and X. L. Chen, *Self-Assembly of Ordered Microporous Materials from Rod-Coil Block Copolymers*, Science **283**, 372 (1999).

[13] G. Stix, *Innovations: Nano Patterning*, Sci. Am. (2004).

[14] R. lmbihl and G. Ertl, *Oscillatory Kinetics in Heterogeneous Catalysis*, Chem. Rev. **95**, 697 (1995).

[15] J. V. Barth, G. Costantini, and K. Kern, *Engineering atomic and molecular nanostructures at surfaces*, Nature (London) **437**, 671 (2005).

[16] Z. Zhang and M. G. Lagally, *Atomistic Processes in the Early Stages of Thin-Film Growth*, Science **276**, 377 (1997).

[17] H. Röder, E. Hahn, H. Brune, J. Bucher, and K. Kern, *Building one- and two-dimensional nanostructures by diffusion-controlled aggregation at surfaces*, Nature (London) **366**, 141 (1993).

[18] M. Corso, W. Auwärter, M. Muntwiler, A. Tamai, T. Greber, and J. Osterwalder, *Boron Nitride Nanomesh*, Science **303**, 217 (2004).

[19] S. Berner, M. Corso, R. Widmer, O. Gröning, R. Laskowski, P. Blaha, K. Schwarz, A. Goriachko, H. Over, S. Gsell, M. Schreck, H. Sachdev, T. Greber, and J. Osterwalder, *Boron Nitride Nanomesh: Functionality from a Corrugated Monolayer*, Angew. Chem. Int. Ed. **46**, 5115 (2007).

[20] W. Chen, K. P. Loh, H. Xu, and A. T. S. Wee, *Nanoparticle Dispersion on Reconstructed Carbon Nanomesh*, Langmuir **20**, 10779 (2004).

[21] H. Brune, M. Giovannini, K. Bromann, and K. Kern, *Self-organized growth of nanostructure arrays on strain-relief patterns*, Nature (London) **394**, 451 (1998).

[22] J. A. Theobald, N. S. Oxtoby, M. A. Phillips, N. R. Champness, and P. H. Beton, *Controlling molecular deposition and layer structure with supramolecular surface assemblies*, Nature (London) **424**, 1029 (2003).

[23] W. Chen, H. Xu, L. Liu, X. Gao, D. Qi, G. Peng, S. C. Tan, Y. Feng, K. P. Loh, and A. T. S. Wee, *Atomic structure of the 6H-SiC(0001) nanomesh*, Surf. Sci. **596**, 176 (2005).

[24] C. Berger, Z. Song, T. Li, X. Li, A. Y. Ogbazghi, R. Feng, Z. Dai, A. N. Marchenkov, E. H. Conrad, P. N. First, and W. A. de Heer, *Ultrathin Epitaxial Graphite: 2D Electron Gas Properties and a Route toward Graphene-based Nanoelectronics*, J. Phys. Chem. B **108**, 19912 (2004).

[25] G. Binnig and H. Rohrer, *In touch with atoms*, Rev. Mod. Phys. **71**, 324 (1999).

[26] G. Binnig and H. Roher, *Scanning Tunneling Microscopy*, Helvetica Physica Acta **55**, 726 (1982).

[27] W. A. Hofer, *Challenges and errors: interpreting high resolution images in scanning tunneling microscopy*, Prog. Surf. Sci. **71**, 147 (2003).

[28] G. A. D. Briggs and A. J. Fisher, *STM experiment and atomistic modelling hand in hand: individual molecules on semiconductor surfaces*, Surf. Sci. Reports **33**, 1 (1999).

[29] C. J. Chen, *Introduction to Scanning Tunneling Microscopy*, Oxford University Press, 1993.

[30] J. Bardeen, *Tunneling from a many-partcle point of view*, Phys. Rev. Lett. **68**, 57 (1961).

[31] J. Tersoff and D. R. Hamann, *Theory of the scanning tunneling microscope*, Phys. Rev. B **31**, 805 (1985).

[32] C. J. Chen, *Origin of atomic resolution on metal surfaces in scanning tunneling microscopy*, Phys. Rev. Lett. **65**, 448 (1990).

[33] J. K. Gimzewsky and R. Möller, *Transition from the tunneling regime to point contact studied using scanning tunneling microscopy*, Phys. Rev. B **37**, 1284 (1987).

[34] U. Dürig, O. Züger, B. Michel, L. Häussling, and H. Ringsdorf, *Electronic and mechanical characterization of self-assembled alkanethiol monolayers by scanning tunneling microscopy combined with interaction-force-gradient sensing*, Phys. Rev. B **48**, 1711 (1993).

[35] K. Reuter, P. L. de Andres, F. J. Garcia-Vidal, F. Flores, and K. Heinz, *Surface and bulk band-structure effects on $CoSi_2$/Si(111) ballistic-electron emission experiments*, Phys. Rev. B **63**, 205325 (2001).

[36] A. Selloni, P. Carnevali, E. Tosatti, and C. D. Chen, *Voltage-dependent scanning-tunneling microscopy of a crystal surface: Graphite*, Phys. Rev. B **31**, 2602 (1985).

[37] M. R. Castell, P. L. Wincott, N. G. Condon, C. Muggelberg, G. Thornton, S. L. Dudarev, A. P. Sutton, and G. A. D. Briggs, *Atomic-resolution STM of a system with strongly correlated electrons: NiO(001) surface structure and defects sites*, Phys. Rev. B **55**, 7860 (1997).

[38] S. Schintke and W.-D. Schneider, *Insulators at the ultrathin limit: electronic structure studied by scanning tunneling microscopy and scanning tunneling spectroscopy*, J. Phys.: Condens. Matter **16**, 49 (2004).

[39] B. Michel, G. Travaglini, H. Rohrer, C. Joachim, and M. Amrein, *Images of crystalline alkanes obtained with scanning tunneling microscopy*, Z. Phys. B **76**, 99 (1989).

[40] J. Viernow, D. Y. Petrovykh, A. Kirakosian, J.-L. Lin, F. K. Men, M. Henzler, and F. J. Himpsel, *Chemical imaging of insulators by STM*, Phys. Rev. B **59**, 10357 (1999).

[41] W. Hebenstreit, J. Redinger, Z. Horozova, M. Schmid, R. Podloucky, and P. Varga, *Atomic resolution by STM on ultra-thin films of alkali halides: experiment and local density calculations*, Surf. Sci. **424**, L321 (1999).

[42] T. Jung, Y. W. Mo, and F. J. Himpsel, *Identification of Metals in Scanning Tunneling Microscopy via Image States*, Phys. Rev. Lett. **74**, 1641 (1995).

[43] M. Pivetta, F. Patthey, M. Stengel, A. Baldereschi, and W.-D. Schneider, *Local work function Moiré pattern on ultrathin ionic films: NaCl on Ag(100)*, Phys. Rev. B **72**, 115404 (2005).

[44] E. D. L. Rienks, N. Nilius, H.-P. Rust, and H.-J. Freund, *Surface potential of a polar oxide film: FeO on Pt(111)*, Phys. Rev. B **71**, 241404 (2005).

[45] K. Bobrov, A. J. Maine, and G. Dujardin, *Atomic-scale imaging of insulating diamond through resonant electron injection*, Nature (London) **431**, 616 (2004).

[46] J. Repp, S. Fölsch, G. Meyer, and K.-H. Rieder, *Ionic Films on Vicinal Surfaces: Enhanced Binding due to Charge Modulation*, Phys. Rev. Lett. **86**, 252 (2001).

[47] S. Hüfner, *Photoelectron Spectroscopy*, Springer, Berlin, 1995.

[48] F. Reinert and S. Hüfner, *Photoemission spectroscopy - from early days to recent applications*, New Journal of Physics **7**, 97 (2005).

[49] J. Osterwalder, *Fermi Surface Mapping by Photoemission*, Surf. Rev. Lett. **4**, 391 (1997).

[50] P. Aebi, J. Osterwalder, R. Fasel, D. Naumović, and L. Schlapbach, *Fermi surface mapping with photoelectrons at UV energies*, Surf. Sci. **307-309**, 917 (1994).

[51] R. Fasel and J. Osterwalder, *Alkali-metal adsorption geometries on metal surfaces from photoelectron-diffraction experiments*, Surf. Rev. Lett. **2**, 395 (1995).

[52] K. Siegbahn, C. Nordling, R. Fahlman, R. Nordberg, K. Hamrin, J. Hedman, G. Johansson, T. Bergmark, S. -E. Karlsson, I. Lindgren, and B. Lindberg, *ESCA, Atomic, Molecular and Solid State Structure Studies by Means of Electron Spectroscopy*, Nova Acta Regiae Soc. Sci., Upsaliensies, Ser. IV, Vol. 20, 1967.

[53] J. Osterwalder, *Structure determination by Angle-Scanned X-Ray Photoelectron Diffraction*, The Arabian Journal for Science and Engineering **15**, 273 (1990).

[54] J. Wider, T. Greber, E. Wetli, T.J. Kreutz, P. Schwaller, and J. Osterwalder, *Direct observation of subsurface oxygen on Rh(111)*, Surf. Sci. **417**, 301 (1998).

[55] P. A. Lee, *Possibility of adsorbate position determination using final-state interference effects*, Phys. Rev. B **13**, 5216 (1976).

[56] S. Kono, S. M. Goldberg, N. F. T. Hall, and C. S. Fadley, *Chemisorption geometry of c(2×2) oxygen on Cu(001) from angle-resolved core-level x-ray photoemission*, Phys. Rev. B **22**, 6085 (1980).

[57] J. B. Pendry, *Low Energy Electron Diffraction*, Academic Press, London, 1974.

[58] S. Y. Tong, H. C. Poon, and D. R. Snider, *Importance of multiple forward scattering in medium- and high-energy electron emission and/or diffraction spectroscopies*, Phys. Rev. B **32**, 2096 (1985).

[59] T. J. Kreutz, *The temperature dependent electronic structure of nickel metal*, PhD thesis, University of Zurich, 1997.

[60] T. Greber, O. Raetzo, T. J. Kreutz, P. Schwaller, W. Deichmann, E. Wetli, and J. Osterwalder, *A Photoelectron Spectrometer for k-Space Mapping Above the Fermi Level*, Rev. Sci. Instrum. **68**, 4549 (1997).

[61] F. Baumberger, *Electronic Surface States in Lateral Super-Structures*, PhD thesis, University of Zurich, 2002.

[62] T. J. Kreutz, T. Greber, P. Aebi, and J. Osterwalder, *Temperature-dependent electronic structure of nickel metal*, Phys. Rev. B **58**, 1300 (1998).

[63] W. Auwärter, *One monolayer of Hexagonal Boron Nitride on Ni(111): an Atomically Sharp Interface*, PhD thesis, University of Zurich, 2003.

[64] K. Watanabe, T. Taniguchi, and H. Kanda, *Direct-bandgap properties and evidence for ultraviolet lasing of hexagonal boron nitride single crystal*, Nature Mater. **3**, 404 (2004).

[65] V. L. Solozhenko, A. G. Lazarenko, J. P. Petitet, and A. V. Kanaev, *Bandgap energy of graphite-like hexagonal boron nitride*, J. Phys. Chem. Solids **62**, 1331 (2001).

[66] A. Lipp, K. A. Schwetz, and K. Hunold, *Hexagonal boron nitride: Fabrication, properties and applications*, J. Eur. Ceram. Soc. **5**, 3 (1989).

[67] H. Sueyoshi, N. T. Rochman, and S. Kawano, *Damping capacity and mechanical property of hexagonal boron nitride-dispersed composite steel*, J. Alloys Compounds **355**, 120 (2003).

[68] S. Watanabe, S. Miyake, and M. Murakawa, *Tribological properties of cubic, amorphous and hexagonal boron nitride films*, Surf. Coat. Technol. **49**, 406 (1991).

[69] J. Buodiombo, O. Baehr, A. Boudrioua, P. Thevenin, J. C. Loulergue, and A. Bath, *Modes of propagating light waves in thin films of boron nitride deposited by plasma enhanced chemical vapor deposition*, Mater. Sci. Eng. B **46**, 96 (1997).

[70] E. Benko, J. Morgiel, and T. Czeppe, *BN sintered with Al: microstructure and hardness*, Ceram. Int. **23**, 89 (1997).

[71] Y. Zhang, X. He, J. Han, and S. Du, *Combustion synthesis of hexagonal boron-nitride-based ceramics*, J. Mat. Proc. Tech. **116**, 161 (2001).

[72] C. Rohr, J. -H. Boo, and W. Ho, *The growth of hexagonal boron nitride thin films on silicon using single source precursor*, Thin Solid Films **322**, 9 (1998).

[73] N. Ooi, V. Rajan, J. Gottlieb, Y. Catherine, and J. B. Adams, *Structural properties of hexagonal boron nitride*, Modelling Simul. Sci. Eng. **14**, 515 (2006).

[74] V. L. Solozhenko, G. Will, and F. Elf, *Isothermal compression of hexagonal graphite-like boron nitride up to 12 GPa*, Solid State Commun. **96**, 1 (1995).

[75] C. Berger, Z. Song, X. Li, X. Wu, N. Brown, C. Naud, D. Mayou, T. Li, J. Hass, A. N. Marchenkov, E. H. Conrad, P. N. First, and W. A. de Heer, *Electronic Confinement and Coherence in Patterned Epitaxial Graphene*, Science **312**, 1191 (2006).

[76] C. A. Long and H. J. Grabke, *The formation of boron nitride on Fe-37Ni alloy*, Appl. Surf. Sci. **59**, 207 (1992).

[77] J. A. Rodriguez, C. M. Truong, and D. W. Goodman, *Molecular Precursors to Boron Nitride Thin Films. 1 Adsorption of Diborane on Ru(0001),* NH_3*/Ru(0001) and O/Ru(0001) Surfaces*, J. Phys. C: Solid State Phys. **96**, 334 (1992).

[78] C. M. Truong, J. A. Rodriguez, and D. W. Goodman, *Molecular Precursors to Boron Nitride Thin Films. 2 Coadsorption and Reaction of Hydrazine and Diborane on Ru(0001)*, J. Phys. C: Solid State Phys. **96**, 341 (1992).

[79] R. J. Simonson and M. Trenary, *An Infrared Study of the Adsorption of Borazine,* $(BHNH)_3$*, on the Pt(111) Surface*, J. Electron Spectr. Rel. Phen. **54**, 717 (1990).

[80] R. J. Simonson, M. T. Paffett, M. E. Jones, and B. E. Koel, *A vibrational study of borazine adsorbed on Pt(111) and Au(111) surfaces*, Surf. Sci. **254**, 29 (1991).

[81] M. T. Paffet, R. J. Simonson, P. Papin, and R. T. Paine, *Borazine adsorption and decomposition at Pt(111) and Ru(0001) surfaces*, Surf. Sci. **232**, 286 (1990).

[82] F. Müller, K. Stöwe, and H. Sachdev, *Symmetry versus Commensurability: Epitaxial Growth of Hexagonal Boron Nitride on Pt(111) From B-Trichloroborazine* $(ClBNH)_3$, Chem. Mater. **17**, 3464 (2005).

[83] J. -W. He and D. W. Goodman, *Interaction of borazine with a Re(0001) surface, studied by LEED, TDS, AES and ELS*, Surf. Sci. **232**, 138 (1990).

[84] A. B. Preobrajenski, A. S. Vinogradov, and N. Mårtensson, *Ni 3d-BN* π *hybridization at the h-BN/Ni(111) interface observed with core-level spectroscopies*, Phys. Rev. B **70**, 165404 (2004).

[85] A. Nagashima, N. Tejima, Y. Gamou, T. Kawai, and C. Oshima, *Electronic dispersion relations of monolayer hexagonal boron nitride formed on the Ni(111) surface*, Phys. Rev. B **51**, 4606 (1995).

[86] Y. Gamou, M. Terai, A. Nagashima, and C. Oshima, *Atomic Structural Analysis of a Monolayer Epitaxial Film of Hexagonal Boron Nitride/Ni(111) studied by LEED Intensity Analysis*, Sci. Rep. RITU A **44**, 211 (1997).

[87] W. Auwärter, T. J. Kreutz, T. Greber, and J. Osterwalder, *XPD and STM investigation of hexagonal boron nitride on Ni(111)*, Surf. Sci. **429**, 229 (1999).

[88] G. B. Grad, P. Blaha, K. Schwarz, W. Auwärter, and T. Greber, *Density functional theory investigation of the geometric and spintronic structure of h-BN/Ni(111) in view of photoemission and STM experiments*, Phys. Rev. B **68**, 085404 (2003).

[89] M. N. Huda and L. Kleinman, *h-BN monolayer adsorption on the Ni(111) surface: A density functional study*, Phys. Rev. B **74**, 075418 (2006).

[90] A. Nagashima, N. Tejima, Y. Gamou, T. Kawai, and C. Oshima, *Electronic states of monolayer hexagonal boron nitride formed on the metal surfaces*, Surf. Sci. **357**, 307 (1996).

[91] A. Nagashima, N. Tejima, Y. Gamou, T. Kawai, and C. Oshima, *Electronic Structure of Monolayer Hexagonal Boron Nitride Physisorbed on Metal Surfaces*, Phys. Rev. Lett. **75**, 3918 (1995).

[92] A. B. Preobrajenski, A. S. Vinogradov, and N. Mårtensson, *Monolayer of h-BN chemisorbed on Cu(111) and Ni(111): The role of the transition metal 3d states*, Surf. Sci. **582**, 21 (2005).

[93] R. Desrosieres, D. W. Greve, and A. J. Gellman, *Nucleation of boron nitride thin films on Ni(100)*, Surf. Sci. **382**, 35 (1997).

[94] E. Rokuta, Y. Hasegawa, A. Itoh, K. Yamashita, T. Tanaka, S. Otani, and C. Oshima, *Vibrational spectra of the monolayer films of hexagonal boron nitride and graphite on faceted Ni(755)*, Surf. Sci. **427**, 97 (1999).

[95] M. K. Muntwiler, *Nanostructured Magnetic Interfaces: Case Studies and New Experiment Control Software*, PhD thesis, University of Zurich, 2004.

[96] T. Greber, L. Brandenberger, M. Corso, A. Tamai, and J. Osterwalder, *Single layer hexagonal boron nitride films on Ni(110)*, e-J. Surf. Sci. Nanotech. **4**, 410 (2006).

[97] A. Zangwill, *Physics at Surfaces*, Cambridge University Press, Cambridge, 1988.

[98] N.W. Ashcroft and N.D. Mermin, *Solid State Physics*, Saunders College (Philadelphia), 1976.

[99] E. K. Sichel, R. E. Miller, M. S. Abrahams, and C. J. Buiocchi, *Heat capacity and thermal conductivity of hexagonal pyrolytic boron nitride*, Phys. Rev. B **13**, 4607 (1976).

[100] E. Bertel, G. Rosina, and F. P. Netzer, *The structure of benzene on Rh(111): coadsorption with CO*, Surf. Sci. Lett **172**, 515 (1986).

[101] O. Bunk, M. Corso, D. Martoccia, R. Herger, P. R. Willmott, B. D. Patterson, J. Osterwalder, J. F. van der Veen, and T. Greber, *Surface X-Ray Diffraction Study of Boron-Nitride Nanomesh in Air*, Surf. Sci. Lett **601**, L7 (2007).

[102] M. Gsell, P. Jakob, and D. Menzel, *Effect of Substrate Strain on Adsorption*, Science **280**, 717 (1998).

[103] R. Hoffmann, C. Barth, A. S. Forster, A. L. Schluger, H. J. Hug, H.-J. Günterodt, R. M. Nieminem, and M. Reichling, *Measuring Site-Specific Cluster-Surface Bond Formation*, J. Am. Chem. Soc. **127**, 17863 (2005).

[104] R. Laskowski, P. Blaha, T. Gallauner, and K. Schwarz, *Single Layer Model of the Hexagonal Boron Nitride Nanomesh on the Rh(111) Surface*, Phys. Rev. Lett. **98**, 106802 (2007).

[105] H. Brune, H. Röder, C. Boragno, and K. Kern, *Strain relief at hexagonal-close-packed interfaces*, Phys. Rev. B **49**, 2997 (1994).

[106] C. Günther, J. Vrijmoeth, R. Q. Hwang, and R. J. Behm, *Strain Relaxation in Hexagonally Close-Packed Metal-Metal Interfaces*, Phys. Rev. Lett. **74**, 754 (1995).

[107] J. Jacobsen, L. P. Nielsen, F. Besenbacher, I. Stensgaard, E. Lægsgaard, T. Rasmussen, K. W. Jacobsen, and J. K. Nørskov, *Atomic-Scale Determination of Misfit Dislocation Loops at Metal-Metal Interfaces*, Phys. Rev. Lett. **75**, 489 (1995).

[108] R. Pushpa and S. Narasimhan, *Reconstruction of Pt(111) and domain patterns on close-packed metal surfaces*, Phys. Rev. B **67**, 205418 (2003).

[109] P. Bak, *Commensurate phases, incommensurate phases and the devil's staircase*, Rep. Prog. Phys. **45**, 587 (1982).

[110] S. Degen, A. Krupski, M. Kralj, A. Langner, C. Becker, M. Sokolowski, and K. Wandelt, *Determination of the coincidence lattice of an ultra thin Al_2O_3 film on $Ni_3Al(111)$*, Surf. Sci. Lett **576**, L57 (2005).

[111] R. D. Heidenreich and W. Shockley, *Report of a Conference on Strenght of Solids*, Physical Society, London, 1948.

[112] A. Nagashima, Y. Gamou, M. Terai, M. Wakabayashi, and C. Oshima, *Electronic states of heteroepitaxial double-layer system: Graphite/monolayer hexagonal boron nitride/Ni(111)*, Phys. Rev. B **54**, 13491 (1996).

[113] W. Di, S. Dhar, K. E. Smith, and S. D. Kevan, *Angle-resolved photoemission study of the clean and hydrogen-covered Rh(111) surface*, Phys. Rev. B **49**, 4821 (94).

[114] P. J. Feibelmann, *Electronic structure of clean and carbon-covered closed-packed rhodium and ruthenium surfaces*, Phys. Rev. B **26**, 5347 (1982).

[115] A. Catellani, M. Posternak, A. Baldereschi, and A. J. Freeman, *Bulk and surface electronic structure of hexagonal boron nitride*, Phys. Rev. B **36**, 6105 (1987).

[116] M. Morscher, M. Corso, T. Greber, and J. Osterwalder, *Formation of single layer h-BN on Pd(111)*, Surf. Sci. **600**, 3280 (2006).

[117] H.-J. Neff, I. Matsuda, M. Hengsberger, F. Baumberger, T. Greber, and J. Osterwalder, *High-resolution photoemission study of the discommensurate (5.55×5.55) Cu/Si(111) surface layer*, Phys. Rev. B **64**, 235415 (2001).

[118] J. Voit, L. Perfetti, F. Zwick, H. Berger, G. Margaritondo, G. Grüner, H. Höchst, and M. Grioni, *Electronic Structure of Solids with Competing Periodic Potentials*, Science **290**, 501 (2000).

[119] S. Hüfner, J. Osterwalder, T. Greber, and L. Schlapbach, *Interpretation of substrate photoelectron diffraction*, Phys. Rev. B **42**, 7350 (1990).

[120] M. R. C. Hunt and R. E. Palmer, *The structural and vibrational properties of* C_{60} *adsorbed on the graphite (0001) surface*, Surf. Rev. Lett. **3**, 937 (1996).

[121] A. V. Hamza and M. Balooch, *The chemisorption of* C_{60} *on Si(100)-(2×1)*, Chem. Phys. Lett. **201**, 404 (1993).

[122] G. Gensterblum, K. Hevesi, B.-Y. Han, L. -M. Yu, J. -J. Pireaux, and P. A. Thiry, *Growth mode and electronic structure of the epitaxial* C_{60}*(111)/GeS(001) interface*, Phys. Rev. B **50**, 11981 (1994).

[123] M. Muntwiler, W. Auwärter, A. P. Seitsonen, J. Osterwalder, and T. Greber, *Rocking motion induced charging of* C_{60} *on h-BN/Ni(111)*, Phys. Rev. B **71**, 241401 (2005).

[124] A. Tamai, *Molecular Arrangement and Electronic Properties of Low-Dimensional* C_{60} *Systems*, PhD thesis, University of Zurich, 2005.

[125] E. I. Altman and R. J. Colton, *The interaction of* C_{60} *with noble metal surfaces*, Phys. Rev. B **71**, 241401 (2005).

[126] P.W. Stephens, L. Mihaly, P. L. Lee, R. L. Wetten, S. M. Huang, R. Kaner, F. Diederich, and K. Holczer, *Structure of single-phase superconducting K_3C_{60}*, Nature (London) **351**, 632 (1991).

[127] P. W. Murray, M. Ø. Pedersen, E. Lægsgaard, I. Stensgaard, and F. Besenbacher, *Growth of C_{60} on Cu(110) and Ni(110) surfaces: C_{60}-induced interfacial roughening*, Phys. Rev. B **55**, 9360 (1997).

[128] J. K. Gimzewski, S. Modesti, and R. R. Schlitter, *Cooperative Self-Asembly of Au Atoms and C_{60} on Au(111) surfaces*, Phys. Rev. Lett. **72**, 1036 (2001).

[129] J. Weckesser, C. Cepek, R. Fasel, J. V. Barth, F. Baumberger, T. Greber, and K. Kern, *Binding and ordering of C_{60} on Pd(111): Investigations at the local and mesoscopic scale*, J. Chem. Phys. **115**, 9001 (2001).

[130] A. Tamai, A. P. Seitsonen, R. Fasel, Z.-X. Shen, J. Osterwalder, and T. Greber, *Doping induced reorientation of C_{60} molecules on Ag(111)*, Phys. Rev. B **72**, 085421 (2005).

[131] E. I. Altman and R. J. Colton, *Determination of the orientation of C_{60} adsorbed on Au(111) and Ag(111)*, Phys. Rev. B **48**, 18244 (1993).

[132] Y. Kuk, D. K. Kim, Y. D. Suh, K. H. Park, H. P. Noh, S. J. Oh, and S. K. Kim, *Stressed C_{60} Layers on Au(001)*, Phys. Rev. Lett. **70**, 1948 (1993).

[133] A. J. Maxwell, P. A. Brühwiler, S. Andersson, D. Arvanitis, B. Hernnäss, O. Karis, D. C. Mancini, and N. Mårtensson, *C_{60} on Al(111): Covalent bonding and surface reconstruction*, Phys. Rev. B **52**, R5546 (1995).

[134] M. Pedio, K. Hevesi, N. Zema, P. Perfetti, R. Gouttebaron, J.-J. Pireaux, R. Caudano, and P. Rudolf, *C_{60}/metal surfaces: adsorption and decomposition*, Surf. Sci. **437**, 249 (1999).

[135] A. J. Maxwell, P. A. Brühwiler, D. Arvanitis, J. Hasselström, and N. Mårtensson, *C 1s ionization potential and energy referencing for solid C_{60} films on metal surfaces*, Chem. Phys. Lett. **260**, 71 (1996).

[136] W. Auwärter, H. U. Suter, H. Sachdev, and T. Greber, *Synthesis of One Monolayer of Hexagonal Boron Nitride on Ni(111) from B-Trichloroborazine $(ClBNH)_3$*, Chem. Mater. **16**, 343 (2004).

[137] A. Goriachko, M. Corso, Y. B. He, M. Knapp, T. Brugger, S. Berner, J. Osterwalder, H. Over, and T. Greber, *Self-Assembly of a Hexagonal Boron Nitride Nanomesh on Ru(0001)*, Langmuir **23**, 2928 (2007).

[138] J. J. Weimer, E. Umbach, and D. Menzel, *The properties of K and coadsorbed CO + K on Ru(0001)*, Surf. Sci. **159**, 83 (1985).

[139] K. Wandelt, J. Hulse, and J. Küppers, *Site-selective adsorption of xenon on a stepped Ru(0001) surface*, Surf. Sci. **104**, 212 (1981).

[140] F. J. Himpsel, K. Christman, P. Heimann, and D. E. Eastmann, *Experimental band-energy dispersions and lifetimes for ruthenium*, Phys. Rev. B **23**, 2548 (1981).

[141] T. Pelzer, G. Ceballos, F. Zbikowski, B. Willerding, K. Wandelt, U. Thomann, Ch. Russ, Th. Fauster, and J. Braun, *Electronic structure of the Ru(0001) surface*, J. Phys.: Condens. Matter **12**, 2193 (2000).

[142] M.-C. Wu, Q. Xu, and D. W. Goodman, *Investigations of Graphitic Overlayers Formed from Methane Decomposition on Ru(0001) and Ru($11\bar{2}0$) Catalysts with Scanning Tunneling Microscopy and High-resolution Electron Energy Loss Spectroscopy*, J. Phys. C: Solid State Phys. **98**, 5104 (1994).

[143] M. Corso, T. Greber, and J. Osterwalder, *h-BN on Pd(110): a tunable system for self-assembled nanostructures?*, Surf. Sci. Lett **577**, L78 (2005).

[144] J. Repp, G. Meyer, and K.-H. Rieder, *Snell's Law for Surface Electrons: Refraction of an Electron Gas Imaged in Real Space*, Phys. Rev. Lett. **92**, 036803 (2004).

[145] A. D. Novaco and J. P. McTague, *Orientational Epitaxy-the Orientational Ordering of Incommensurate Structures*, Phys. Rev. Lett. **38**, 1286 (1977).

[146] G. Ertl and J. Küppers, *Low Energy Electrons and Surface Chemistry*, VCH Verlagsgesellschaft mbH, Germany, 1985.

[147] M. P. Seah, *The Quantitative Analysis of Surfaces by XPS: A Review*, Surf. Interface Anal. **2**, 222 (1980).

[148] M. P. Seah and W. A. Dench, *Quantitative Electron Spectroscopy of Surfaces: A Standard Data Base for Electron Ineleastic Mean Free Path in Solids*, Surf. Interface Anal. **1**, 2 (1979).

[149] S. Tanuma, C. J. Powell, and D. R. Penn, *Calculation of electron inelastic mean free path. II. Data for 27 elements over the 50-2000 eV range*, Surf. Interface Anal. **17**, 911 (1991).

[150] P. Prieto, C. Quiròs, E. Elizalde, and J. M. Sanz, *Electron inelastic mean free path and dielectric properties of a-boron, a-carbon, and their nitrides as determined by quantitative analysis of reflection electron energy loss spectroscopy*, J. Vac. Sci. Technol. A **24**, 396 (2006).

[151] J. J. Yeh and I. Lindau, *Subshell Photoionization Cross Sections*, Atomic Data and Nuclear Data Tables. **32**, 1 (1985).

[152] A. G. Shard, V. R. Dhanak, and A. Santoni, *Structural studies of the* $(\sqrt{3} \times \sqrt{3})R30^\circ$ *surfaces of chlorine and iodine on Rh(111)*, Surf. Sci. **429**, 279 (1999).

[153] A. G. Shard, V. R. Dhanak, and A. Santoni, *Structures of chlorine on palladium (111)*, Surf. Sci. **445**, 309 (2000).

Acknowledgements

The period spent at the University of Zurich during my Ph. D. work will always remain an unforgettable experience. A lot of persons contributed to my personal enrichment from a human and a scientific point of view.

First of all I would like to thank Prof. Jürg Osterwalder for welcoming me in his group and especially for the great relevance given to my project, in the belief that a 'naive' scientific discovery as the 'nanomesh', will be one day useful for the society.

I would like to thank my supervisor Prof. Thomas Greber for the brilliant ideas and the stimulating discussions shared with me.

Many thanks to all my colleagues for the friendly atmosphere that they created during the working and the free time: Milan Allan, Willy Auwärter, Simon Berner, Louis Branderberger, Thomas Brugger, Andrei Dolocan, Carine Galli, Cynthia Hengsberger, Dominik Leuenberger, Jorge Lobo-Checa, Thomas Mattle, Martin Morscher, Matthias Muntwiler, Taichi Okuda, Christian Schlepuetz and Richard Schillinger. Special thanks go to Anna Tamai and Claudio Cirelli that with me were the first generation of italian student in the group.

I am very grateful to all the members of the 'Nanomesh Consortium' and all the people involved in the 'Nanomesh' european project (FP6-STREP). This collaboration and the constructive interactions show how important the cooperation between groups with different background is in order to achieve scientific progress.

Thanks to Gabriel Lastennet from the institute of inorganic chemistry for the help in handling the borazine.

It has been a pleasure to work with Oliver Bunk, Roger Herger, Domenico Martoccia, Bruce Patterson and Phil Willmott during the beamtimes at the Swiss Light Source.

I would like to thank Roland Widmer, Oliver Gröning and Roman Fasel who contributed in the final solution of the intriguing issue of the nature of the 'nanomesh'.

I am glad to thank all the people from the Physik-Institut, always helpful in the case of need and to Kurt Bösiger and the team of the workshop for the professional work in constructing.

Many thanks to Peter Leškovský for the great help in the data processing and for his critical observations.

A big hug goes to my family that even if physically far, has always been present with the best advices and the appropriate words making me feel at home.

Finally I would like to thank Martin Klöckner and Matthias Hengsberger, not only for their constant presence in the case of need, but especially for their great willingness, for their patience and sense of humor noticeable at any occasion.

Curriculum Vitae

Name	Martina Corso
Birth	26.12.1978 in Palmanova (UD), Italy
Nationality	Italian

Education

1992-1997	Liceo Scientifico Statale "A. Einstein", Cervignano del Friuli (UD), Italy
Jun 1997	Maturità scientifica (58/60)
1997-2002	University of Trieste, Studies of Physics with specialization in Condensed matter Physics (A. Baldereschi, S. Modesti, R. Rosei, G. Senatore)
1999-2000	Third year of University as an Erasmus student at the Physics Department at The University of Manchester
Sep 2001-Nov 2002	Diploma work in the Surface Structure and Reactivity Group of Prof. Dr. G. Comelli and Prof. Dr. R. Rosei (Laboratorio TASC INFM, Trieste Italy) *Diploma Thesis Title*: "Reactivity of a surface strained structure: (10×2) of Oxigen on Rh(110)" studied with a VT-Omicron STM; supervisors: Prof. Dr. G. Comelli and Dr. F. Esch
Nov 2002	Graduation with full marks (110 cum laude/110)
since Mar 2003	Employed as Ph. D. student in the Surface Physics Group of Prof. Dr. Jürg Osterwalder, University of Zurich *Ph. D. Thesis Title*: "Boron Nitride Nanostructures on Transition Metals: Flat Layers and Nanomesh"; supervisors: Prof. Dr. J. Osterwalder and Prof. Dr. T. Greber
since Apr 2004	Participation to the Nanomesh European Project (FP6-STREP), www.nanomesh.org.

Teaching Experience

since Apr 2002	Teaching Assistant, University of Zurich (Taught lab-courses for medical students and problem classes in elementary and advanced solid state physics)
2005	Supervision in the Diploma Thesis of M. Morscher, *Title: "Hexagonal Boron Nitride on Pd(111): Nanomesh or Moiré Pattern?"*

Publications

1. **M. Corso**, W. Auwärter, M. Muntwiler, A. Tamai, T. Greber, and J. Osterwalder,
   "Boron Nitride Nanomesh",
   Science, **303**, 217 (2004)

2. C. Africh, F. Esch, W. X. Li, **M. Corso**, B. Hammer and G. Comelli,
   "Two-Step Reaction on a Strained, Nanoscale Segmented Surface",
   Physical Review Letters, **93**, 126104 (2004)

3. C. Africh, H. Lin, **M. Corso**, F. Esch, R. Rosei, W. A. Hofer and G. Comelli,
   "Water Production Reaction on Rh(110)",
   J. Am. Chem. Soc, **127**, 11454 (2005)

4. **M. Corso**, T. Greber, and J. Osterwalder,
   "h-BN on Pd(110): a tunable system for self-assembled nanostructures?",
   Surface Science Letters, **577**, L78 (2005)

5. T. Greber, L. Brandenberger, **M. Corso**, A. Tamai, and J. Osterwalder,
   "Single layer hexagonal boron nitride films on Ni(110)",
   Proceedings ALC05, e-J. Surf. Sci. Nanotech, **4**, 410 (2006)

6. M. Mulazzi, M. Hochstrasser, **M. Corso**, I. Vobornik, J. Fujii, J. Osterwalder, J. Henk, and G. Rossi
   "Matrix element effects in angle-resolved valence band photoemission with polarized light from the Ni(111) surface",
   Phys. Rev. B, **74**, 035118 (2006)

7. M. Morscher, **M. Corso**, T. Greber, and J. Osterwalder,
   "Formation of single layer h-BN on Pd(111),
   Surface Science , **600**, 3280 (2006)

–

O. Bunk, **M. Corso**, D. Martoccia, R. Herger, P. R. Willmott, B. D. Patterson, J. Osterwalder, J. F. van der Veen, and T. Greber,
"Surface X-Ray Diffraction Study of Boron-Nitride Nanomesh in Air",
to be published in Surface Science (2006)

M. Allan, S. Berner, **M. Corso**, T. Greber, and J. Osterwalder
"Tunable Self-Assembly of One-Dimensional Nanostructures with Orthogonal Directions",
to be published in Nano (2006)

A. Goriachko, **M. Corso**, Y. B. He, M. Knapp, T. Brugger, S. Berner, J. Osterwalder, H. Over, and T. Greber
"Self-Assembly of a Hexagonal Boron Nitride Nanomesh on Ru(0001)",
to be published in Langmuir (2006)

S. Berner, **M. Corso**, R. Widmer, O. Gröning, R. Laskowski, P. Blaha, T. Greber, and J. Osterwalder,
"Boron Nitride Nanomesh: Functionality from a Corrugated Monolayer",
submitted to Angewandte Chemie (2006)

Languages

Italian	Mother tongue
English	Fluent spoken and written (Cambridge Advanced Cerificate)
German	Discrete spoken and written (B2 level certificate)
Spanish	Basic